

# UNIVERSITÀ DEGLI STUDI DI PERUGIA

## DIPARTIMENTO DI FISICA E GEOLOGIA

*Corso di Laurea Magistrale in  
Scienze e Tecnologie Geologiche*



UNIVERSITÀ DEGLI STUDI  
DI PERUGIA

### TESI DI LAUREA

### DETECTION, CLASSIFICATION, AND ANALYSIS OF SINUOUS RILLES ON THE NEAR-SIDE OF THE MOON

Laureando:

SOFIA FIORUCCI

Relatore:

LAURA MELELLI

Correlatore:

MARIA TERESA BRUNETTI

Anno Accademico 2019/2020

*"I have not failed. I've just found  
10,000 ways that won't work."*

— *Thomas A. Edison*



# Table of Contents

## Chapter 1: Introduction

1.1	The Moon Mapping Project .....	1
1.2	Chang'E missions.....	4
1.3	Moon Mapping Topics .....	9
1.3.1	Topic 1 –Map of the solar wind.....	10
1.3.2	Topic 2 – Geomorphologic map of the Moon.....	11
1.3.3	Topic 3 – Data processing of Chang'E-1 mission .....	13
1.3.4	Topic 4 –Map of element distribution .....	14
1.3.5	Topic 5 – 3D Visualization system .....	14
1.3.6	Topic 6 –Tutorial and Atlas on joint lunar mapping .....	15
1.4	Thesis Objectives .....	16

## Chapter 2 - Origin of the Moon

2.1	Theory of formation: Proto-planet Theia.....	18
2.2	Lunar structure and composition.....	22
2.2.1	The crust .....	23
2.2.2	Upper and Middle mantel.....	27
2.2.3	The inner and outer core .....	27
2.3	Lunar geologic timescale .....	28
2.3.1	Pre-Nectarian .....	28
2.3.2	Nectarian .....	29
2.3.3	Imbrian.....	30
2.3.4	Eratosthenian .....	31
2.3.5	Copernican .....	31

## Chapter 3 – Morphologic description of the study area

3.1	Volcanic structures.....	37
-----	--------------------------	----

3.1.1	Domes .....	37
3.1.2	Cones.....	38
3.1.3	Volcanic systems .....	39
3.1.4	Crater chains or <i>catenae</i> .....	46
3.1.5	Sinuous rilles.....	48
3.2	Tectonic structures .....	52

## **Chapter 4 –Lunar rille’s detection and classification**

4.1	Data and Images.....	56
4.1.1	Lunar Reconnaissance Orbiter Camera- Wide Angle Camera (LROC-WAC).....	58
4.1.2	Lunar Orbiter Laser Altimeter (LOLA) .....	60
4.1.3	Chang'E2 DOM .....	62
4.2	Detection and classification criteria .....	63

## **Chapter 5- Analysis of morphometric parameters**

5.1	Measures of morphometric parameters.....	71
5.2	Statistical distribution of morphometric parameters.....	78

<b>Conclusions .....</b>	<b>87</b>
--------------------------	-----------

<b>Bibliography.....</b>	<b>90</b>
--------------------------	-----------

# Chapter 1: Introduction

## 1.1 The Moon Mapping Project

The argument of this thesis takes its bases on the Moon Mapping international project, which started in early 2015 and ended in 2017, for a total length of three years. The project was a mutual collaboration between Chinese and Italian research teams, and undergraduate students from both countries with the aim of producing a new map of the lunar surface. The project was supervised by the Ministry of Science and technology, P.R. China (MOST), the National Remote Sensing Centre of China and the Italian Ministry of Education, University and Research (MIUR). The leader and the coordinators for the project were the Italian Space Agency (ASI) and the Centre of Space Exploration, Ministry of Education of China. Details about the Moon Mapping project' participants are summarized in *Table 1.1*.

Institution	Department	Location, Country
Italian Space Agency (ASI)	ASI Science Data Centre (ASDC)	Rome, Italy
National Inst. of Astrophysics (INAF)	Astronomical Observatory of Rome (OAR)	Rome, Italy
	Institute for Space Astrophysics and Planetology (IAPS)	
	Astronomical Observatory of Padua (OAPD)	Padua, Italy
National Research Council (CNR)	Research Inst. for Geo-Hydrological Protection (IRPI)	Perugia, Italy
	Dept. of Aerospace Science and Technology	Milan, Italy
	Dept. Architecture, Built environment and Construction Engineering (ABC)	
University of Cagliari	Dept. of Chemical and Geological Sciences	Cagliari, Italy
University d'Annunzio	IRSPL – Dept. of Engineering and Geology	Pescara, Italy
University of Padua	Dept. of Geosciences	Padua, Italy
University of Parma	Dept. of Civil, Environmental, Land Management Engineering and Architecture (DICATeA)	Parma, Italy
University of Pavia	Dept. of Electrical, Computer and Biomedical Engineering	Pavia, Italy
China Ministry of Education	Center of Space Exploration (COSE), Chongqing University	Chongqing, China
China University of Geosciences	Dept. of Remote Sensing and Geo-Information Engineering, School of Land Science and Technology	Beijing, China
East China Normal University	School of Geographic Sciences	Shanghai, China
Nanjing University	School of Geographic and Oceanographic Sciences	Nanjing, China
Tsinghua University	Dept. of Computer Science and Technology	Beijing, China

*Table 1.1: Participants of the Moon Mapping Project, main institutions. (Scaioni et al., 2016)*

Building a solid and mutual scientific collaboration between the two countries was one of the main goals of the project, but the real backbone of the entire work was the interaction among undergraduate students. Under the supervision of a senior researcher, they had the opportunity to improve their scientific knowledge and test themselves with different types of study approaches. Collaboration between students were encouraged since the first meeting

and were carried on, despite the distance between Italy and China, throughout all the project timeline.

The idea of an international collaboration in planetary science was born initially in 2012 under the name of “Joint Lunar Map Drawing Project by Chinese and Italian College Students”. In 2015 a collaboration agreement was definitely signed by the Italian Space Agency (ASI) Science Data Centre (ASDC) director Paolo Giommi and the vice-president of the Chinese National Space Agency (CNSA) Gengxin Xie (*Figure. 1.1*). A schedule of mutual visits, workshop, and conferences (*Figure 1.2 and 1.3*) was defined in order to manage the scientific activity and produce a geomorphological and technical map of the Moon.



*Figure 1.1:* Moon Mapping Project workshop 23rd January 2015 ASI Headquarters – Rome. Credits: <https://solarsystem.ssdc.asi.it/change/>



*Figure 1.2:* The Moon Mapping Project 6th workshop 17th November 2017 Guyang, China. Delivery ceremony to the Chinese and Italian ministry of education. Credits: <https://solarsystem.ssdc.asi.it/change/>

Data used in the Moon Mapping project by the students and researchers was collected during the Chinese Lunar Exploration Program (CLEP), and it included the series of Chang'E missions. CLEP program includes Chang'E-1 (2007), E-2 (2010), E-3 (2014), E-4 (2018) and E-5 (2020). In particular, for the researches of Moon Mapping Project only the Chang'E-1 and part of Chang'E-2 data have been made available. CLEP program started with the launch of Chang'E-1 spacecraft (Zuo, Li e Zhang 2013, Ouyang , et al. 2010) in October 2007 and the landing in March 2009 in the region of *Mare Fecunditatis*. Chang'E-2 space probe was launched in October 2010, with similar but improved instruments already flown on Chang'E-1. Both the space probes were equipped with a CCD (charge-coupled device) stereo camera, an



*Figure 1.3: China- Italy forum of Lunar and Deep Space Exploration 18th November 2015, Geoscience International Conference Centre- Beijing. Credits: <https://solarsystem.ssdc.asi.it/change/>*

interference imagine spectrometer (IIM), a laser altimeter (LAM), a gamma-ray spectrometer (GRS), an X-ray spectrometer (XRS), a microwave radiometer (MRM), a high-energy particle detector (HPD) and a solar wind ion detector (SWID) (Ouyang , et al. 2010, Zuo, Li e Zhang 2013).

A brief description of Chang'E-1 and Chang'E-2 orbiter satellites and the dataset collected by them and used during the development of the Moon Mapping Project's research activity is reported in the following.

## 1.2 Chang'E missions

The Chinese Lunar Exploration Program (CLEP) is composed of 3 mission phases: 1) orbiting; 2) soft landing and 3) sample returning with lunar landing. Chang'E-1 (*Figure 1.4*) and Chang'E-2 missions were designed for the first phase, which was a demonstration of China's technologies progress other than a new step to the Moon exploration.

The first stage of CLEP program, involved the launch of Chang'E-1, programmed in 2007 and Chang'E-2, programmed in 2010. Both the lunar probes were equipped with similar instruments but Chang'E-2, improved the performances of its predecessor with its advanced payloads, i.e. a CCD stereo camera with a higher spatial resolution (7 m/px). The lunar probe Chang'E-1 was launched in October 2007, entered in the Moon's orbit in November 2007 and landed in 2009. It represents the first Chinese probe to orbit a body besides Earth. The entire mission lasted 495 days and during its life, Chang'E-1 collected a total of 1.37 TB raw data (Ouyang , et al. 2010) analysed by Ground and Research Application System (GRAS) of CLEP.

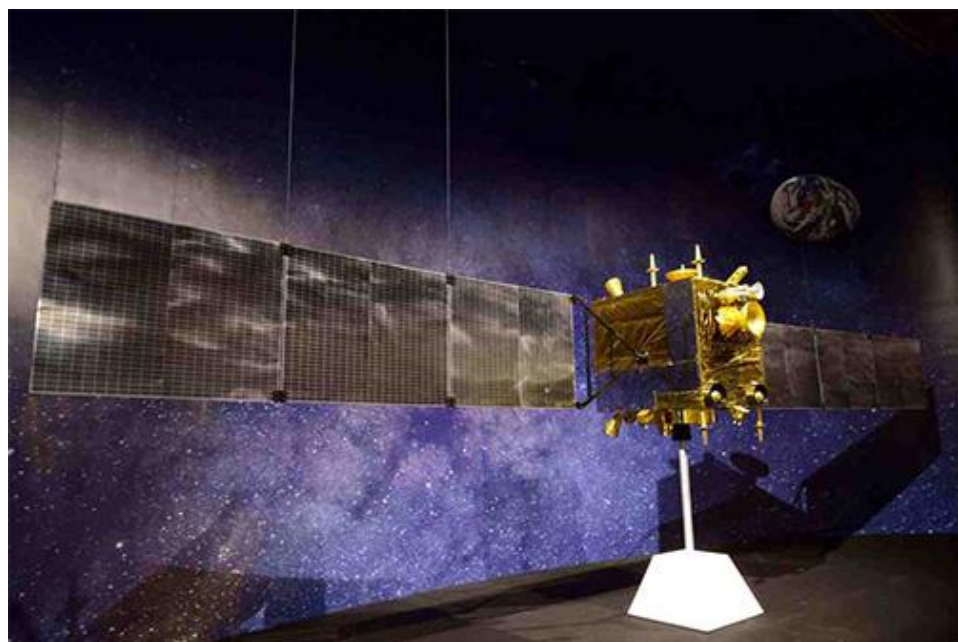


*Figure 1.4: Chang'E-1 model from the exhibition of Chinese lunar exploration program, Hong Kong museum.*

Credits: <https://hk.science.museum/ms/cle/exhibits.html>

Chang'E-1 goals can be reassumed in four points (Ouyang , et al. 2010):

- Map the entire Moon with global 3D stereo images of the Moon, with the aim of studying the features on the lunar surface
- Explore the abundance of key elements in the lunar surface (K, Th, U, O, Si, Mg, Al, Ca, Te, Ti, Na, Mn, Cr, La), using GRS and XRS. Chang'E-1, equipped with IIM, GRS and XRS instruments, was able to detect the composition and relative distribution of chemical elements and minerals on the lunar surface and derived, through the Moon's reflectance properties, the mineral chemistry of the lunar regolith<sup>1</sup>.
- Measure the microwave brightness temperature of the Moon using MRM to deduce physical properties and thickness of the lunar regolith, in combination with the surface composition.
- Investigate the space environment around the Moon, used to study the impact of solar activity on the earth and the Moon.

Chang'E-2 was launched in October 2010 and it had the major goal to obtain high-resolution images of specific lunar areas (north and south poles and *Sinus Iridum*). Chang'E-2 equipment is similar to his predecessor, but it was improved for its specific mission; see *Table 1.2* for the instrument details. Noteworthy for this thesis and for the result of the mission itself are the instruments carried by Chang'E-1 and Chang'E-2, CCD stereo camera and the LAM (Laser Altimeter). The two instruments provided a 1:2.5 million-scale global image mosaic. A co-registration method between stereo images and laser altimeter data have been processed by IRSA (Institute for Remote Sensing Applications) of Beijing (China), in order to provide 3D high precision mapping of lunar surface.

---

<sup>1</sup> Regolith is a layer of loose, heterogeneous superficial deposits covering solid rock. It includes dust, broken rock, and other related materials and is present on Earth, the Moon, Mars, some asteroids, and other terrestrial planets and moons. ( (Oxford Dictionaries 2008)

The CCD stereo camera with the registration of LAM data through surface matching and a 3D rigid transformation model automatically generated DEM images.

**Table 1 Summary of exploration instruments and functions**

Mission	Payload	Scientific objective
CE-1, CE-2	CCD stereo camera (CCD)	To acquire 3-dimensional mapping of the lunar surface at a spatial resolution of 120 meters (CE1) and 10 meters (CE2) for morphological and tectonic analyses, as well as for identifying potential landing sites
CE-1, CE-2	Laser altimeter (LAM)	To obtain the digital elevation model (DEM) of the entire lunar surface at a 7 km spatial resolution, which also helps to improve the positioning of the CCD imaging data
CE-1	Interference imaging spectrometer (IIM)	To obtain the spectral information of the lunar surface in the 0.5–1 $\mu\text{m}$ wavelength range for analyzing the composition of the surface materials
CE-1, CE-2	Gamma-ray spectrometer(GRS)	To obtain the $\gamma$ -ray spectrum in the 0.3–9 MeV energy range of the lunar surface materials to estimate the distribution of heavy elements such as U, Th, K, Fe and Ti
CE-1, CE-2	X-ray spectrometer (XRS)	To obtain the X-ray spectra in the 1–10 keV energy range of the lunar surface materials to estimate the distribution of heavy elements such as Mg, Al and Si
CE-1, CE-2	Microwave radiometer(MRM)	To obtain the lunar brightness temperature at different frequencies, to estimate the thickness of the lunar regolith and to evaluate the lunar $^3\text{He}$ content
CE-1, CE-2	High-energy particle detector (HPD)	To obtain the spectra of high energy particles to investigate the spatial and temporal variability of the near-Moon plasma environment
CE-1, CE-2	Solar wind ion detector(SWID)	To probe the near-Moon space plasma environment by measuring the energy spectra of protons and ions between 40 eV and 20 keV

*Table 1.2: Summary detailed description of Chang'E-1 and Chang'E-2 payloads. Credits: (Zuo et al., 2013)*

With this process, a lunar topography model was obtained based on LAM data and altimetry data made possible improves fundamentals parameters of Moon's shape (Kramer 2012):

- Mean radius: 1737013 m
- Mean polar radius: 1735843 m
- Mean equatorial radius: 1737646 m
- Flattening: 1/963.7526

Chang'E-2 was equipped with five instruments for the imaging, gamma-ray detection, solar wind detection, high energy particles detection and a CCD stereo camera. It collected six Tb of raw data, including high resolution overall Moon images. The most important data retrieved by the Chang'E-2 CCD camera was a detailed map of Sinus Iridium region, which was the landing site of the next Chang'E-3 mission (Kramer 2012). Unfortunately, due to the instrument failure, Chang'E-2 was not able to collect a significant amount of LAM data. However, it improved the quality of 2D images of the lunar surface with a spatial resolution < 10 m/pixel, but also the knowledge of the lunar surface composition and the amount of observations of the Earth-Moon space environment. Indeed, Chang'E-1 examined the

environment between the lunar surface and the payload altitude at about 200 km, while Chang'E-2 reached a lower altitude of 100 km (Ouyang , et al. 2010, Zuo, Li e Zhang 2013).

Although the Moon Mapping project was only based on the use of Chang'E-1 and Chang'E-2 data, a brief description of the other three phases of CLEP and its achievements is here reported in order to give an exhausting point of view about the China progress in space exploration.

The second phase has started in 2013 with Chang'E-3 which included a lander and a rover mission (Sun, et al. 2014) and in 2018 with the second lander Chang'E-4 (Ye, Sun e Li 2017). The objective of Chang'E-3, which is the third robotic lunar probe mission, was soft-landing on the lunar surface and exploring the surrounding area. The lunar probe is composed of two modules: a lander and a lunar surface exploration vehicle (the rover was named "Yutu" or jade rabbit). Despite the rigid program that planned to bring Yutu on the landing site *Sinus Iridium* near the *Mare Imbrium*, the rover actually has set down in the northern region of Sea of Rains, at the eastern edge of its original landing site (Kramer 2012).

Chang'E-4 had the same equipped payloads of Chang'E-3 and it incorporated, as the previous mission, a lander and a rover. CLEP dedicated this mission on studying the harsh environment of the "Far Side"<sup>2</sup> of the Moon, precisely in Aitken Basin in the South Pole region. Remarkable is the bio-experiment conducted on the Chang'E-4 lander. In this mission, China started to test how crops could be response an extreme environment such as the lunar polar region, constantly bombarded by cosmic rays and with temperature that swung between +127°C (day-time) and -173°C (night-time). A small cotton bud (*Figure 1.5*) has grown inside a little greenhouse build inside the lander. Unfortunately, due to a black out problem, the team of the experiment was forced to shut down the energy that kept a constant temperature inside the greenhouse at 25°C, exposing the bud to the icy lunar night.

---

<sup>2</sup> The Moon is divided into two side: the "Near Side", which is the visible face of the Moon, hit by the sunlight and the "Far Side" which is the hidden face of the Moon, impossible to see with the bare eye.

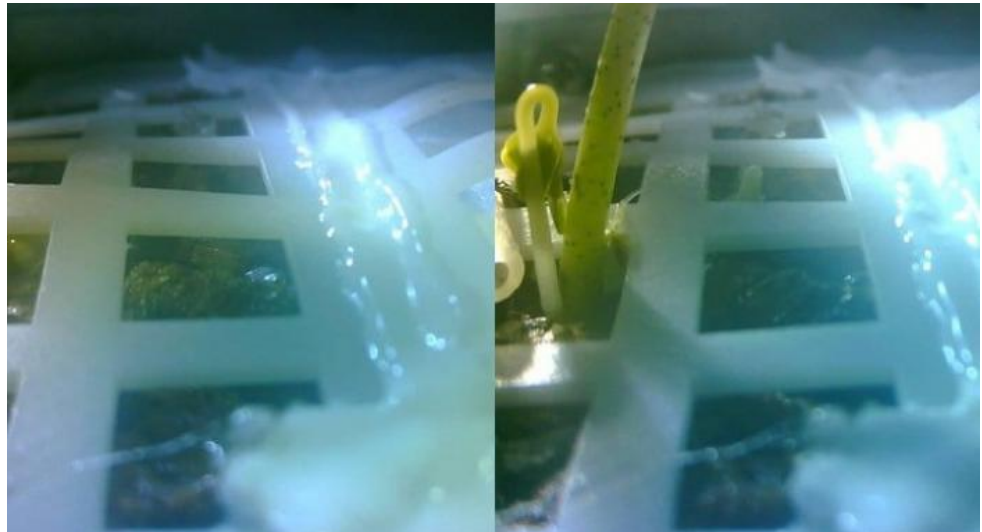


*Figure 1.5: The cotton bud during its grown. Credits: Chinese Lunar Exploration Program, Chongqing University. Credit: People's Daily, China (via Twitter)*

The third phase is schedule for December 2020 with Chang'E-5 sample-return lander launch. It will be the first Chinese sample-return mission and the first since Luna 24 in 1976 to collect at least 2 Kg of samples back to the Earth. The landing site will be *Mons Rümker* in *Oceanus Procellarum*, an elevated volcanic region of 70 Km of diameter. As its predecessors, Chang'E-5 will carry payloads such as a CCD stereo camera, a spectrometer and ground-penetrating radar. The ultimate and ambitious step is to build a lunar research station, expected to operate in 2023-2027. The structure will be autonomous using *in-situ* resources and all the technology necessary for a permanent lunar space base.

## 1.3 Moon Mapping Topics

A rich schedule of workshops, meetings and conferences was planned in order to complete the Moon Mapping project within the deadline in December 2017. The research work was organized into six main topics, each one supervised by different research institutes of China and Italy (*Tables 1.3 and 1.4*). A brief introduction of the topics is here presented. Though this thesis is mainly focus on topic 2 and topic 3 arguments, it is important to give, even if just mentioned, a satisfying description of the other topics, because all the arguments cannot be considered as separated works from the overall project, but part of an extremely complex and articulated exchange of data and interpretations, which paved the way for future collaborations among Chinese and Italian students in this field of research.

Institution	Department	Location, Country
Italian Space Agency (ASI)	ASI Science Data Centre (ASDC)	Rome, Italy
National Inst. of Astrophysics (INAF)	Astronomical Observatory of Rome (OAR)	Rome, Italy
	Institute for Space Astrophysics and Planetology (IAPS)	
	Astronomical Observatory of Padua (OAPD)	Padua, Italy
National Research Council (CNR)	Research Inst. for Geo-Hydrological Protection (IRPI)	Perugia, Italy
Politecnico di Milano (Technical University of Milan)	Dept. of Aerospace Science and Technology	Milan, Italy
	Dept. Architecture, Built environment and Construction Engineering (ABC)	
University of Cagliari	Dept. of Chemical and Geological Sciences	Cagliari, Italy
University d'Annunzio	IRSPOS – Dept. of Engineering and Geology	Pescara, Italy
University of Padua	Dept. of Geosciences	Padua, Italy
University of Parma	Dept. of Civil, Environmental, Land Management Engineering and Architecture (DICATeA)	Parma, Italy
University of Pavia	Dept. of Electrical, Computer and Biomedical Engineering	Pavia, Italy
China Ministry of Education	Center of Space Exploration (COSE), Chongqing University	Chongqing, China
China University of Geosciences	Dept. of Remote Sensing and Geo-Information Engineering, School of Land Science and Technology	Beijing, China
East China Normal University	School of Geographic Sciences	Shanghai, China
Nanjing University	School of Geographic and Oceanographic Sciences	Nanjing, China
Tsinghua University	Dept. of Computer Science and Technology	Beijing, China

*Table 1.3 : Members of "Moon Mapping Project" between Italy and China (Scaioni, et al. 2016).*

Project Topics	Topic Coordinators	
	Italy	China
1 Map of the solar wind ion	ASDC	Tsinghua University
2 Geomorphologic map of the Moon	Politecnico Milan	China Univ. Geosciences
3 Data preprocessing of Chang'E 1 mission	INAF-IAPS	East China Normal Uni
4 Map of element distribution	Univ. of Cagliari	Nanjing University
5 3D visualization system	ASDC	China Univ. Geosciences
6 Tutorial and Atlas on joint lunar mapping	Chongqing University	University d'Annunzio

*Table 1.4: Moon Mapping project's topics and their Topic coordinators. (Scaioni, et al. 2016).*

### **1.3.1 Topic 1 –Map of the solar wind**

Topic 1 was focused on the analysis of solar wind ions, based on existing research results and the measurements of Chang'E-1, collected by the instruments on board: Solar Wind Ion Detector (SWID) and the High-energy Particle Detector (HPD) (Ouyang , et al. 2010, Kramer 2012). SWID instrument on board of Chang'E-1 is designed to analyse the ions with low energy in the same space with high-energy particle detector (HDP). In particular, two sets of SWID instruments were equipped on the lunar probe. The SWID A and the SWID B instruments detected the solar wind ions particles, one in certain polar region, the other in all polar region with the exception collect by the other one (Kramer 2012). Noteworthy, the data collected by SWID change periodically, 127 minutes per cycle. The main objective of the Topic is to produce maps of the solar wind ions. An interactive visualization approach for drawing low-energy solar ion flow distribution at arbitrary time will give a real-time display of solar wind ion flow and its direction. To date, data from Chang'E-1 SWID have been analysed to obtain the spacecraft velocity and the Sun Incidence angle (Scaioni, et al. 2016).

A second stage consisted in a post-processing elaboration of the data. The work time schedule has been divided into five sub-topics:

1. Merging of SWID A and SWID B (time synchronization)
2. Evaluation of solar wind parameters by SWIDA/B data fit
3. Elaboration of a multidimensional solar wind ions map
4. Evaluation of Earth/Sun magnetic field
5. Correction of the magnetic field effects

Predict the direction and the intensity of the solar wind and its impact on the lunar surface is a crucial outcome for future missions.

### 1.3.2 Topic 2 – Geomorphologic map of the Moon

The topic is focused on the detection and the analysis of the geomorphological structures on the lunar surface. Due to the multispectral approach, the topic is divided into three sub-topics:

Sub-topic 2.1 is focused on mapping craters, including features like ejecta and studying the development of crater morphology and degradation. Studying the impact crater is important to understand the terrain evolution and the history of Solar system. In this sub-topic the major objective is to develop an algorithm for the automatic identification and mapping of impact craters (*Figure 1.6*). A team from the University of Pavia, from the Italian side, developed an algorithm for the automatic detection of craters and other morphologies of interest (Kang, Luo, et al. 2015). For the topic, the team used Chang'E-1 and Chang'E-2 stereo images and DEMs (Digital Elevation Model) images obtained by the co-calibration of CCD stereo camera and LAM instruments. Morphometric geometries were identified starting from a generated DTM (Digital Terrain Model), and measurement of morphometric parameters like slope, openness, and plan curvature were achieved. (Scaioni, et al. 2016).

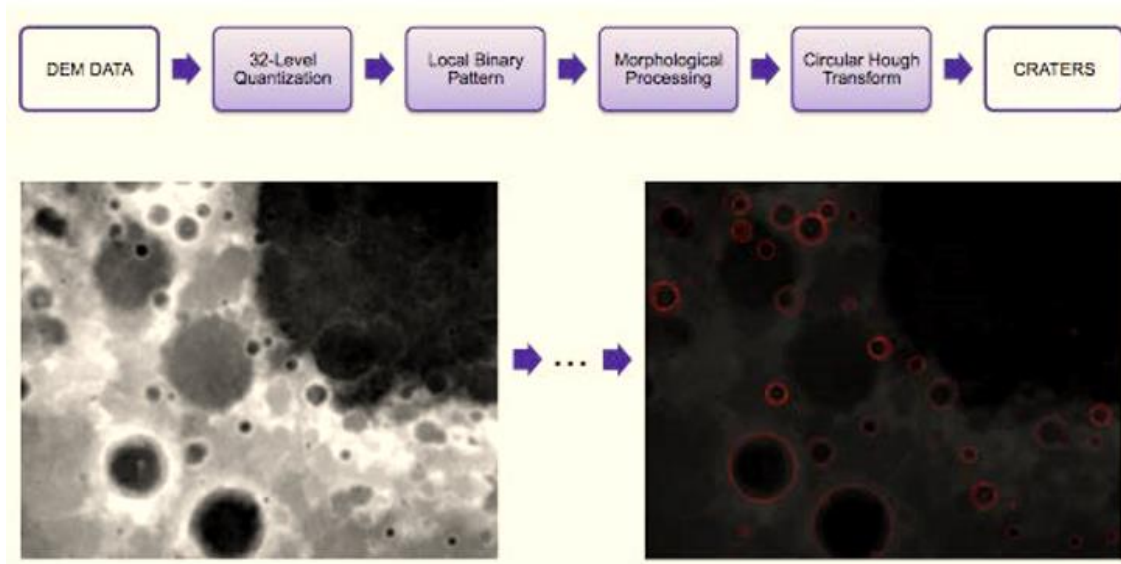


*Figure 1.6: Procedure of craters' extraction developed by University of Pavia (Kang, Luo, et al. 2015, Scaioni, et al. 2016).*

The Sup-topic 2.2 focused on the characterization of landslides inside the impact craters. A team work, composed by Politecnico di Milano, CNR-IRPI (National Centre of Research-Institute for the Hydrogeological Protection and Research), University of Cagliari, INAF-OAR (National Astrophysical Institute – Observatory of Arceteri) and INAF-OAPD (National Astrophysical Institute– Observatory of Padua), have studied an automatic approach to locate mass wasting inside impact-craters on the lunar' surface (P. Gamba, et al. 2015, Scaioni, et al. 2016). Based on a work of Brunetti et al. (2015) (*Figure 1.7*) who visually classified nearly 60 landslides, this new method has the priority to enhance the classic, subjective method with another objective approach (Guzzetti , Mondini, et al. 2012, Brunetti, et al. 2015, Scaioni, et al. 2016). The teamwork used Chebyshev polynomials (Mahanti, Robinson e Thompson 2015, Yordanov, et al. 2016) to identify each crater with a theoretical shape in order to analyse any geometries that deviate from the classical bowl-shape of the craters, interpreting them as a signature for the possible presence of a landslide. A DTM (Digital Terrain Model) from the NASA LROC (Lunar Reconnaissance Orbiter Camera, (Chin, Brylow, et al., Lunar Reconnaissance Orbiter Overview: The instrument suite and Mission 2007) was initially used to develop the method, which was then applied to Chang'E-2 data.

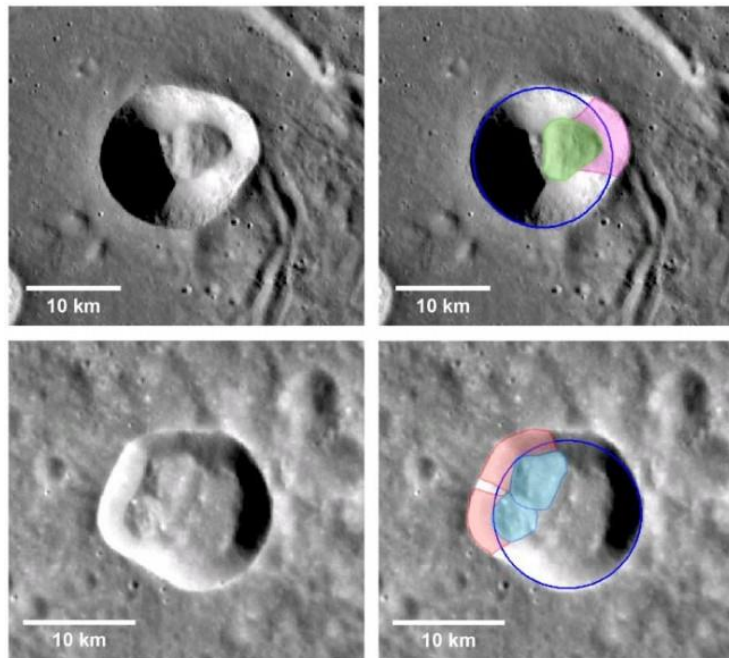


*Figure 1.7: Classification of landslides inside impact craters (Brunetti, et al. 2015).*

The Sup-topic 2.3 included the detection and characterization of lava-tubes below the lunar surface and their correlation with sinuous rilles. This is the main subject of this thesis, therefore a specific discussion on this sub-topic will be provided in chapter 4, where data and methods used are illustrated.

### 1.3.3 Topic 3 – Data processing of Chang'E-1 mission

The main objective of Topic 3 is to investigate, calibrate and pre-process procedures that sensors carried by Chang'E-1 need to output correctly their data. In particular, the topic worked on the correction of the distortion of the imaging system, calibration of the laser altimeter, and photometric and in-flight calibration of the Interference Imaging Spectrometer (IIM) on board Chang'E-1. *Figure 1.8* shows the pre-processing workflow.

Data pre-processing is often the most time consuming and costly phase of the analysis workflow, nevertheless it was needed in preparing the Chang'E-1 data that have been used in the other Topics of the Moon Mapping Project (Scaioni, et al. 2016).

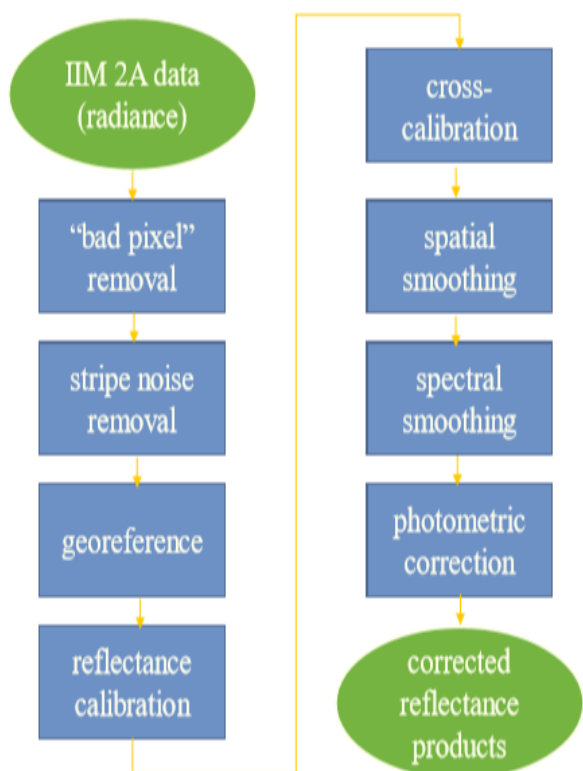


*Figure 1.8: IIM pre-processing workflow. (Scaioni, et al. 2016)*

### **1.3.4 Topic 4 –Map of element distribution**

The aim of Topic 4 was to produce a map of elemental distribution of the Moon surface using data collected by the Interference Imaging Spectrometer (IIM) on board CE-1 (Wu et al., 2010). The IIM spectral range (0.48-0.96  $\mu\text{m}$ ) was used to retrieve information about the differences in the lunar surface mineralogy and lithology. The IIM is a Sagnac-based<sup>3</sup> sensor able to obtain a multispectral imagery of the lunar surface, with a resolution of 200 m/pixel. IIM data have been made available through MATISSE, which is a web-based tool to access and visualize data from planetary exploration instruments (Zinzi, et al. 2016). One of the main future prospective is to integrate the research activity of Topic 4 with photo-interpretation and classification of the main elements to better describe their morphological origin (Scaioni, et al. 2016).

### **1.3.5 Topic 5 – 3D Visualization system**

Topic 5 had the purpose to integrate the results of the other topics through an advanced web-based visualization system called MATISSE. All the datasets uploaded in the tool are consultable and can be managed by the most common GIS desktop software packages. It is also possible to select a single high-order product (i.e. mosaic, DEM and orthophoto images, RGB images, ratios ...) or a single observation (*Figure 1.9*). Possible future development includes a Solar Wind Ion Detector (SWID) and Chang'E-2 data set (Scaioni, et al. 2016, Zinzi, et al. 2016). At the present time the Italian side has already add the data acquired from the CLEP mission.

---

<sup>3</sup> The Sagnac effect is a phenomenon observed in interferometry, resulted from the rotation of the signal. The effect can be seen with a ring interferometer. [https://en.wikipedia.org/wiki/Sagnac\\_effect](https://en.wikipedia.org/wiki/Sagnac_effect)

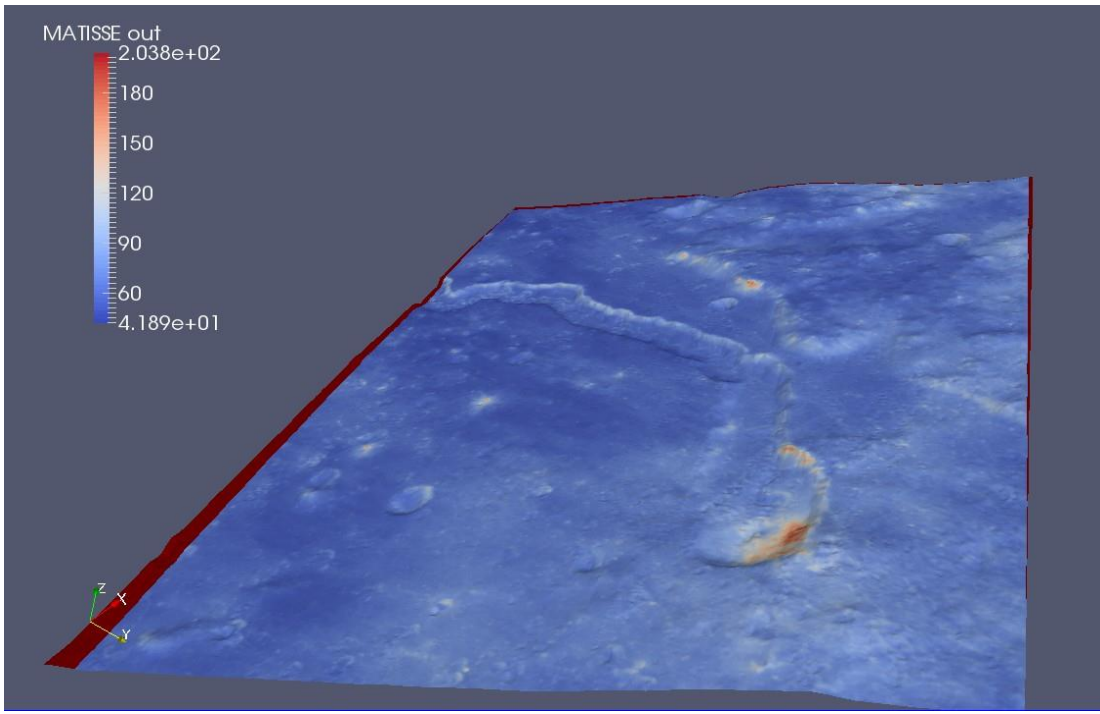


**Figure 1.9:** 3D visualization of a lunar crater with Chang'E-2 high-resolution orthophoto and NASA DEM (Zinzi, et al. 2016).

### 1.3.6 Topic 6 –Tutorial and Atlas on joint lunar mapping

The purpose of Topic 6 was the production of a Moon Atlas that also included the geological characterization of the lunar poles using Chang'E-1 and Chang'E-2 datasets. As mentioned, CLEP mission had the ultimate goal to build a permanent scientific base on the lunar surface in 2023-2027. Lunar poles have a strong scientific importance for future human exploration due to the continue sunlight exposition. For this reason, the area could be a prime location for the establishment of a solar power generation. Moreover, the temperature is nearly constant in these regions, being extreme oscillations during the day and nighttime nearly absent. Citing the cotton bud experiment conducted by Chang'E-4 mission in the Aitken Basin (*Figure 1.5*), the intent of CLEP was to test the reaction and the possibility of creating micro-habitat inside a controlled structure (greenhouse). This is the key point for the future human exploration on the space environment, not only for the Moon, but also for longer routes (i.e. Mars).

## 1.4 Thesis Objectives

This thesis is focused on the detection and classification of lunar sinuous rilles, and it is based on the work done during the Moon Mapping Project (Sub-topic 2.3). Due to the partial availability of data from Chang'E-1 and Chang'E-2, which was limited to the *Sinus Iridium* area (see § 4.1.3), the analysis involved Chang'E and LROC data as well. This permitted to extend the study area to an entire quadrant of the Moon.

Sinuous rilles are one of the most enigmatic features, that usually appear as channels of various lengths, depths and widths with parallel-striking, laterally continuous walls, and in association or not with a recognizable potential source vents (Hurtwitz, et al. 2012). These features are mostly common on the near-side of the Moon, especially on lunar basaltic seas (*maria*) rather than on highlands (*terrae*). Since SR developed for the most on the lunar *maria*, or at least on the extreme boundaries with the high topographic *terrae*, this would probably mean that *maria* experienced an intense volcanic activity during the lunar history. Although a general agreement on their volcanic origin, the exact formation process of the rilles remains undefined. Considering the available information, the thesis would aim to answer the following questions:

- 1) How did the volcanic origin influence the distribution of sinuous rilles? Was there any particular area where the volcanic activity was significantly intense? Can sinuous rilles help to identify the most active area in the past?
- 2) Sinuous rilles can be characterized by topographic parameters such as length, width, area, slope, and sinuosity. Can these parameters indicate a common pattern? Are there any characteristics that repeat? Can sinuous rilles be divided according to common characteristics in a given area?
- 3) Some SRs are extended for hundreds of kilometres, while others have smaller extensions. What is this difference due to?
- 4) Some SRs have a very articulate, meandering pattern but not all of them present the same characteristics. What does it depend on?

Using the QGIS standalone software ([www.qgis.org](http://www.qgis.org)), the sinuous rilles were mapped and measured, collecting all the data necessary for their characterization. In the initial phase of the

Moon Mapping project, the attention was focused only on the detection of lava tubes, which are a particular type of sinuous rille mainly developing below the lunar surface. This choice was driven by the scientific relevance that lava tubes offer for future human exploration (Blair, et al. 2016). Due to their difficult identification and the poor resolution of the available data, the subject of the study has become the SRs in general. Scientific interest on these structures is as relevant as the interest in lava tubes because both have a volcanic origin and studying their characteristics, will certainly help to understand better the morphological evolution of the lunar surface.

# **Chapter 2 - Origin of the Moon**

This chapter is dedicated to the description of the various theories on the formation of the Moon, with particular attention to the theory of the "Giant Impact". The physical and compositional characteristics of our satellite will be described, and a brief history of the geological evolution of the Moon, from its formation to the present day, is reported.

## **2.1 Theory of formation: Proto-planet Theia**

The origin of the Moon is still an argument of research studies, influenced by technologic progress of science exploration. Thanks to the Apollo mission in 1969, which returned samples back to the Earth, it is possible dating the Moon at 4.5 billion years ago. Since the relative size of the Moon respect to the Earth is strangely bigger if compared to other moons of the Solar system (i.e. Mars with Phobos and Deimos; Jupiter with Io, Europa, Ganymede, Calisto and Amaltea) which formed from a rotating cloud of gas and dust (Geiss e Rossi 2013), the Moon must have formed through a different process. Since the 1898, scientists have been proposed three different theories: fission, co-accretion and capture (Cummings 2019).

Fission theory can be divided into two schools of thought: rotational and collisional fission. In the rotational fission theory, the material that now constitutes the Moon was once a part of a rapidly rotating proto-Earth and was subsequently flung away from its parent by extreme high centrifugal force of the Earth's rotation. In the collisional fission theory, it is proposed a collision with another planetary body have been occurred. George Darwin (1845-1912), the second son of Charles Darwin, is the developer of the rotational fission theory. In Darwin's theory, the material that formed the Moon came from the upper layers of the Earth and thereby the Moon should have a density that is comparable to the density of the Earth's crust. The Moon's average density is  $3.34 \text{ g/cm}^3$ , which is significantly lower than the average density of the Earth,  $4.03 \text{ g/cm}^3$ . The density of material in the upper layers of the Earth, however, is close to the measured average density for the Moon. Heavier elements such as iron in the Earth's core cause the average density of the Earth to be higher than the density of material in its upper layers (Cummings 2019).

The astronomer Reginald Aldworth Daly (1871-1957) proposed the collisional fission in the 1940s. Daly proposed as alternative of Darwin's rotation fission theory:

[...] "a 'planetoid,' captured because of tangential, slicing, collision with the liquid earth, brought with it so much angular momentum as to ensure its perpetuation as a separate, revolving body—the moon we know [...]. Many of these were gravitationally aggregated by the pull of master fragment or captured 'planetoid' to make the substance of our moon, and the somewhat diminished earth felt a prolonged rain of other earth-fragments, large and small." (Daly 1946, Cummings 2019).

The co-accretion proposed by the American chemist Harold Urey (1883-1981), was the dominant theory in the 1960s and concerned the evolution of a slowly rotating cloud of dust and gas that first formed the Sun and then after flattening into an accretion disk and after formed planets. Both the Earth and the Moon originated from the same accretion disc, and consequently their internal structure should be similar (Urey 1952, Cummings 2019). Instead, the current physical parameters, i.e. different inclination of the rotation axis and different mass density, demonstrate that this theory is not plausible (Cano, Sharp e Sherer 2020).

The capture theory supported the idea that both, Moon and Earth, were originated in different region of the solar accretion disk or, anyway in different time. But if the Moon had accumulated its mass far away from the Earth and somehow was placed in an orbit around the Sun that brought it close to the Earth, it would still have difficulty in being captured by the Earth, as the kinetic energy of its motion would be too high for capture to take place. The capture hypothesis implied that the Earth would have been spinning at such a high rate that the length of the day would have been only 4.8 h, to be able to dissipate the high kinetic energy of the colliding Moon.

All the theories presented, at least before the advent of modern technology, were considered quite laudable and as Urey himself writes: [...] "there is no model for the origin of the moon that is not complicated and does not appear to be very highly improbable." [...] (Urey 1952, Cummings 2019). Please refer to the bibliography for further information on the various theories. Summarily, after their birth in the 1960s, these theories do not meet the physical requirement to explain the actual Moon characteristics and they were abandoned (Geiss e Rossi 2013) until the 1975 with W. Hartmann and D. Davis, who formulated the hypothesis of

“Giant Impact” (Hartmann e Davis 1975). Following NASA’s Apollo missions, in fact, scientists had the possibility to study lunar rock sample for the first time.

In this theory, a Mars-size object, named Theia, collided with the proto-Earth almost 4.5 billion years ago, smashing out the mantle of the Earth at a relatively velocity of about 14 000 km/h (*Figure 2.1*). This theory was calibrated and validated through mathematical models, which proved that the results are consistent with the nuclear mass of the Moon, its density, its nearly absence of volatile elements (H, C, N and other noble gasses) and the Earth-Moon angular momentum (Meyer, Reufer e Wieler 2014).



*Figure 2.1: Artist’s depiction of a collision between two planetary bodies. CREDIT: NASA/JPL-Caltech*

However, even if the theory seems to better explain the formation of the Moon and its characteristics, it still fails in reproducing the chemical composition, which is similar to that of the Earth. In fact, even though a Giant Impact can justify the low iron content of the Moon’s nucleus, the depletion of volatiles and the enrichment in refractory elements, the computer model reveals that the Moon should have been composed for almost 70-90% of the proto-lunar Theia, but it is actually not. Recently, four integrated theories have been formulated to explain why Earth and Moon have similar isotopic composition (Cummings 2019):

- Synesthesia: the impact was too violent that both the proto-Earth and Theia were vaporized and spread their masses formed a donuts cloud of dust. The two single elements were formed only in a second moment, with similar chemical compositions.
- Multi-impact: due to the small initial mass of Theia, one impact would not be enough to create the Moon, as we know now. A multi-impact occurred before the formation of the Moon, so that the similar composition is explained by the relatively small masses of the impacting celestial bodies in relation to the debris cut off from the proto-Earth.
- Similar bodies: Theia had an original chemical composition similar to the Earth, and the Giant Impact did not cause a significant change in chemical composition.
- Fourth theory: in this model, there were mixed together the classic impact hypothesis, considering Theia's size as the half of Mars' size, and the fission hypothesis proposed by Darwin. At first, the Earth-mass planet had a higher spin rate at the end of the accretion phase; therefore, the giant impact with Theia created a Moon-forming disk composed for the most by the lost material lost via spin by Earth. It was shown that an erosive giant impact onto a fast-spinning proto-Earth followed by despinning during passage through the evection resonance could reproduce the isotopic homogeneity and present angular momentum of the Earth-Moon system (Cuk e Stewart 2012).

Observing the non-volatile isotope ratio, especially at the triple oxygen isotope system  $\Delta^{17}\text{O}$ , it impossible to distinguish them from Earth's (Cano, Sharp e Sherer 2020). One explanation is that the proto-Earth and Theia were formed at the same heliocentric distances from the same isotopic reservoir or, alternatively, a re-equilibrium of the chemical elements occurred after the Giant Impact, when heterogeneity was adjusted. However, a recent study is trying to address the lunar composition problem, conducting a high-precision oxygen isotope analysis of a range of different lunar rocks. The results of this study shows that lunar rocks have a higher concentration of lighter oxygen isotopes than the Earth ones, and the difference increase when moving from crust to the mantle lunar rock (Cano, Sharp e Sherer 2020).

The lack of samples from the deepest areas of the lunar mantle requires more information for further studies. It is hoped that with future lunar explorations this gap will soon be filled to finally shed light on the mystery of the Moon's origin.

## 2.2 Lunar structure and composition

With a diameter of about 3474 km, the Moon is the fifth largest satellite in the Solar System. Its surface gravity is about 17% of that on Earth ( $1.62 \text{ m/s}^2$ ) and it has a volume and a mass respectively 2.0% and 1.2% of the Earth (Jaumann, et al. 2012). The Moon has an internal differentiation, distinct in crust, mantle, outer core and inner core, like the Earth (Figure 2.2) (Barnes, et al. 2012). The presence of internal layers was interpreted as a direct consequence of the giant impact, being the Moon immediately after impact in a molten state and with the lunar magma ocean (LMO) covering the entire surface (Hartmann, Phillips e Taylor 1986). During the subsequent eras (§ 2.3), the Moon underwent a series of purely igneous processes that led to the differentiation of its interior.

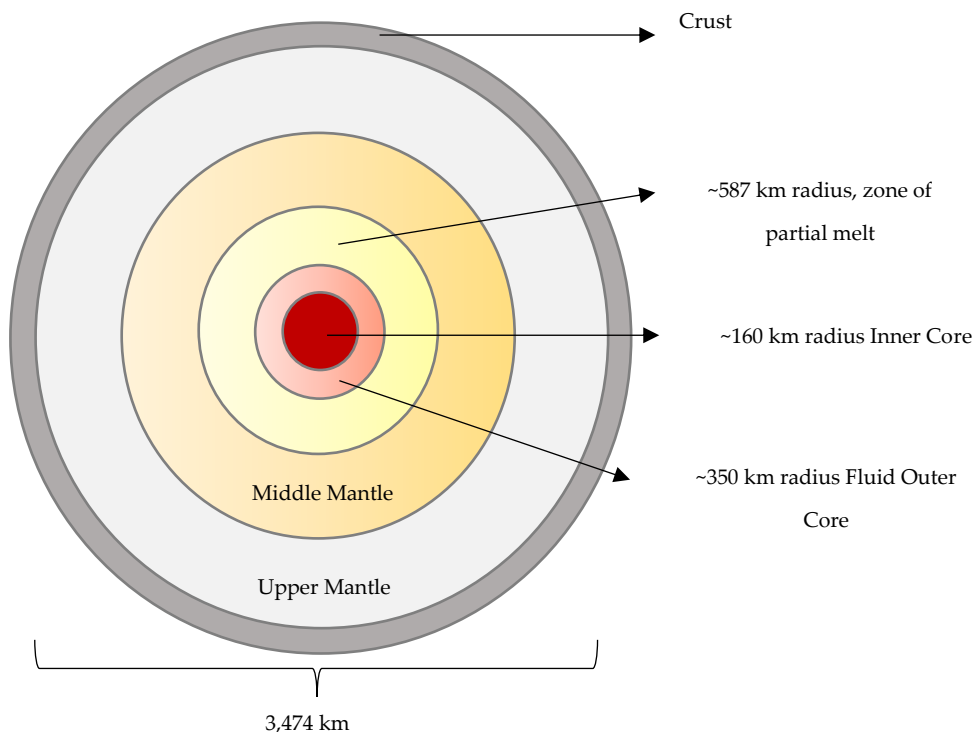


Figure 2.2: Diagram of the interior of the Moon.

### 2.2.1 The crust

Visually the Moon is divided into two topographically distinct morphologies: *maria* and *terrae* (Figure 2.3). The crust is the most superficial part, with a thickness that varies from 74 km in the *terrae* (far-side) to 12 km in the *maria* (near-side). Both of them are fully covered by regolith, which is originated by the mechanical disintegration of rocks and by the continuous bombardment by particles of solar and cosmic rays to which the lunar surface is constantly

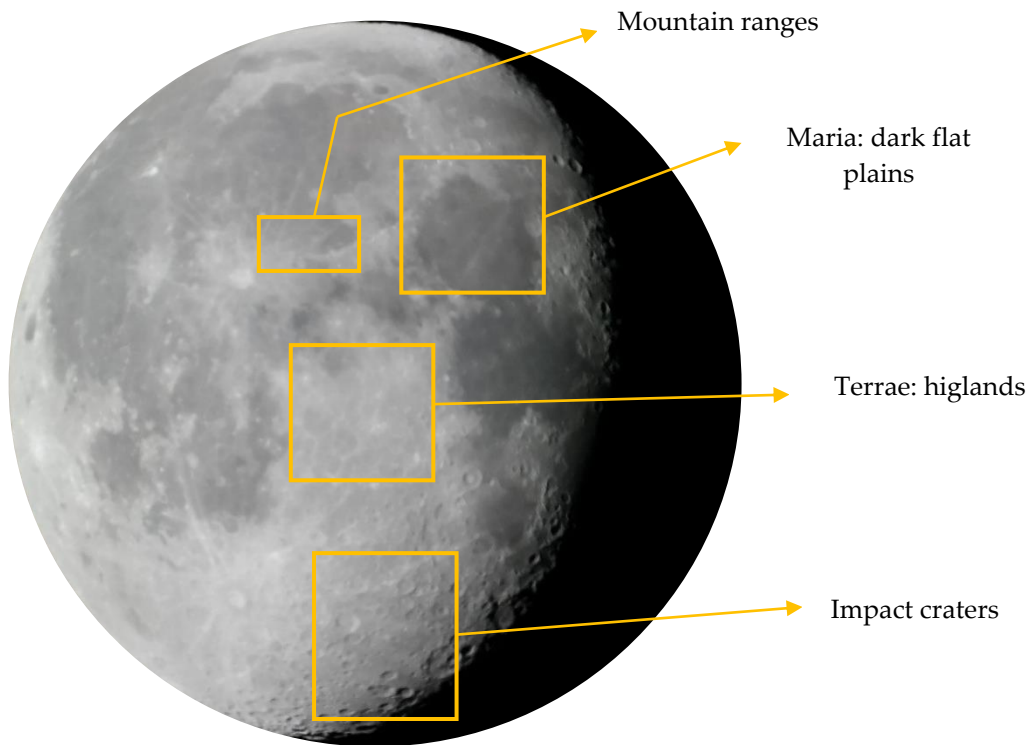


Figure 2.3: Main morphologies on the lunar surface highlighted by the orange rectangles. Credit: Fiorucci S.

exposed. The *maria* and *terrae* have a different elemental composition and in the following is presented a brief description of their mineral characterization.

*Maria* take their name from the ancient belief that these dark-coloured depressions had been covered by water. They have pseudo-circular shapes and their dark colour is essentially due to the low albedo<sup>4</sup>. They occupy about 17% of the whole surface with highest concentration in

<sup>4</sup> The albedo is the measure of the diffuse reflection out of the total solar radiation on a normalized scale from 0 (black body) to 1 (total reflectance body). The mean value of the Moon's albedo is 0.14, which is typical of the regolith surface.

the near-side, where they occupy 30% of the surface, whereas is about 2% in the far-side. Most of the *maria* are dated between 3-3.5 billion years (Wilhems 1987) and only very few of them are as old as 4.2 billion years. Maria and basins have different origin, even though before '60s, these two features were thoughts to have been formed by the same processes. Successive studies demonstrated that *mare* materials are younger than the basin materials and the two have formed by different processes. Basins formed likely after an impact, and in fact, only the kinetic energy released by an impact with a giant asteroid can explain the kinetic energy required for their formation. On the contrary, Maria have been formed from volcanic eruptions, in fact the lunar volcanism inside the *maria* was mainly characterized by effusive activity with rates of proportions never seen on Earth (Wilhems 1987). Lunar-mare material is made of dark coloured basalts, mafic, fine-grained extrusive or shallow-intrusive rocks (Wilhems 1987). Clinopyroxene and plagioclase compose the 75-90% of the most *maria* basalt but in terms of elemental abundance they differ from the Earth in Ca content, contains no detectable H<sub>2</sub>O, very low in alkalis especially in the form Na<sub>2</sub>O, generally high in TiO<sub>2</sub>, low in Al<sub>2</sub>O<sub>3</sub> and SiO<sub>2</sub>, very high in FeO and differ for their underrated structure. However, not all basalts on the lunar surface have the same Ti content. In fact, based on the distribution of this element, the lunar basalts can be divided into 3 categories (*Figure 2.4*):

- Moon basalts with high Ti content (>7 wt.%)
- basalts with a low Ti content (>3 wt%)
- moon basalts with very low Ti content (<2 wt%)

Minerals like aluminous, ilmenite, silica minerals, troilite and Fe metal are common accessories; lunar rocks have a less variety than that of the terrestrial rocks. Lunar mare basalt contains essentially no Fe<sup>3+</sup>, for the most occurs Fe<sup>2+</sup> and a minor amount of native Fe. The europium (Eu) on the lunar basalt rocks has a negative anomaly<sup>5</sup> while on Earth, generally there is a positive anomaly but the interesting fact is that lunar rocks are poor of siderophile

---

<sup>5</sup> Europium anomaly is the phenomenon whereby the europium (Eu) concentration in a mineral is either enriched or depleted relative to some standard commonly a chondrite or mid-ocean ridge basalt (MORB). A europium anomaly is said to be "positive" if the Eu concentration in the mineral is enriched relative to the other rare-earth elements (REEs), and is said to be "negative" if Eu is depleted relative to the other REEs. (Credit: en.wikipedia.org/wiki/Europium\_anomaly).

elements and in volatiles elements (Wilhems 1987, Jaumann, et al. 2012, Cano, Sharp e Sherer 2020).

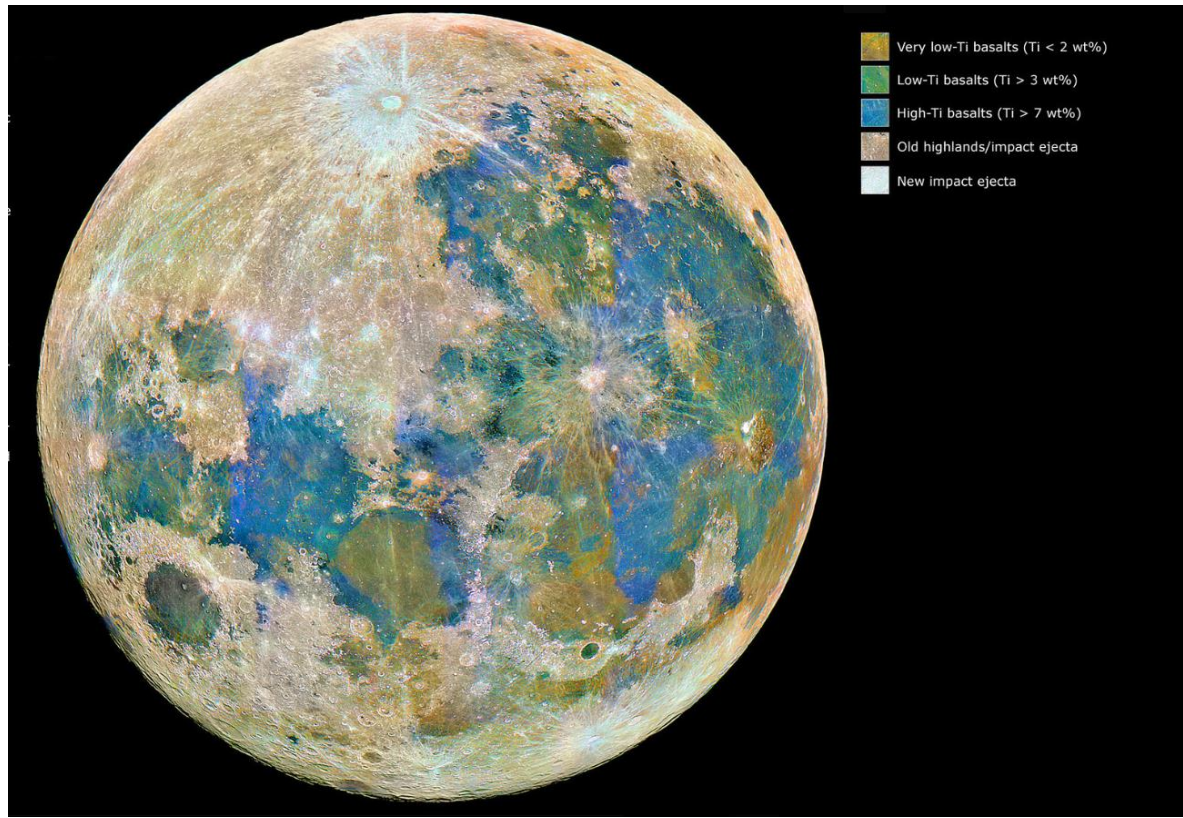


*Figure 2.4: Coloured enhance image of the Moon near-side and its different categories of mare basalts. Credit: Rolph Wahl Olsen/ <https://www.rolfolsenastrophotography.com/>*

*Terrae*, also recognizable as highlands, represent the highest morphology on the lunar surface and covered almost the 60% of the entire surface. Remote sensing missions as the LRO (Lunar Reconnaissance Orbiter) (Chin, Brylow, et al., Lunar Reconnaissance Orbiter Overview: The instrument suite and Mission 2007), launched in 2008, have measured the highest and the lowest point on the lunar surface. Referred to a sphere of 1737.4 km mean radius, the two points are located in the Aitken Basin South Pole -9100 m and in the Far-side highlands at +10770 m (Riris, et al. 2008, Jaumann, et al. 2012). *Terrae* host the oldest rocks on the lunar surface, as they exhibit a compositional variation that can be divided into 3 chemical groups, on the basis of their molar  $\text{Ca}/(\text{Ca}+\text{Na}+\text{K})$  content vs. the molar  $\text{Mg}/(\text{Mg}+\text{Fe})$  content (Jaumann, et al. 2012):

- The ferroan anorthosites: about 4.56–4.29 Ma BP, white-colored rocks rich in calcium, aluminium and in Fe and mainly composed of plagioclases with olivines and pyroxenes as minor minerals.
- The magnesian rocks: high Mg/Fe, they are younger (4.46–4.18 Ma BP) than ferroan anorthosites and overlap to them. They contain plagioclases, pyroxenes and olivines and according to their abundance they can be divided into gabbros and noritis (plagioclases and pyroxenes), dunites (only olivines) and troctoliths (olivines and plagioclases).
- The oldest basalt named KREEP (acronym for K (potassium), REE (rare earths) and P (phosphorus) composes the last group. The generic anorthositic terrae are rich in Th (Thorium) on the range of 1 to 2-3 ppm, and erupted only during the Imbrian period, they have brought a small volumetrically contribution for the supply of basaltic flows on the *Terrae*. On the contrary, a particularly very high Th (Thorium) concentration of 3–12 ppm characterized the *Procellarum* KREEP, typical of the *Oceanus Procellarum* and *Mare Imbrium* regions (*Figure 2.5*), erupted from at least 4.2 Ma to about 1 Ma. The high abundances of heat-producing elements within the *Procellarum* KREEP terrae are likely the cause of extensive magmatic productivity and volcanic longevity within this region (Barnes, et al. 2012, Jaumann, et al. 2012).

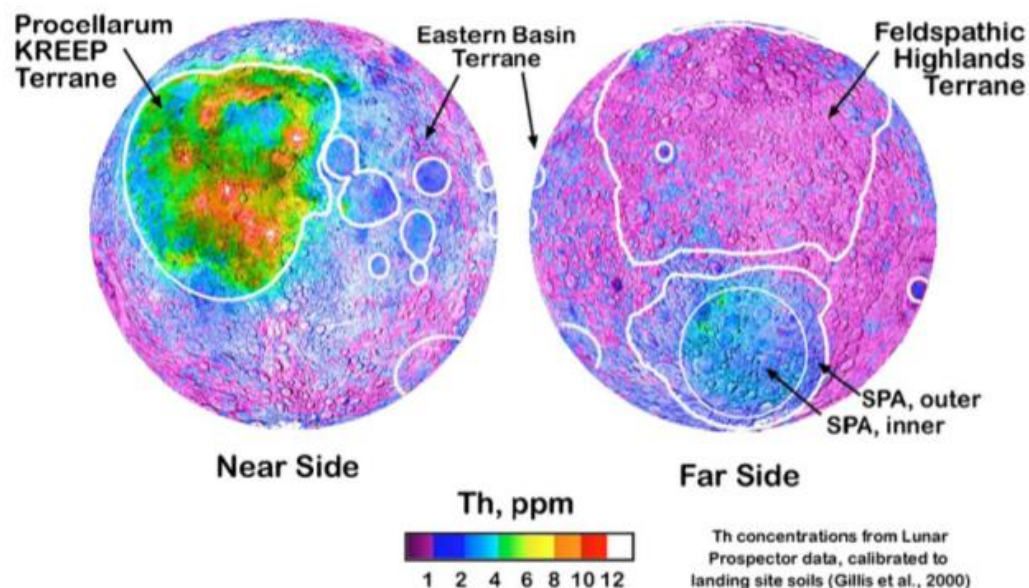


*Figure 2.5: The major lunar surface terrae as inferred from the distribution of Th. (Jaumann, et al. 2012).*

### **2.2.2 Upper and Middle mantel**

The chemical composition of the silicate mantle is consistent with that of an olivine-pyroxene mixture. Data analysis of the upper and middle mantle conducted at first time by Apollo missions revealed an almost constant seismic velocity in the upper mantle and a more heterogeneously distribution in the middle mantle. This discontinuity is detected at about 500 km in depth which indicates a change in composition or a higher abundance aluminous and MgO-rich mafic silicates. However, this discontinuity has only been recorded below the KREEP of the *Oceanus Procellarum* and, if it had a global extension, it would only be a direct consequence of the differentiation during the first Moon formation. In the lower mantle, below a depth of about 1150 km, seismic waves are strongly attenuated. This attenuation has been interpreted in terms of a partial melt zone that extends down to the core-mantle boundary (Jaumann, et al. 2012).

### **2.2.3 The inner and outer core**

Little is known about the lunar core, but the low density of the Moon ( $3344 \text{ km/m}^3$ ) suggests that the satellite has only a small iron core compared to the Earth one. The application of recent seismological array techniques led to the identification of new reflected phases from the deep interior of the Moon. Data results shows a partial melt layer in the deep mantle, a liquid iron-rich core, and a solid inner core. Data analyses also suggest the presence of a small (1–3 wt. %,  $<500 \text{ km radius}$ ) metallic or dense silicate partially to full molten core (Jaumann, et al. 2012). The estimated size of the lunar core ranges from 290 km to 380 km, while the estimates of the outer core thickness have converged to  $\sim 90 \text{ km}$  in recent studies (Liu J. 2020).

Further studies are necessary to better understand the size, composition and state of lunar core.

## 2.3 Lunar geologic timescale

The Moon's eras are characterized by longer durations than the terrestrial ones, probably due to the absence of plate tectonics. Five eras were identified, each corresponding to an evolutionary phase of our satellite: Pre-Nectarian (PN), Nectarian (N), Imbrian (I), Eratosthenian (E) and Copernican (C) (*Figure 2.6*).

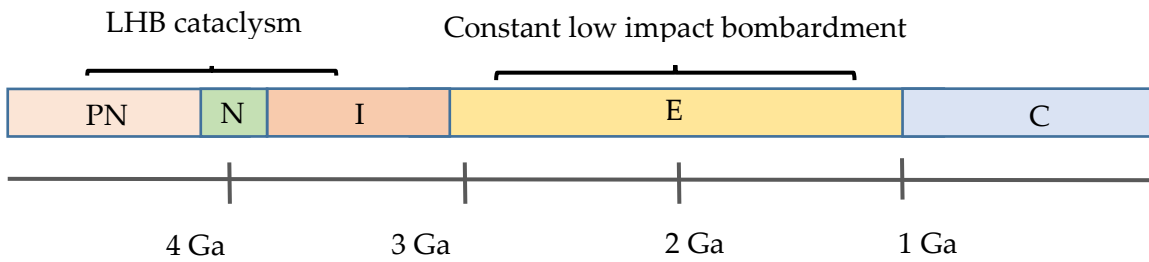


*Figure 2.6: Lunar timescale period compared to Earth timescale. N indicates the Nectarian period.*

### 2.3.1 Pre-Nectarian

The geological history of the Moon begins with its formation about 4.6 billion years ago, starting, after the Giant Impact, from a state of total fusion. The surface part of the Moon takes the name of Lunar Magma Ocean (LMO), which covers the entire surface. At this stage, magmatic differentiation began, which will later lead to the formation of *terrae*, composed mainly of Fe-anorthositic minerals (*Figure 2.7*). Due to the low density of the component minerals (plagioclase for the majority), being in a low viscosity magma, these minerals floated in the LMO forming giant lunar “rockbergs”. During this first phase the early Moon, in addition to the process of magmatic differentiation, was also subject to an intense bombardment (asteroids and comets) that caused the continuous disintegration of the rock masses that were forming. It is estimated that this phase of growth-disintegration began about 4.2 Ga and then slowly faded (*Figure 2.6*). During the Pre-Nectarian period (*Figure 2.6*), it is possible to lead back to the differentiation of the inner and outer core, as well as the differentiation between the upper and intermediate mantle (Geiss e Rossi 2013, Jaumann, et al. 2012, Lin, et al. 2017).

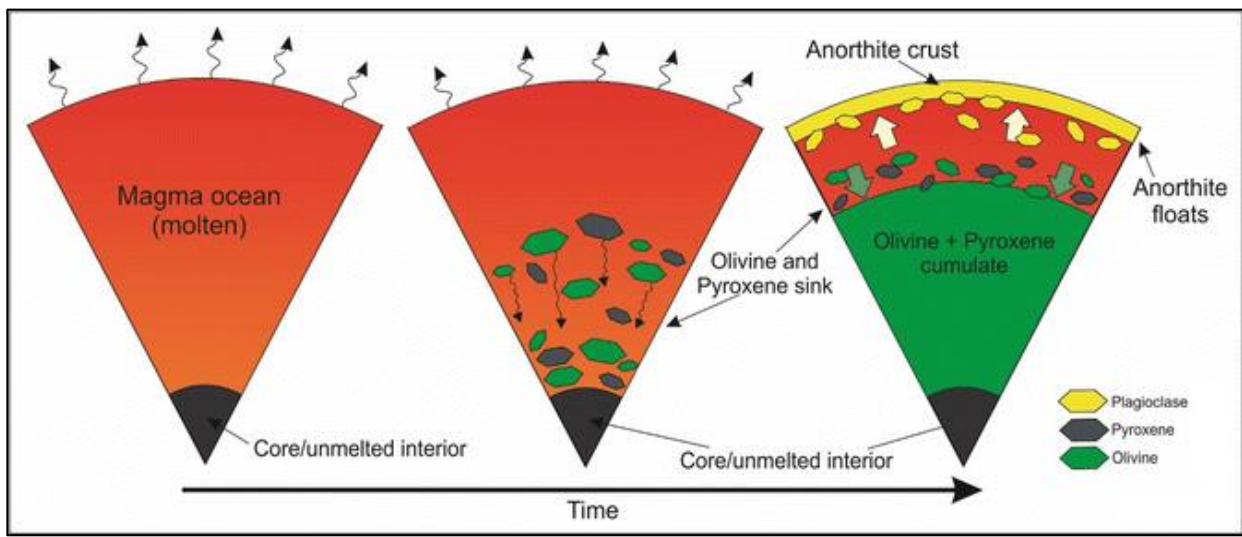


*Figure 2.7: Stages of the differentiation of the crust and the upper and middle mantle. Credit: (Lin, et al. 2017)*

### 2.3.2 Nectarian

This period is from 4.2 Ga BP (before present) to 3.9 Ga BP registered one of the most massive meteoritic bombardment named LHB (Late Heavy Bombardment). LHB consisted (*Figure 2.6*) where a few percent of the initial planetesimal population in the 1-2 AU zone (Astronomical units) from Neptunium zone have left their trajectory on high-inclined orbits in the inner Solar System (Morbidelli, et al. 2001).

Due to their inclined trajectory, and their consequent velocity, bodies as small as 400 m of radius could have effectively formed impact basins of 20 km of radius or more. The causes of this cataclysm are still under discussion, one hypothesis being that the objects responsible for the bombardment were coming from the trans-neptunian belt. Once their started to migrate, the orbit of the giant planets started to become more elliptic causing an unstable equilibrium which permitted the passage of the tras-neptunian meteorites. However, this model has been questioned and it has been shown that only a small percentage of these bodies actually reached the lunar surface. This quantity is not sufficient to explain the origin of the Aitken basin, *Mare Nectaris* and *Mare Crisium*, whose formation dates back to the LHB cataclysm. Whatever was the original causes of the LHB, it has likely upset the state of the lunar surface, shaping its larger basins and *maria* (Morbidelli, et al. 2001).

### 2.3.3 Imbrian

The Imbrian period is interesting from the volcanism point of view. It started as early as 3.9 Ga BP and ended approximately 3.1 Ma BP. Technically the period is divided into two epochs: Early Imbrian and Late Imbrian. In the first epoch Mare Imbrium has formed due to a massive impact with an external body, probably the last trace of the LHB event, as the greatest *maria* and basins. In the second epoch, Late Imbrian, the molten mantle below the lunar basins extruded with intense and massive lava basalt filled the depression. During the Imbrian period the volcanism of the Moon reached its peak, most of the volcanic structures, e.g. sinuous rilles, Marius hills, Mons Rümker (Figure 2.8 A; B and C) have formed.

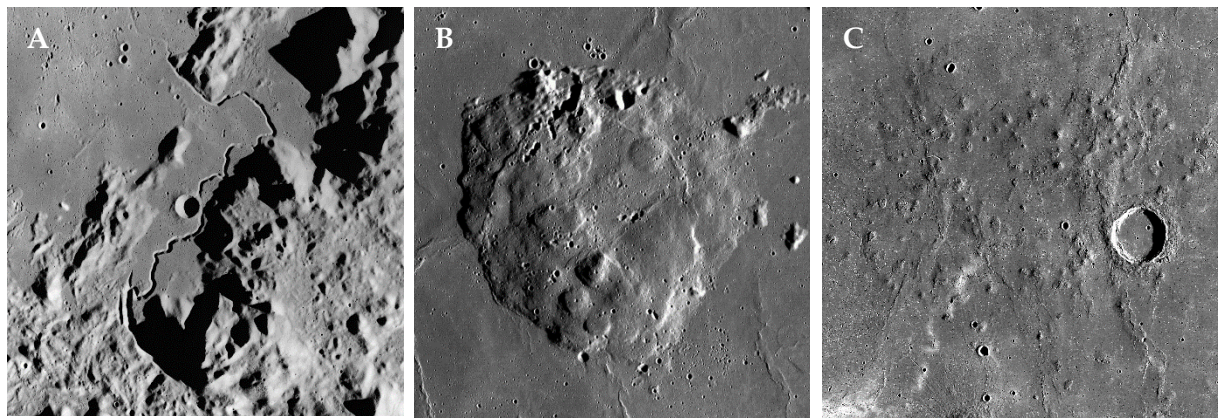


*Figure 2.8: A) Rima Hadley photograph from the Apollo15 not in scale; B) Mons Rümker, image from the LROC-WAC not in scale; C) Marius Hills, image from LROC-WAC not in scale. Credit: NASA/LROC.*

### 2.3.4 Eratosthenian

In relation to the duration of the other periods, this is the longest, starting at 3.9 Ga BP and ending at 0.9 Ga BP. In this period, we have the stabilization of the lunar crust with a cratering rate that is similar to the current one. Episodes of effusive volcanism alternate with those of explosive character and in this period begins the “lunar tectonics”. In fact, during the Imbrian the impact basin were fulfilled with basaltic lavas and this progressive increase in mass, caused also a progressive sinking of the basin structures. In response, extensive tectonic phenomena, thrust-belts and *graben* structures radially arranged in the basins themselves, were triggered (*Figure 2.9*).

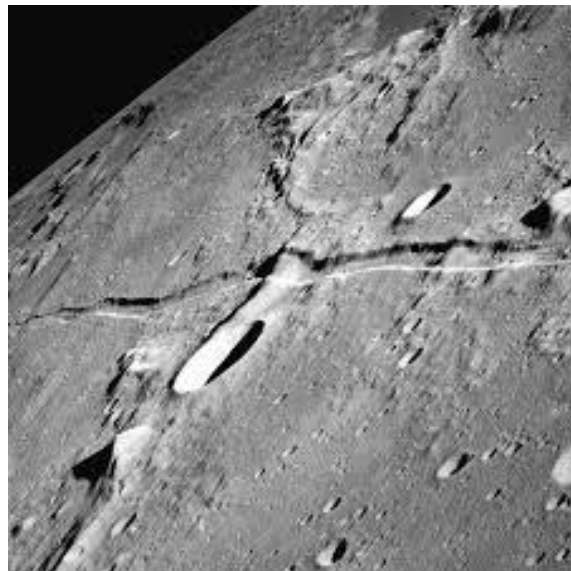


*Figure 2.9: Rima Ariadaeus (photo from the Apollo 11 mission) is a typical extensive structure on the lunar surface. Credit: NASA*

### 2.3.5 Copernican

This period, from 0.9 Ma BP to today, is characterized by a global stabilization of both crater formation rate and local seismicity. In fact, the near-side is subject to cyclic moon-quakes. It is estimated that the depth at which they occur is between 700-1100 km. It is thought that they are due to concentrations of tension stress caused by a decompensation between the mass present on the near-side and the far-side. Since the Apollo 11, 12, 14, 15, and 16 missions, seismometers placed on the near-side of the Moon recorded 28 shallow moonquakes from 1969

to 1977 (*Figure 2.10*). The quakes ranged from about 2 to around 5 on the Richter scale. As mentioned, the most-shallow moon-quakes have a cyclic character and they are thought to correspond to the lunar tides. In fact, the Earth-Moon system affects each other. The moon has as an effect on the earth the generation of tides in the seas and oceans; the earth, on the other hand, which has a greater mass than the moon, cause of moon-quakes of low magnitude (Mimoun, Wieczorek e Zarka 2012).

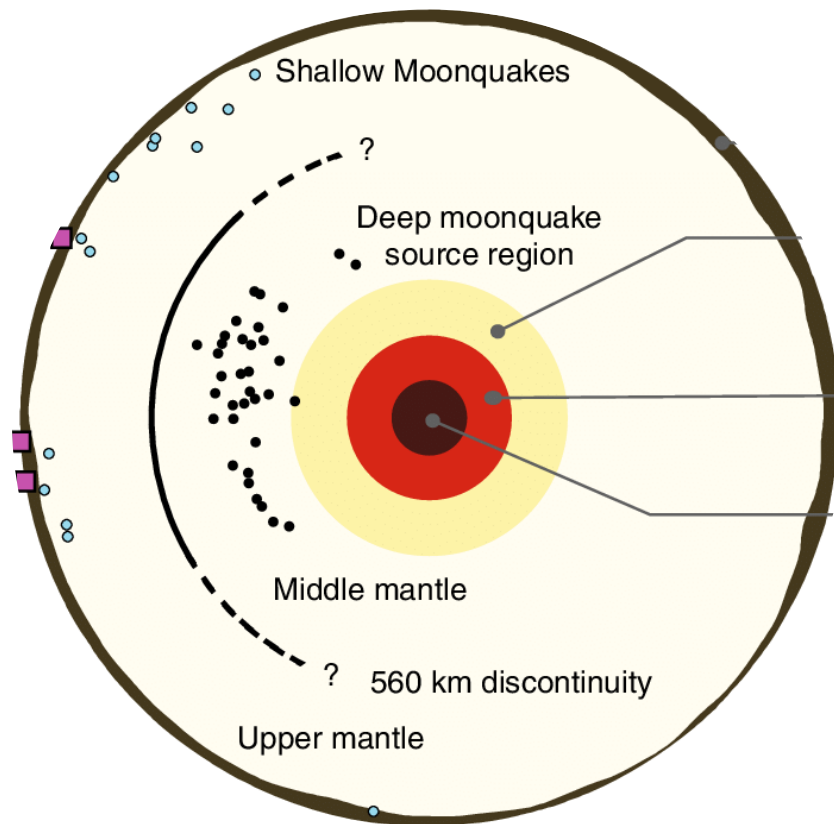


*Figure 2.10:* Apollo mission seismographs are indicated with the purple square dots. Black dots indicates the depth of the recorded moon-quakes. Credit: (Mimoun, Wieczorek e Zarka 2012)

# Chapter 3 – Morphologic description of the study area

The study area (*Figure 3.1*) is concentrated in the quadrant with latitude 0°N-60°N and longitude 270°E-300°E (*Figure 3.1*). NASA's LROC-WAC images have been used as a base map for the thesis, combined with the LOLA DEMs images (refer to Chapter 4- Data and Analyses for details). All the data are available on the official site of LROC: [wms.lroc.asu.edu/lroc/view\\_rdr/WAC\\_GLOBAL](http://wms.lroc.asu.edu/lroc/view_rdr/WAC_GLOBAL); DEMs are available through the website: <http://imbrium.mit.edu/EXTRAS/SLDEM2015/TILES/>.

Influenced by terrestrial geology nomenclature, the Moon's landforms were interpreted in structural terms with the same name and processes observed on Earth. The colour contrast, which characterized the near-side of the Moon, permits to distinguish two different morphological and structural units on the surface. The first is called *Maria* (singular *mare* from Latin) and are dark coloured basins that appear superficially smooth; the second unit called *terrae* (singular *terre* from Latin), and refers to the high topographic side of the surface, which is characterized by bright colours and appears wrinkle and heavily cratered. This distinction corresponds to the most common features of the near- and far -side, respectively. The near-side, is covered for 30 percent by maria and the *terrae* are mostly characterized by high reliefs and a few *maria* of modest size (i.e. *Mare Orientale*; *Mare Australe*; *Mare Ingenii*; *Mare Moscovicense* and *Aitken Basin*), which occupy only two percent of the entire surface. Compared to the entire surface of the Moon, *maria* occupy 16 percent while *terrae* occupy 84 percent (*Figure 3.2*).

In the study area (*Figure 3.1*), the basins and *maria* are predominant, *maria* have a volcanic origin; in fact, they have been made for the most of basaltic material came from several eruption during its evolution. An impact asteroid, instead, originated basins, after fulfilled by lava flows that originated *maria*. For the most, *maria* are circumscribed by round rims, the remain of the ancient impact rims (Wilhems 1987). In the study area, *terrae* are located mainly on the western edge of the quadrant and circumscribe the area of the *Mare Imbrium*. *Oceanus Procellarum*, with a north-south extension of about 2500 km and an aerial extension of 1.5 million km<sup>2</sup> dominates mostly the area. In the north-eastern side is located *Mare Imbrium*

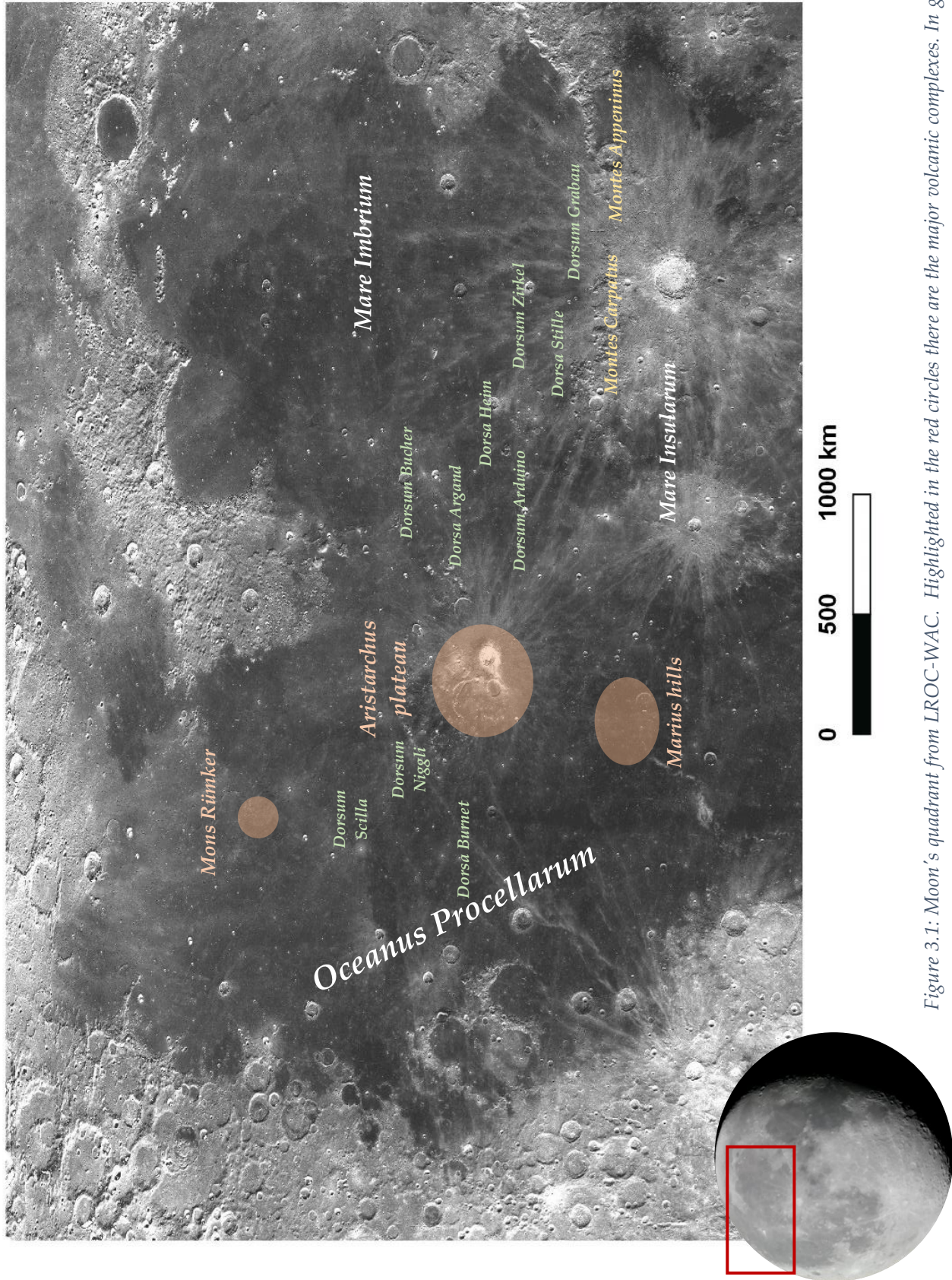
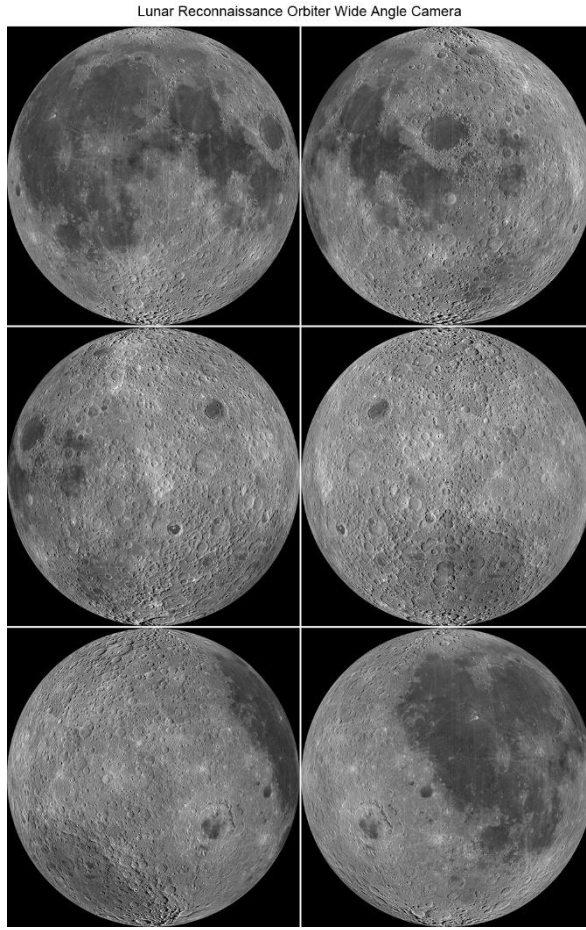


Figure 3.1: Moon's quadrant from LROC-WAC. Highlighted in the red circles there are the major volcanic complexes. In green are indicated the approximate location of *dorsa*, as for *montes* (in yellow), maria and oceans (in white) Credit: NASA



**Figure 3.2:** Six orthographic views of the Moon created from the new WAC global mosaic. From upper left to lower right the central longitude is  $0^\circ$ ,  $60^\circ$ ,  $120^\circ$ ,  $180^\circ$ ,  $240^\circ$ ,  $300^\circ$ . Credit: NASA/Goddard/Arizona State University.

and in the south-east between crater Copernicus and Kepler craters is located the *Mare Insularum* (Figure 3.1). Most of the *maria* have a circular or pseudo-circular shape (i.e. *Mare Imbrium*), bordered by arcuate or annular mountainous rims, which are the remain of the Imbrium crater basin (Wilhems 1987). The shape of the *maria* and their basins is directly linked to their own original processes. The basins have the characteristic circular and pseudo-circular shape of an impact crater; *maria*, instead, originated from effusive volcanic activity occurred inside the depressions created by the impact basins. *Oceanus Procellarum* represents an exception due to its non-circular, not well-defined shape. Recent studies from GRAIL (Gravity Recovery and Interior Laboratory) have contested the theory that the Oceanus Procellarum was formed because of an asteroid impact (Deutsch, et al. 2019). GRAILs data have shown that a complicated system of faults arranged at the edges of the region, in a pseudo-rectangular formation with angular intersections, are present below the surface basaltic layer. The origin

would therefore be magmatic-tectonic, caused by thermal stress. In this region, in fact, a thermal flux is estimated to be much above average compared to the rest of the near-side surface (Andrew-Hanna, et al. 2014).

The near side of the lunar surface may appear almost flat and devoid of any significant morphological structure; however, using high-definition images, it is possible to observe an extraordinary variety of structures, many of which are very similar in appearance and origin to the terrestrial ones. These structures can be summarily classified according to their volcanic or tectonic origin.

*Maria* are rich in volcanic structures similar in appearance to those of Earth. They can be distinguished essentially in domes and cones structures, crater chains or *catenae* and sinuous rilles. In the same way, inspired by terrestrial tectonic structures, it is possible to distinguish wrinkles ridges, graben and crater-floor fractures. Both volcanic and tectonic structures can be found mainly in the maria, with the exception of some families of faults that, instead, are located in the western zone at the edge of the *Oceanus Procellarum* and on the eastern margin of *Mare Imbrium*. A description of these volcanic and tectonic structures is reported in the following.

### 3.1 Volcanic structures

It is possible to recognize four main types of volcanic structures that occur frequently on the lunar surface: domes and cones structures, crater-chains or *catenae* and sinuous rilles.

#### 3.1.1 Domes

These structures have typically circular shape and dome-like morphology, have ring-like moats encircling them, typically tens to hundreds of meters in diameter and a few meters to ~20 m deep, are organized in clusters, occur mainly on lunar maria with similar composition of the surrounding mare basalts. Domes seem to float on the surrounding moat, and appear very young (~25 Ma) if compared with the ancient age of the surrounding maria (~3.2 Ga) (Zhang, et al. 2017).

One of the most evident characteristics is their grouping in certain areas of the lunar surface. Clusters of domes have been found in *Mare Tranquillitatis*, *Fecunditatis*, *Imbrium*, *Humorum*, *Nubium*, *Austral*, *Marginis* and in *Oceanus Procellarum* (Figure 3.3).

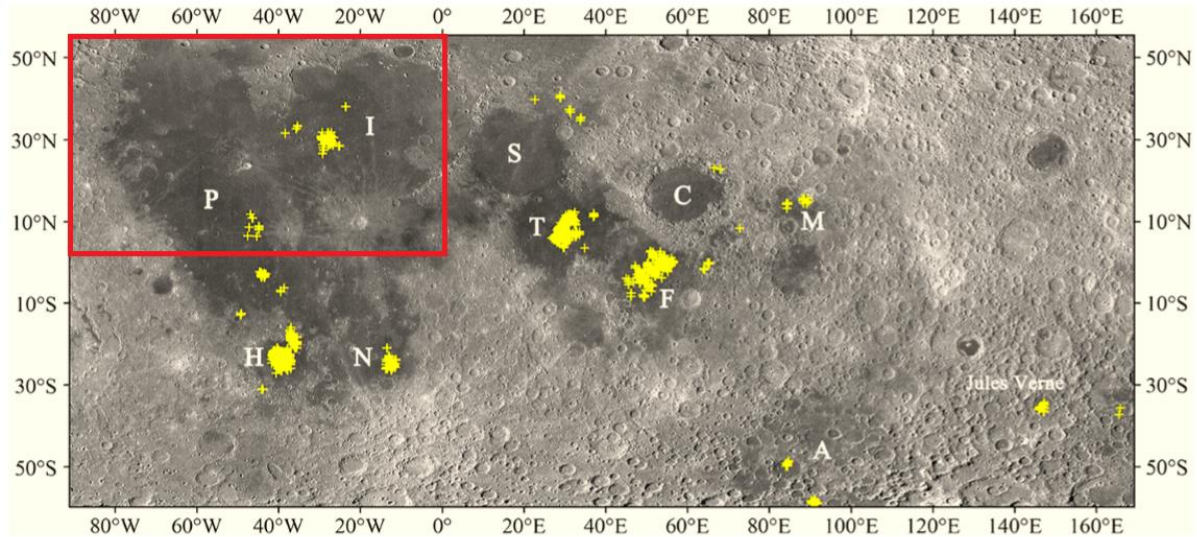


**Figure 3.3:** LROC WAC mosaic showing the distribution of about 2600 dome features identified in lunar maria. *Imbrium* (I), *Serenitatis* (S), *Crisium* (C), *Tranquillitatis* (T), *Fecunditatis* (F), *Humorum* (H), *Nubium* (N), *Marginis* (M), *Australe* (A), *Oceanus Procellarum* (P) are labelled (Zhang, et al. 2017). Study area of this thesis are highlighted on the red square.

There have been hypothesized four possible scenarios for the formations of these structures:

- (1) they are composed of material of a different, more viscous composition and emplaced in the period following mare basalt emplacement.
- (2) their very recent small geological eruptions that occurred several billion years after the laying of the mares' lava flows.
- (3) they are small squeeze-ups features formed at the time of the original flow emplacement;
- (4) they are developments of magmatic foams below a cooling lava flow surface and extrusion of these to form the mounds and moats as the flow evolved (Zhang, et al. 2017).

### 3.1.2 Cones

These structures (*Figure 3.4 A-B*) are exceedingly small in elevation and in extension. Their morphology resembles small cinder cones and volcanic domes on the Earth, but they may form differently, as for the dome's structures. the formation mechanism on Earth involves small eruptive explosions, the material of which falls in the immediate vicinity of the eruptive point. On the Moon, on the other hand, due to the low gravity, the same mechanism would involve the scattering of material miles away, leaving little material in the immediate vicinity of the central peak. Here, most of the domes and cones appear to be made of basalts and cones appear associated with domes, gathered in cluster.

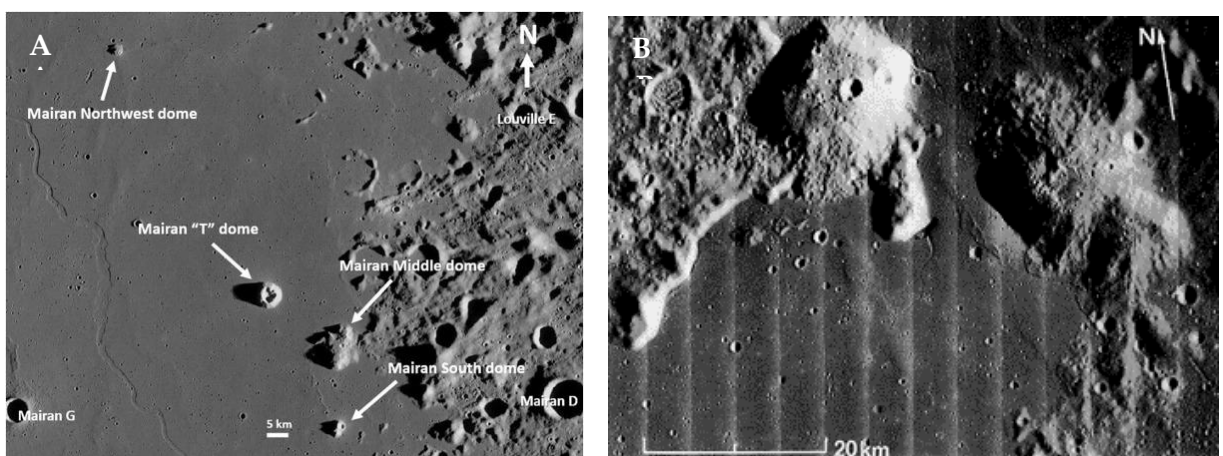


*Figure 3.4: A) Mairan middle domes (Boyce, et al. 2018); B) Gruithuisen domes and cones Credits: <http://volcano.oregonstate.edu/book/export/html/999> (Wilhems 1987).*

### 3.1.3 Volcanic systems

It has always been considered that the volcanic activity on the Moon, took place mainly as an effusive activity, with basaltic flows coming out of the fissures in the crust and filling the topographic baselines on the lunar surface. Most of the volcanic structures are concentrated in small clusters on selected area on the lunar surface, and typically their dimension are around 2 to 10 kilometres in diameter (Spudis, McGovern e Kiefer 2013). The areas with the highest concentration of volcanic morphotypes in the study area are essentially four: The Mons Rümker, the Aristarchus plateau, Prinz complex and the Marius Hills.

Mons Rümker (~70km in extent, centred at 40°N, 58°W) is a volcanic complex located in the northern Oceanus Procellarum and composed by almost 30 blister-like landforms (Spudis, McGovern e Kiefer 2013), formed on the top of a “kipuka”<sup>6</sup> surrounded by lava flowed in the northern Procellarum, which covered the basal area of the complex (*Figure 3.5*). The age of *Mons Rümker* dates to about 3.4 Ma years ago, much older than the surrounding sea of lava.

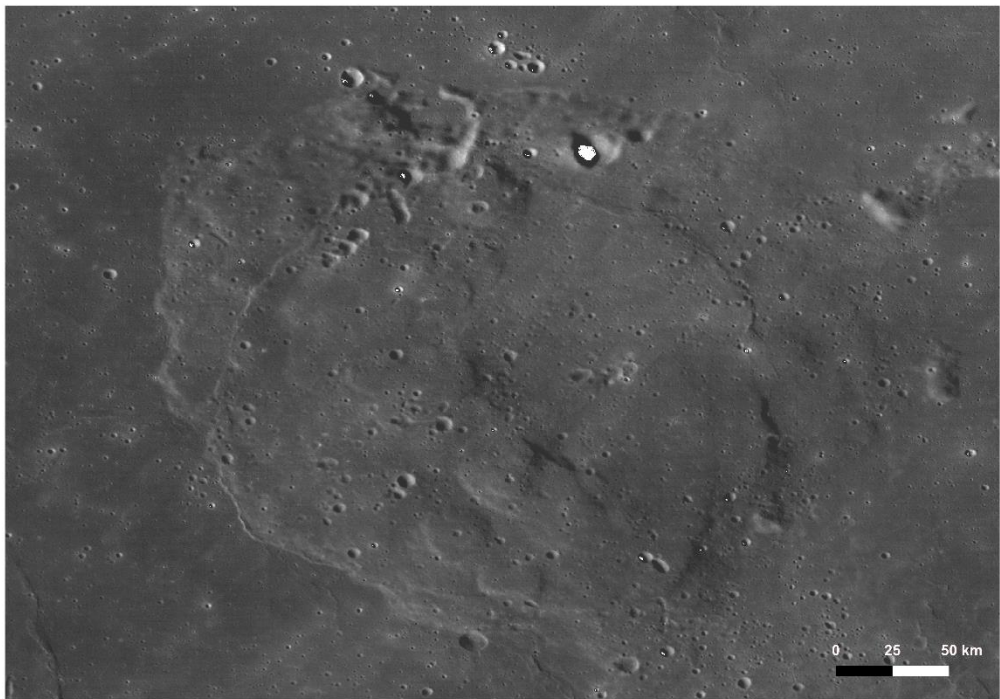


*Figure 3.5: The Mons Rümker overview, LROC-WAC image. Credits: NASA-LROC WAC.*

<sup>7</sup> The word kipuka has a Hawaiian origin like others terms like ‘a’ā and pāhoehoe, related to volcanology. A kipuka is an area of land surrounded by one or more younger lava flows. A kipuka forms when lava flows on either side of a hill, ridge, or older lava dome as it moves downslope or spreads from its source. Credit:

The low shield morphology resembles the volcanic shield on the Earth, there are no evidence of a specific source vent on the area, but the pit crater on the north of the structures may be a collapse pit crater. On the south and in the north of the structures (*Figure 3.6*) are located thirteen domes which did not presented the central pit crater, while on the south three of them presented a potential source vent. The area does not show an association with other volcanic structures i.e. sinuous rilles, but the surrounding mare basalt could have covered these structures (Spudis, McGovern e Kiefer 2013).

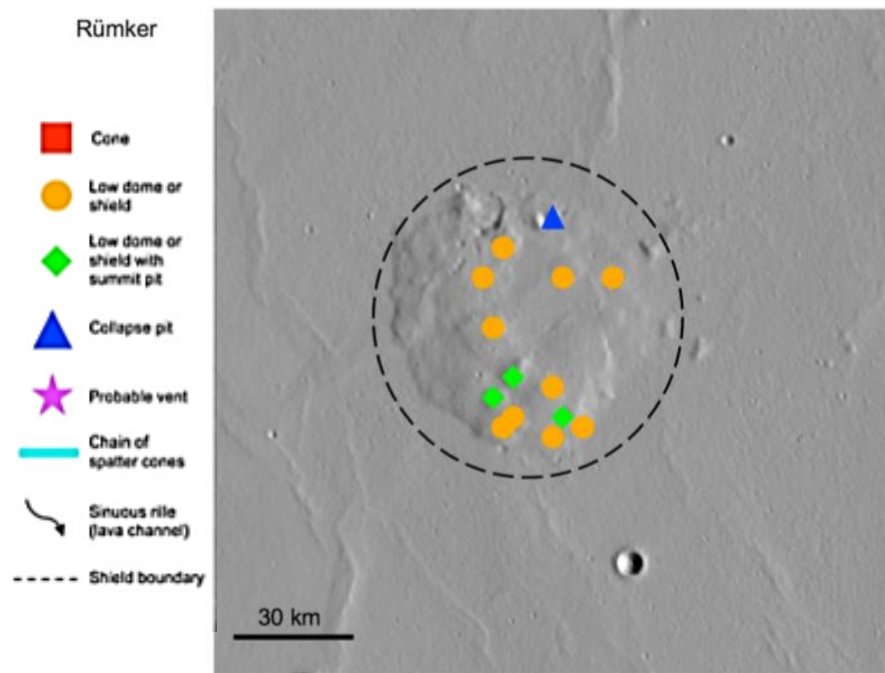


*Figure 3.6: Volcanic features of Mons Rümker, (Spudis, McGovern e Kiefer 2013).*

The Aristarchus Plateau (~250km; 25°N, 50°W) is an uplift block formed during the formation of the Imbrium basin. The area has been affected by massive volcanic eruptions, underlined by the marked presence of sinuous rilles (*Figure 3.7*). Vallis Schröteri (*Figure 3.8*), the biggest rille of the complex, shows at least two phases of eruptions, the first stage is represented by the main rille, the second stage is represented by the inner rille, both originating apparently by the Cobra Head source vent (*Figure 3.8*); suggesting a multi-phased volcanic evolution. The area present numerous secondary volcanic structures, such as mounds and pit craters and outcrops of the basement below, exposed by the lifting action that has affected the area.

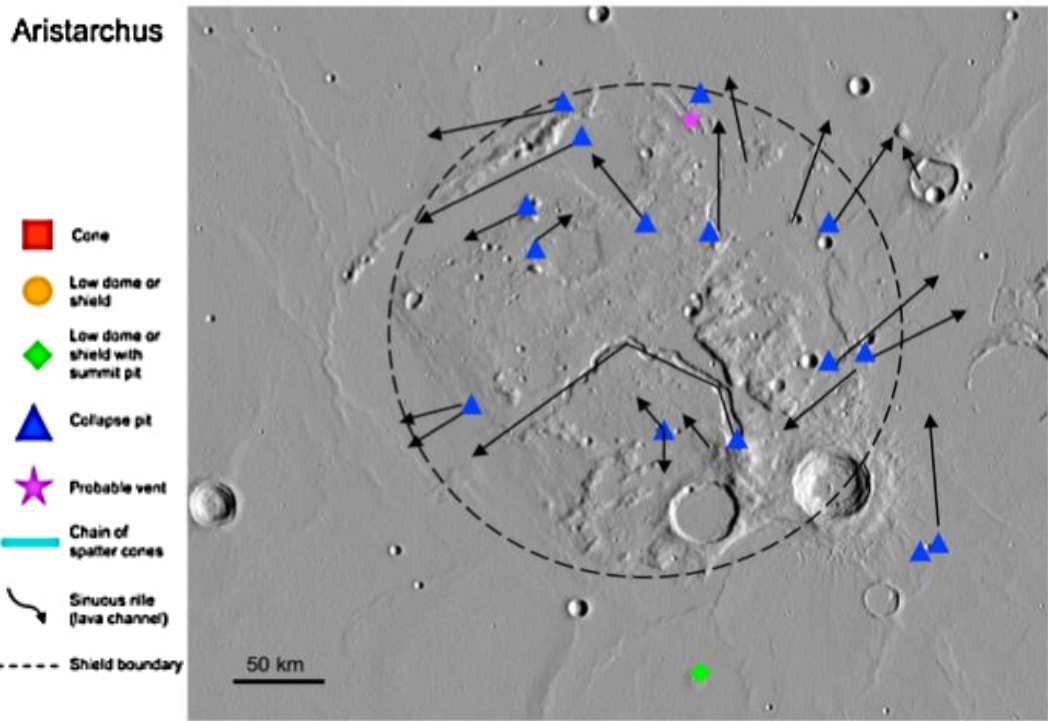


*Figure 3.8: Volcanic features of Aristarchus Platea complex. The arrows in black indicate the direction of the flow (Spudis, McGovern e Kiefer 2013).*

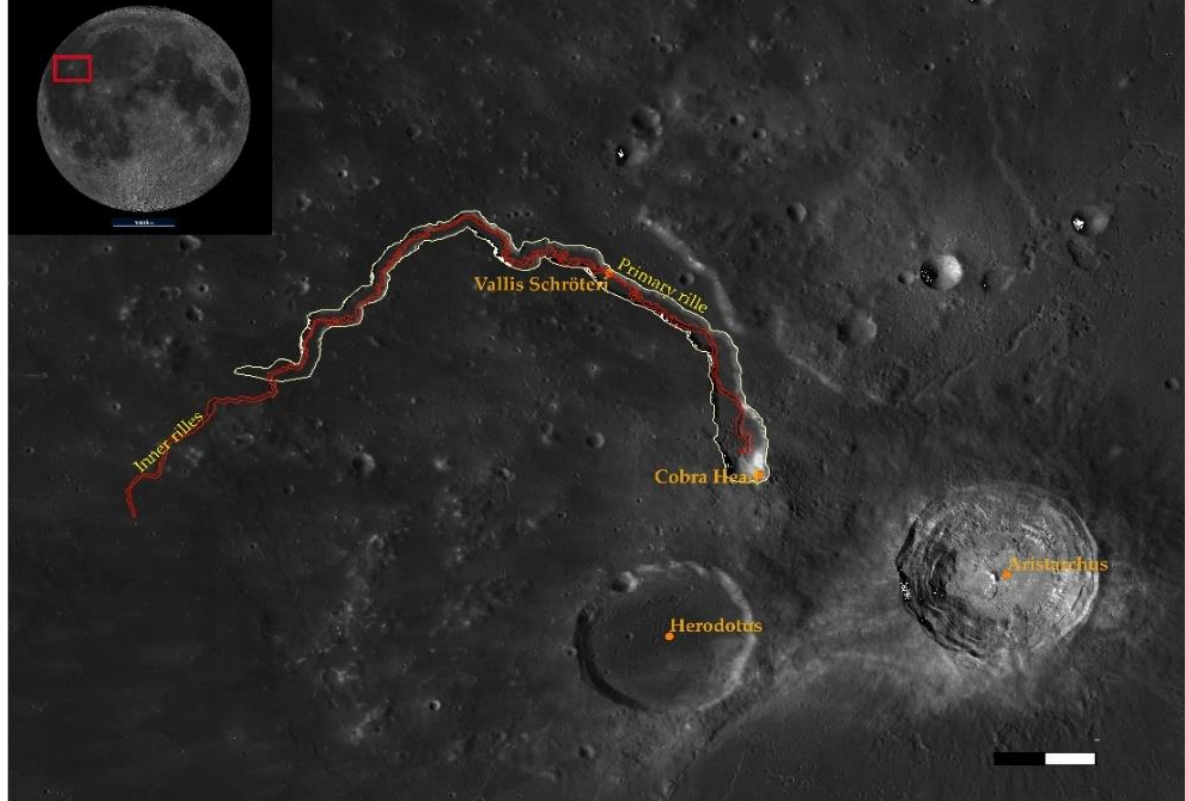


*Figure 3.7: Aristarchus Plateau LROC-WAC images with the mapped sinuous rilles.*

However, due to its shape, Aristarchus plateau seems to be a proto-volcano shield not well developed, as also demonstrated by its topographic profile of 240 km extension for about 2 km in height.

Prinz complex (~150km in extent; 26°N 43 °W) is in the north-eastern area of the Aristarchus plateau and shows a similar structural assessment as Aristarchus system (*Figure 3.9*). It is located on a highland uplift, probably associated with the Imbrium basin; it is characterized by the presence of numerous sinuous rilles started from the Prinz crater rim, partially covered by mare basalt flow (*Figure 3.10*). The main sinuous rilles is characterized by the presence of an inner rilles, as for Vallis Schröteri on the Aristarchus complex. However, even all the similarity with the Aristarchus complex, there are no evidence of a direct connection between the two volcanic system (Spudis, McGovern e Kiefer 2013).

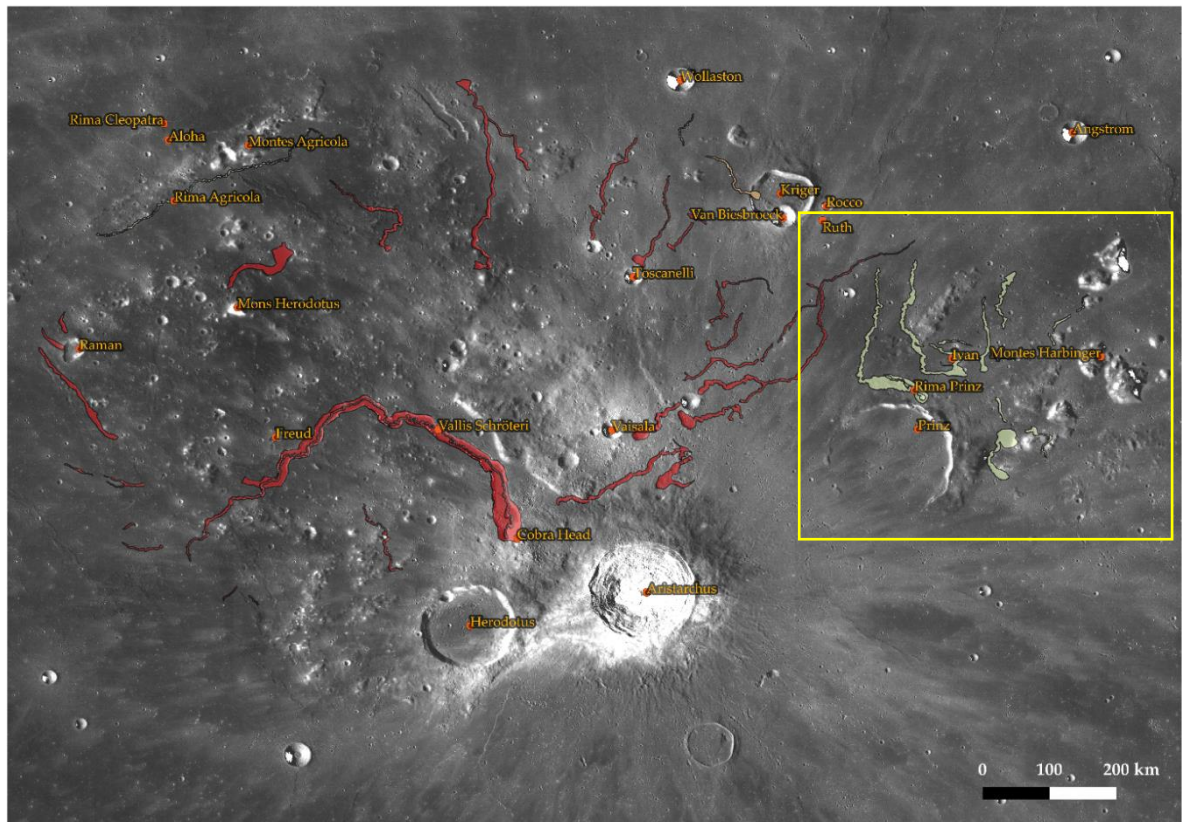


**Figure 3.9:** Aristarchus Plateau system and Prinz system, highlighted on the yellow square, located in the upper right side of the map. The sinuous rilles associated with each system are highlighted in different colours. Credit: NASA-LROC WAC images.

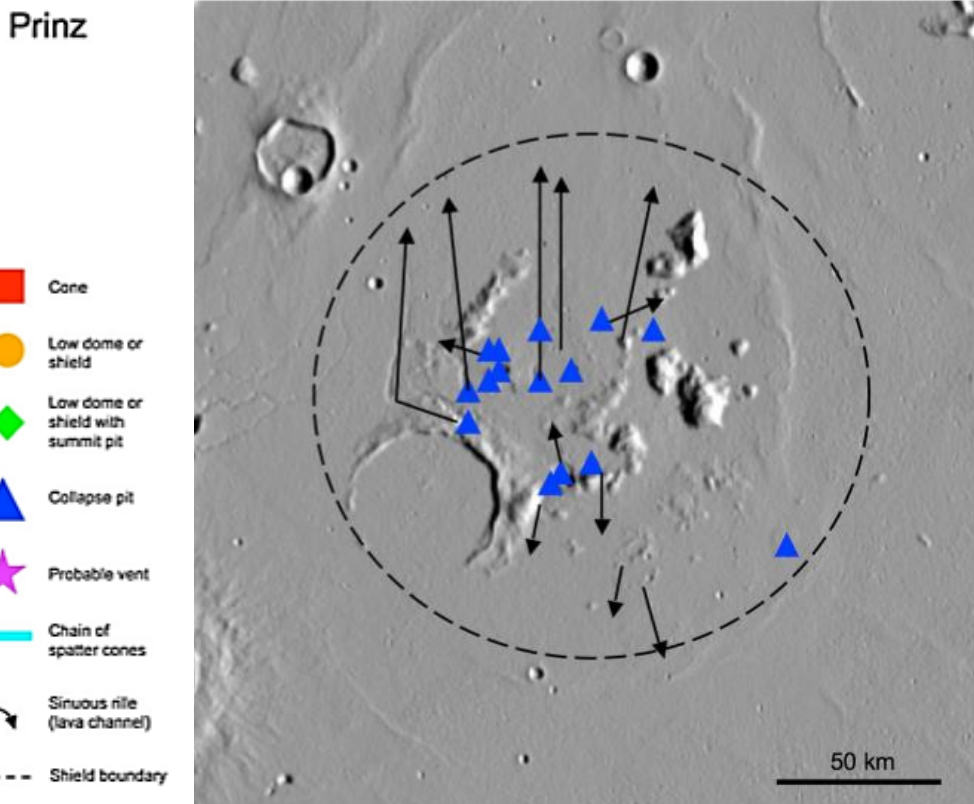


*Figure 3.10: Volcanic features of Prinz complex, the black arrows represent the direction of lava flows (Spudis, McGovern e Kiefer 2013).*

Marius Hills volcanic complex ( $14^{\circ}\text{N}$ ,  $52^{\circ}\text{W}$ ), located within Oceanus Procellarum, was one of the most active effusive system on the lunar surface, located within the *Oceanus Procellarum* (Figure 3.11). As a demonstration of the intense activity, there are many volcanic structures inside, including domes and cones that extend throughout the complex with a mean height between 200 and 600 meters and several sinuous rilles originating from evident defined source vents. The complex (Figure 3.12) extends for about 330 km with a pseudo-elliptical shape, with the highest peak located about 40 km northeast of the crater called Marius and an average elevation of about 2 km with respect to the surrounding maria. The overall shape is somewhat reminiscent of shield volcanoes present on the Earth's surface. The volcanic morphologies are positioned above the pseudo-shield, suggesting a posthumous formation, as emerged by the clear similarities with the shield volcanoes of Hawaii (Spudis, McGovern e Kiefer 2013). In the same figure a skylight is visible on the upper left side of the picture (Figure 3.12).

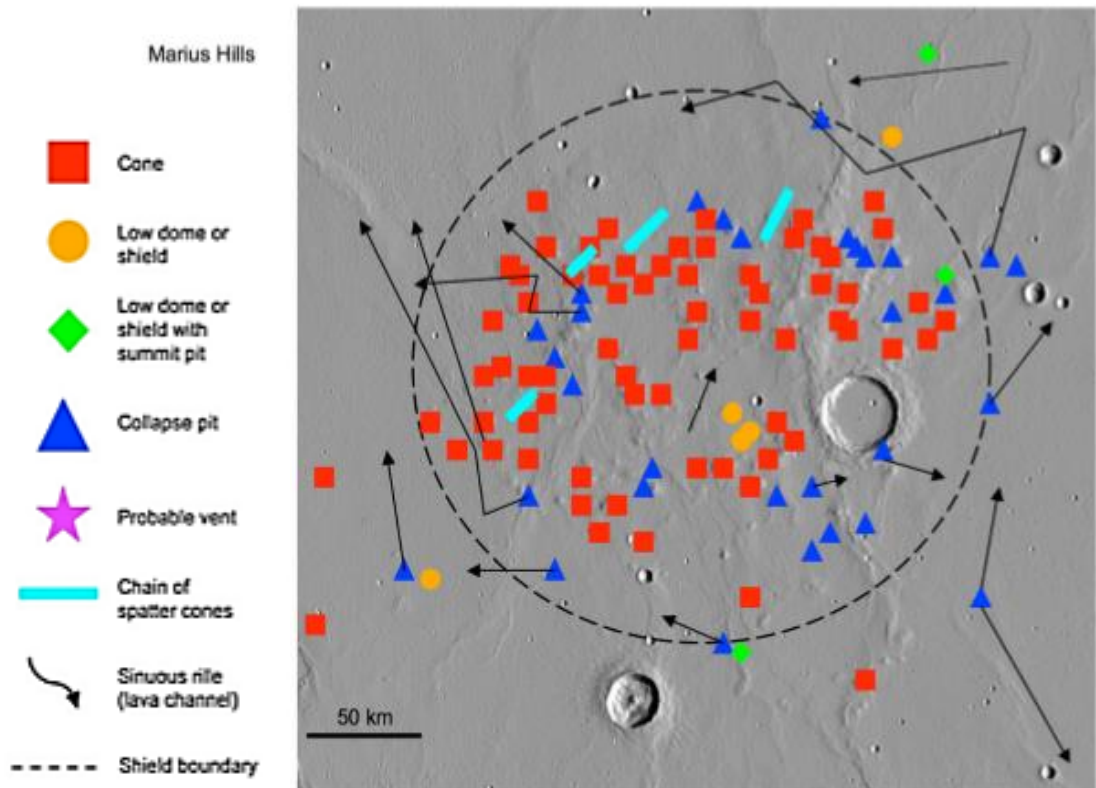


*Figure 3.12: Volcanic features of Marius Hills (Spudis, McGovern e Kiefer 2013).*

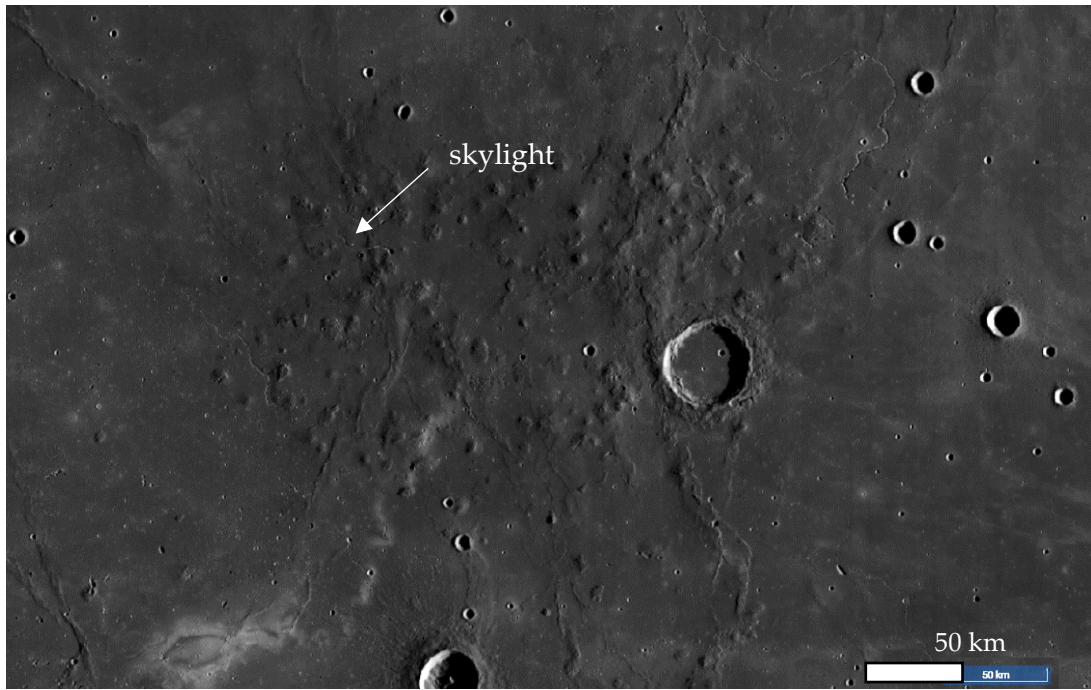


*Figure 3.11: Marius Hills complex overview by LROC-WAC images from quickmap.lroc.asu.edu. Red circle indicates the location of the skylight found in 2009 (Haruyama, et al., 2009). The white arrow indicates the location of the skylight.*

A skylight is defined as a hole in the lunar surface, mostly connected with the presence of a rille or a subsurface lava tube. This particular skylight, was discovered within Marius Hills complex and characterized by (Figure 3.13 A-B) 60 metres of diameter and 80 metres of depth, analysed by Kaguya SELENE Terrain Camera (TC) and classified as a potential lava tubes skylight. Skylights in general are considered as potential lunar site for future human bases, since they are shielded from meteorite bombardment, cosmic radiation, or particle implantation, they are expected to be in pristine condition, an environment with preserved lava composition, textures, and even volatiles (Haruyama, et al. 2009, Kaku, et al. 2017). The skylight was observed on the final part of a rilles, located in the north-western area (*Figure 3.13-A*) and it was hypothesized to be skylight opened on the roof of a lava tubes due a collapse mechanism (*Figure 3.13-B*). However, about the origin of skylights in general, several theories about the formation of mechanism have been considered including collapse due to meteoroid bombardments, emplacement of younger lava, moon-quake and tidal force. Despite the position of this skylight so close to a sinuous rille, for Marius Hills complex skylight, it was excluded a volcanic formation because there are no traces nor deposits around the hole that would suggest a local eruption. A fault- or dike-related formation was also excluded, because it would have created a linear series of pit craters and not one single skylight. In conclusion, due the alignment of the skylight with the sinuous rille (*Figure 3.13-A*) it is mostly plausible a formation due to the collapse of the top roof (Haruyama, et al. 2009).

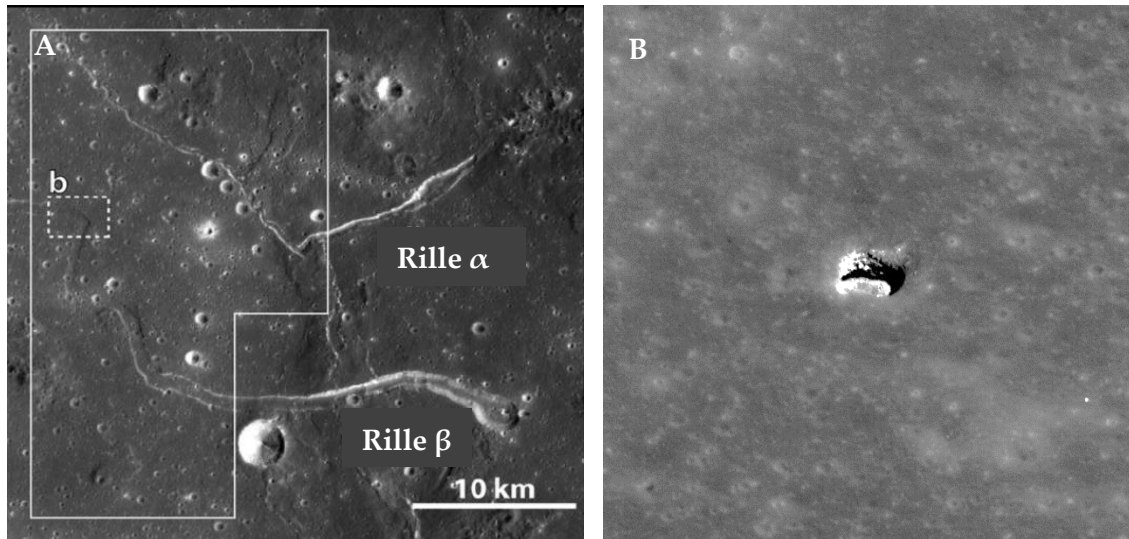


*Figure 3.13: A)* rille A and rille B in the north-western area of Marius Hills complex, b-square indicates the location of the skylight (Haruyama, et al. 2009). *B)* detail image of the skylight on Marius Hill, not in scale. Image from Kaguya/SELENE. Credits: NASA/Goddard/Arizona State University.

### 3.1.4 Crater chains or *catenae*

As defined by the Encyclopaedia of Planetary Landforms, crater chains are a linear series of three or more craters, having similar spacing and apparently similar age, formed by the impact of tidally disrupted bodies. They probably originate from small masses of debris of asteroids or comets that split during a close approach to a planet, separating into fragments that then hit the surface of the planetary bodies rather than escape into interplanetary space. Since there are no asteroids in the outer solar system, only comets can be the source of the crater chains on the moons of giant planets (Richardson e Hoogenboom Hagen 2014). Evidence of this phenomenon can be found on other planetary bodies such Ganymede and Callisto (*Figure 3.14 A-B*).

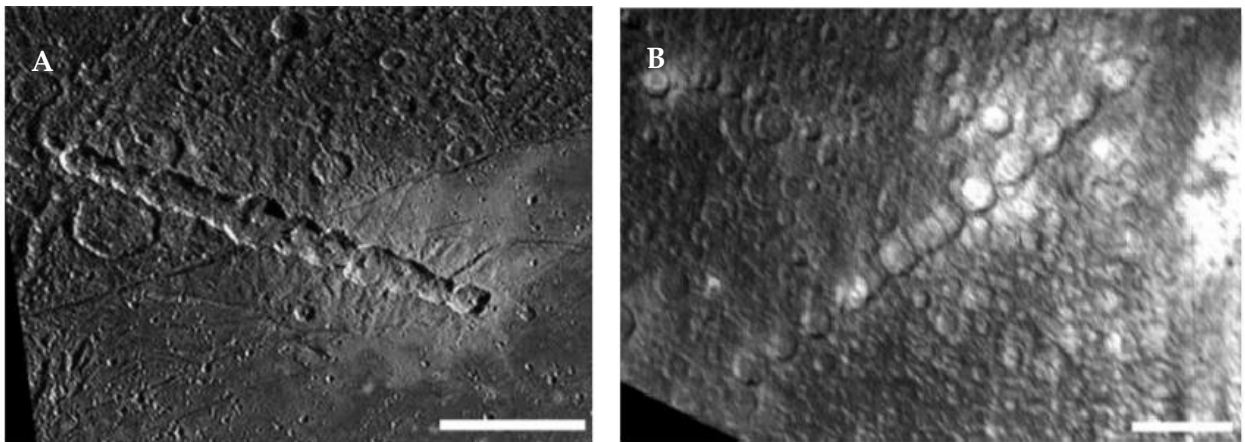


*Figure 3.14: A) Enki Catena on Ganymede A 160-km-long chain of 13 craters, at the boundary of old cratered surface and younger terrain, at 39N 346E. Scale bar 50 km. Galileo 03899211.01 (NASA/JPL); B) Six hundred and twenty-km-long Gipul Catena, Callisto, Scale bar 100 km. Voyager 1 image (NASA), (Richardson e Hoogenboom Hagen 2014)*

On the Moon, the principal mechanism could be reconducted to the collapse of craters associated with extensive tectonics (graben). However, most of the crater chains on the surface are disposed radially to large impact craters, secondary craters or along fissure due to intense eruptive activity, suggesting that even the meteoroid impact is a plausible cause of crater chains' formation (*Figure 3.15*). Recent studies suggest that the rate of formation of new crater chains is now arrested, but a high concentration of them were registered in the past, especially

during the Lata Heavy Bombardment period, where have been registered a high flux of Earth-crossing asteroids (Richardson e Hoogenboom Hagen 2014).

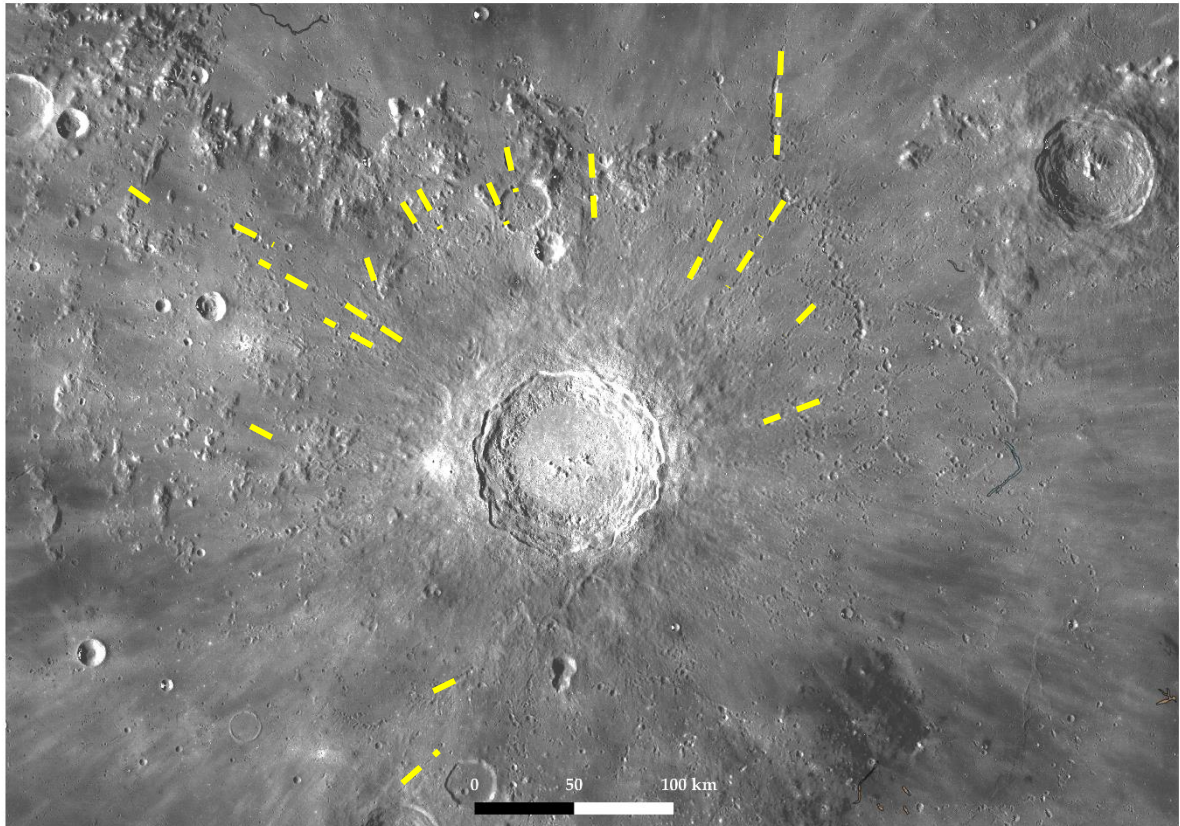


**Figure 3.15:** example of radial distribution of crater chains around Copernicus crater, positioned in the south-eastern side of the study area. Yellow dotted lines highlighted the position of crater chains around the crater.

### 3.1.5 Sinuous rilles

Sinuous rilles, that are the main subject of this thesis, are one of the most enigmatic and widespread structures on the lunar surface. They represent the remains of channels formed by lava that erupted in effusive, high volume volcanic event (Hurwitz, Head e Wilson 2012). Generally, they are narrow and steep channel-like morphologies that resemble terrestrial fluvial channels, mostly associated with a source depression vent, with steep slopes and flat bottom (Komatsu e Hargitai 2014). In this study 210 sinuous rilles were mapped in the area shown in *Figure 3.2*. The main and most relevant characteristic of rilles, which differentiates them from other similar structures, is essentially their appearance that resembles the terrestrial riverbed. However, beyond the purely visual aspect, sinuous rilles have features that differ according to their location and physical aspects (*Figure 3.16 A-B*). As far as for the rilles mapped for this thesis work their length varies from hundreds of meters to about 225 kilometres of the Rima Sharp (*Figure 3.16 A*).

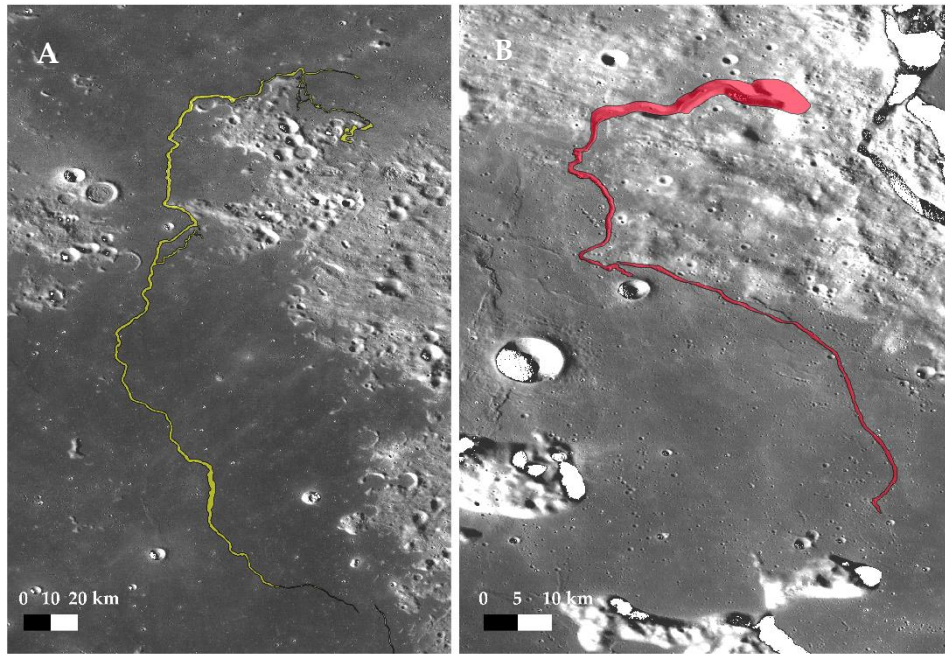


*Figure 3.16: A) Rima Sharp located in the north-eastern margin of Oceanus Procellarum, it is the longest sinuous rilles on the entire lunar surface. B) Rima Plato located in the north-eastern margin of Mare Imbrium close to the Plato crater. Credit: NASA-LROC WAC.*

The mean width of the mapped rilles is about 350 meters for an average depth of about 330 meters. The sinuous rilles have an incredible variance in shape and location (*Figure 3.16 A-B*; *Figure 3.17 A-B*), making it almost impossible to process an automated mapping, unlike craters (see § 1.3.2).

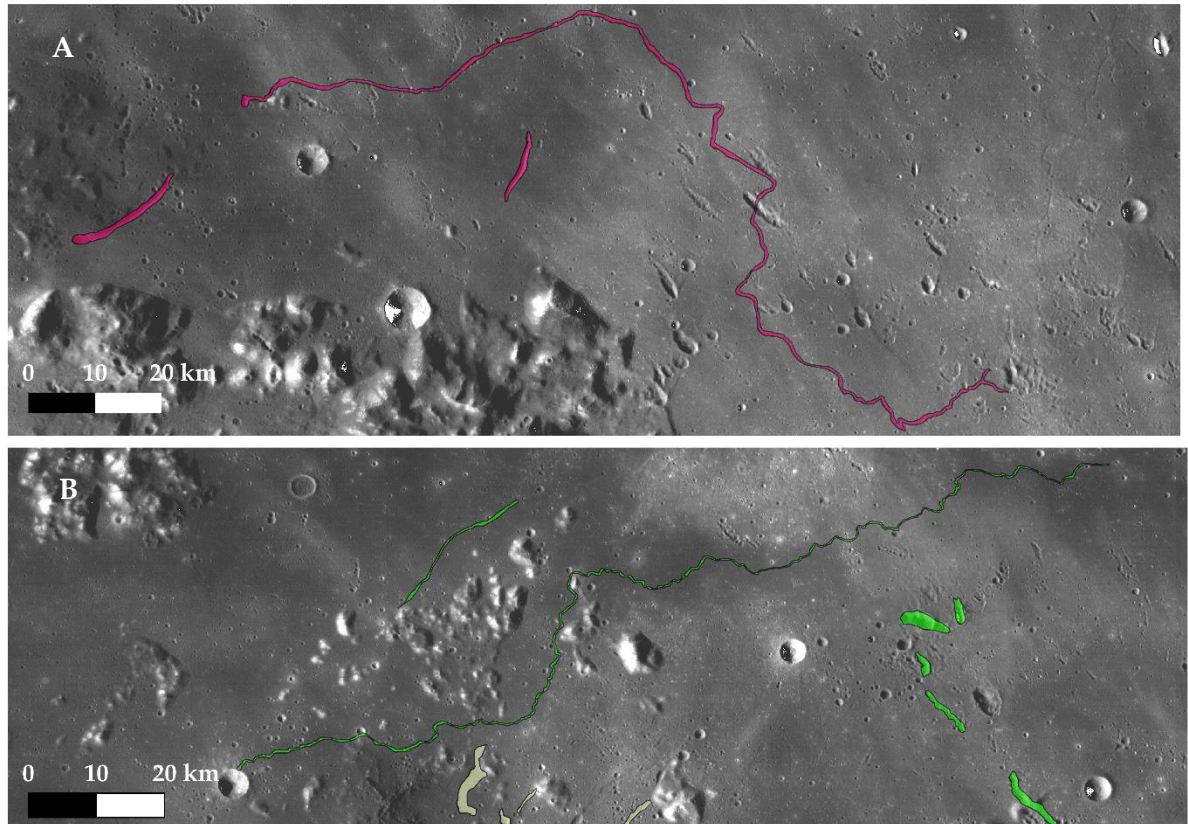


*Figure 3.17: A) Rima T. Meyer located in the southern area of Mare Imbrium and B) Rima Euler in the southern area of Mare Imbrium.*

Predominantly found in the margin of *maria* regions, it is widely accepted the volcanic origin of sinuous rilles; in fact, most of the mapped features present a pit interpreted as potential source vent and they seem to be concentrated principally around volcanic complexes. Details of sinuous rilles formation are still poorly understood, even though they are likely either lava channels or collapsed lava tubes. Lava tubes formed during the transport of lava under a stationary and solid crust, usually a collapse of the top roof made possible to identify them on the lunar surface, causing the alignment of the so-called skylights (Roberts e Gregg 2019). However, there are not consider for the classification of the sinuous rilles because do not respect the typical parameters (see § 4.2). Lava channels are the flow of lava between stationary

leaves and may or may not be covered with pieces or solidified mobile crust (Roberts e Gregg 2019).

Two formation mechanisms are hypothesized for sinuous rilles: constructive processes and erosive mechanism. The first consider the differential cooling of lava flows, the second one implies thermo-mechanical erosion lava channels, formed during a high-flow eruption of turbulent lava flood. The construction process involves lateral growth by differential cooling of the lava flow margins, leading to a centralized flow channelling. The erosion process is divided into mechanical and thermal. Mechanical erosion occurs through friction at the bottom of the channel between the flow particles and the substrate. Thermal erosion, on the other hand, occurs through the melting of the substrate having a lower temperature than that of the flow above (Kerr 2001, Hurwitz, Head e Wilson 2012). Several sinuous rilles, i.e. Vallis Schröteri, Rima Hadley in *Montes Appeninus* south-eastern of *Mare Imbrium*, and Rima Prinz in Aristarchus system, suggest a combination of constructional and erosional processes (Roberts e Gregg 2019, Hurwitz, Head e Wilson 2012).

The same morphologies have been observed on the terrestrial lava tubes and channel from Hawaii and Canary Island Lanzarote (*Figure 3.18 A-B*). In particular, long-live lava tubes on Hawaii have formed initially with the coexistent of pahoehoe<sup>7</sup> lobes with a preferred direction of flow as suggest the constructional origin. As lava continue to flows, a deepening of the bottom floor of the channel is observed because of thermo-mechanical erosion (Roberts e Gregg 2019). It is evident that the formation of sinuous rilles is due to a combination of processes related to the type and duration of effusiveness. Understanding their origin would be of great help in identifying the various phases of activity, duration and identify the various types of eruption, reconstructing the magmatic history of the Moon.

---

<sup>7</sup> Pāhoehoe (from Hawaiian [pa:’howe’howe], [16] meaning “smooth, unbroken lava”), also spelled pahoehoe, is basaltic lava that has a smooth, billowy, undulating, or ropy surface. These surface features are due to the movement of very fluid lava under a congealing surface crust. The Hawaiian word was introduced as a technical term in geology by Clarence Dutton. Credit: <https://en.wikipedia.org/wiki/Lava#P%C4%81hoe hoe>



*Figure 3.18: A) Nāhuku lava tubes, Hawaii Big Island-USA; B) entrance of the lava tubes named Cueva de los verdes, Lanzarote Canary Island. Credit: Fiorucci S.*

## 3.2 Tectonic structures

The lunar tectonism and magmatism resemble the Paleoproterozoic stage of the Earth development. Moon's period is divided into two main stages: the earliest (4.45–4.25 Ga BP) highland magmatism of the Moon and the second stage (3.9-3.2 Ga BP), characterized by extensive generation of mare basalts which fulfil the maria basins (Sharkov e Bagatikov 2000, Sharkov 2011). It is possible to distinguish, as for the oceanic and continental flood basalts of Earth, two varieties of chemical composition, low- and high-titanium mare basalts (Sharkov e Bagatikov 2000). The lunar mare magmatism is related to the ascent of mantle plumes of the second generation from the boundary between the liquid metallic core and the silicate mantle. The spreading of plume heads was probably responsible for the formation of large mare depressions with reduced crust thickness on the near-side of the Moon (Sharkov e Bagatikov 2000, Sharkov 2011). Two major types of tectonic structures were originated: upwelling areas developing in an extension regime and resembling terrestrial cratons and depressions between them (Sharkov e Bagatikov 2000, Sharkov 2011) accompanied by the formation of large areas of mare basalts. The mare structures are associated with an excess mass so-called mascons with a thinned crust above them. A second generation on plumes ascended on the shallow layer and spreaded out, causing a more extensive crust on the maria depressions. As a result, crustal material was packed at the outer parts and mountain morphologies were created at the margin with highlands (*Figure 3.2*), i.e. Montes Appeninus and Carpatus (Sharkov e Bagatikov 2000, Sharkov 2011).

Referring to lunar tectonics, there is no mention of the classic tectonics of the Earth's plates, but it can be understood as an adjustment of the basaltic crust following the various phases of volcanic activity that have characterized the evolutionary phases of the lunar surface. Three main tectonic structures can be identified on the lunar surface: wrinkles ridges, graben and crater-floor fractures.

Wrinkles ridges are linear to sinuous landform spreading in the *maria* regions (Figure 3.18, A-B) of the lunar surface. They can be hundreds of metres to hundreds of kilometres long and up to hundreds of metres wide. Wrinkle ridges form in compressional stress conditions and it is now widely accepted that wrinkle ridges express folded basalt layers overlying thrust faults (Lu, et al. 2019).

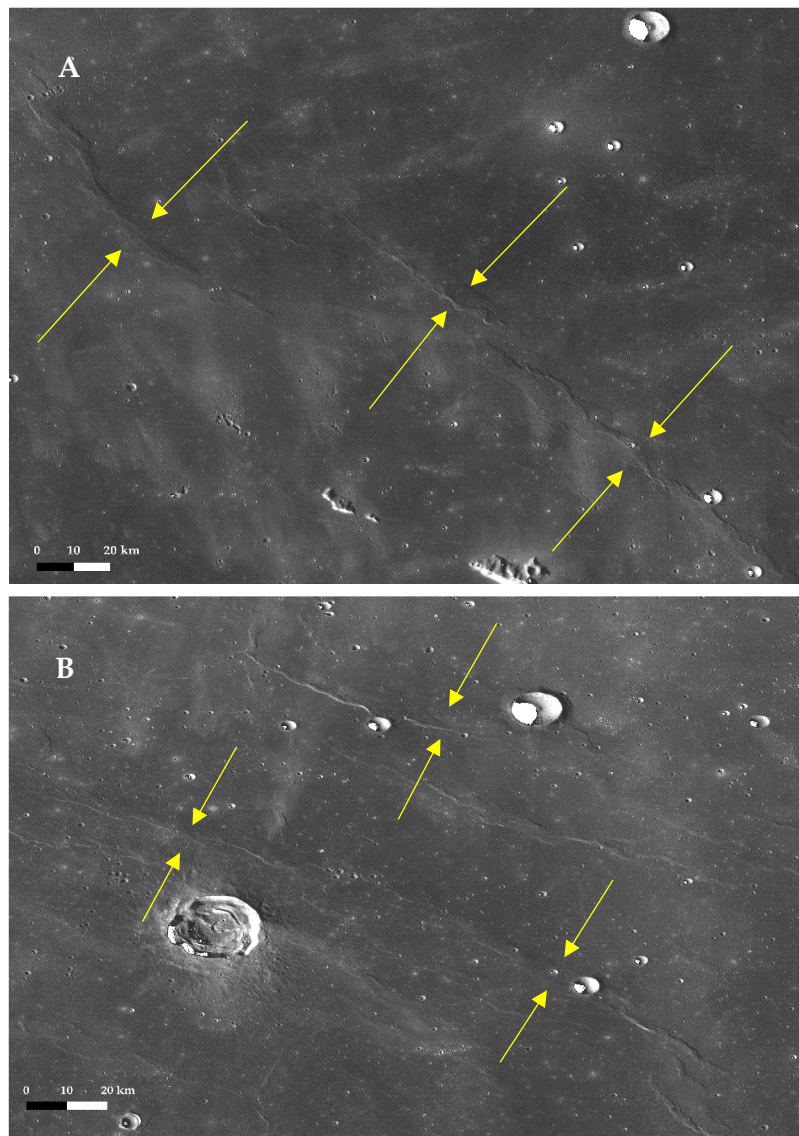
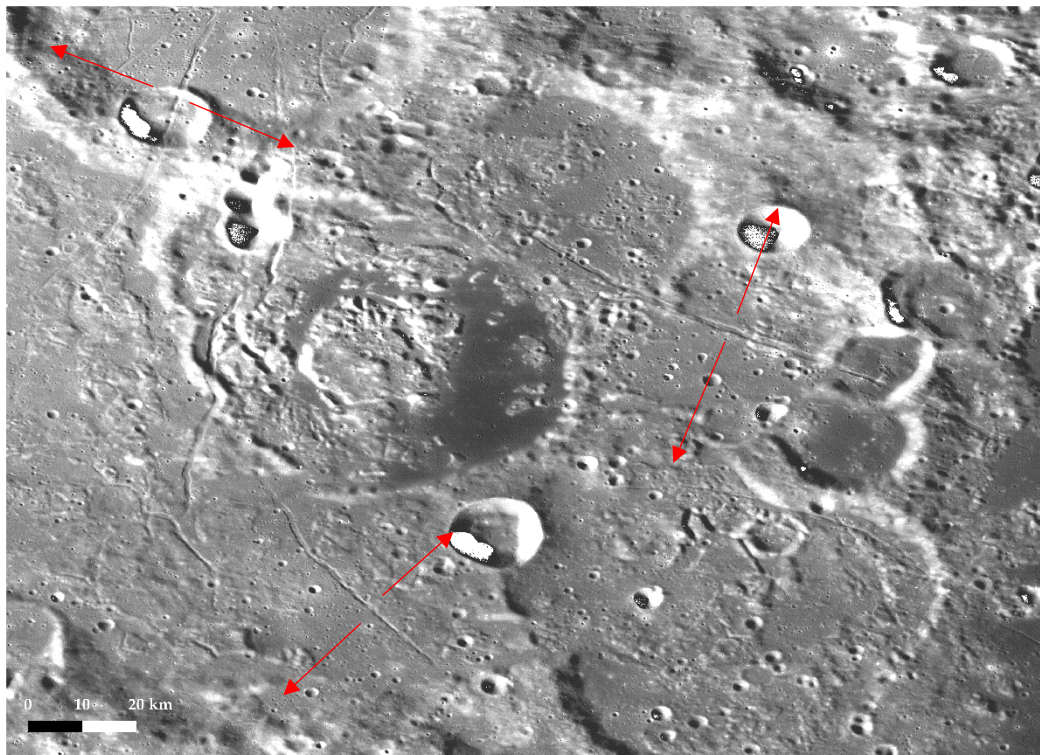


Figure 3.19: A) Wrinkles ridges in south-western area of Mare Imbrium. B) Wrinkles ridges on north-western area of Oceanus Procellarum. Yellow arrows indicate the compressional tectonism, responsible for the wrinkle's ridges formation. Scale bar values 10 km.

Graben are long extensive landforms formed at the margin of lunar maria and are the expression of an extensional tectonism, with the similar morphologic expression of Earth. Graben lengths were found to range from dozen up to hundreds of kilometres and often came across the margin highlands of mare basins (Cullingham e Klimczak 2019).



*Figure 3.20: A) system of grabens in the north-western margin of Oceanus Procellarum. Red arrows indicate the extensive tectonism. Scale bar values 10 km.*

Crater floor fractures could be considered grabens in a local scale, which occur inside impact craters (*Figure 3.20, A-B*) fulfil of basaltic lava during the eruptive phase of the magmatism of the Moon (Sharkov e Bagatikov 2000, Sharkov 2011). Their morphologies resemble the crack fractures occurred in the desert area of the Earth, due to the intense thermal excursion. Probably formed because of a rapid cooling of the magma inside the crater, have articulated branches with 90° angles and are located only inside the impact craters. Graben, instead, often cut across the underlying morphologies.

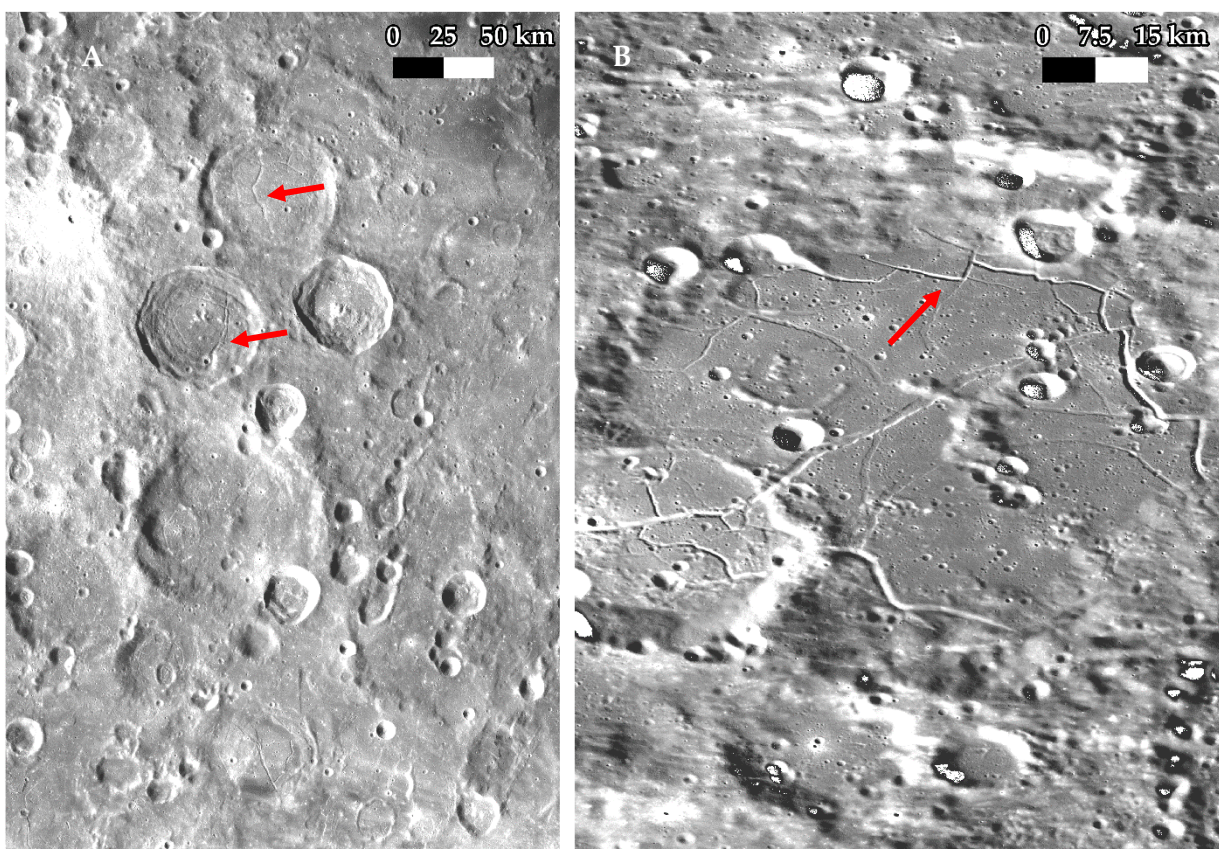


**Figure 3.21:** A) Crater floor fractures on the highland in the south-western margin of Oceanus Procellarum, highlighted in orange colour. B) well developed crater floor fractures in the north-western highland margin of Oceanus Procellarum. Red arrows in both images indicate the crater floor fractures.

# **Chapter 4 –Lunar rille's detection and classification**

This chapter will list and describe all data used for sinuous rilles mapping. NASA's LROC-WAC images, NASA's LOLA DEM (Digital Elevation Model) have been used. The Chinese data of Chang'E-2 the DOMs, corresponding to the NASA DEMs, have been used in the first phase of the Moon Mapping project. Given the limited availability of further images and digital models of the Chinese data, the American data were used to deepen the study and mapping of the sinuous rilles.

## **4.1 Data and Images**

LRO (Lunar Reconnaissance Orbiter) is one of the first missions as part of the LPRP (Lunar Precursor Robotic Program) project with the main purpose of creating permanent scientific missions on the lunar surface. The LRO mission began in October 2008 with the objective of obtaining a detailed, high-resolution mapping of the lunar surface, identifying potential sources of resources and analysing the lunar environment (Chin, Brylow, et al. 2007).

The LRO payload (Chin, Brylow, et al. 2007) includes (*Figure 4.1*):

- LOLA (Lunar Orbiter Laser Altimeter), used to determine the global topography of the lunar surface, slope gradients, local roughness and to research possible ice presence on the polar region.
- LROC (Lunar Reconnaissance Orbiter Camera) equipped with a narrow-angle camera (NAC) and a wide-angle camera (WAC).
- LEND (Lunar Exploration Neutron Detector) used to measure neutron flux from the lunar surface to search for frozen water and to measure radiation and study the lunar environment.
- DLRE (Diviner Lunar Radiometer Experiment) used to produce a detailed map of the temperature of the entire lunar surface with a ~300-meter horizontal resolution and to identify cold-traps and potential ice deposits.

- LAMP (Lyman-Alpha Mapping Project) used to provide a map of the lunar surface in ultraviolet, useful to search for water and ice in the polar areas and to map the permanently shaded area.
- CRaTER (Cosmic Ray Telescope for the Effects of Radiation), which studied the effects of galactic cosmic rays

LROC-WAC and LOLA images were used as the base map for the recognizing of the sinuous rilles. A description of the only two instruments used in this thesis will be provided below,

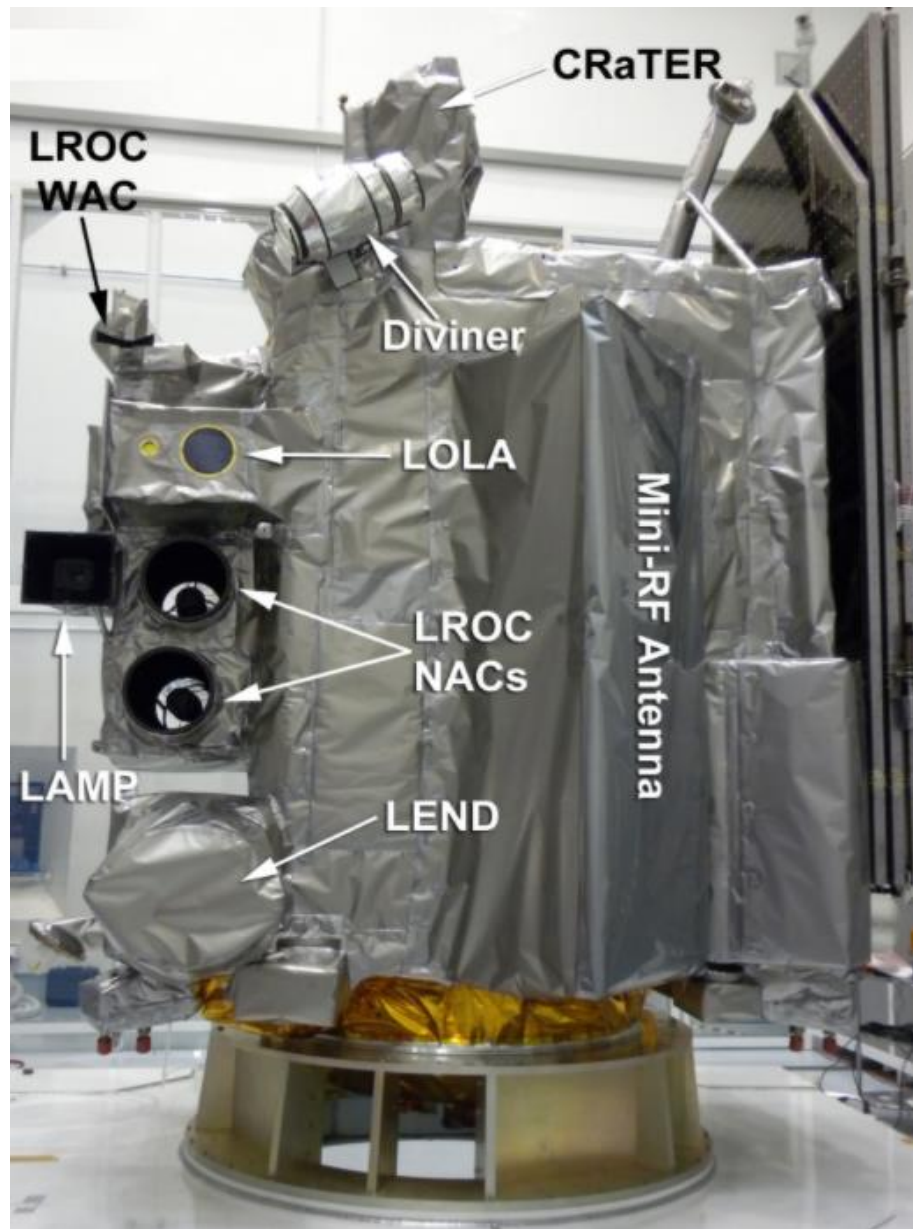


*Figure 4.1: LRO payload indicate with the acronym of each instruments. Credit: <http://lroc.sese.asu.edu>.*

referring to the bibliography for further details on the other instruments. For further information on the other instruments, please refer to the cited bibliography (Chin, Brylow, et al. 2007, Riris, et al. 2008, Robinson, et al. 2020).

#### 4.1.1 Lunar Reconnaissance Orbiter Camera- Wide Angle Camera (LROC-WAC)

The LROC objectives can be reassumed in eight points (Chin, Brylow, et al. 2007):

1. Landing site identification and certification and identification of meter scale hazards, (e.g. large boulders, roughness of the terrain).
2. Mapping of permanent shadow and sunlit regions.
3. Meter-scale mapping of polar regions.
4. Repeated observations to enable derivation of meter-scale topography.
5. Global multispectral imaging to map minerals.
6. Global morphology base map.
7. Characterize regolith properties.
8. Determine recent small impactor rates by re-imaging regions photographed with the Apollo Panoramic Camera (1–2 m/pixel resolution).

LROC is equipped (*Figure 4.2*) with two narrow-angle cameras (NAC) with a spatial resolution of 50 centimetre/pixel, covering almost the 10% of the surface and 100% at 85° latitude; a WAC

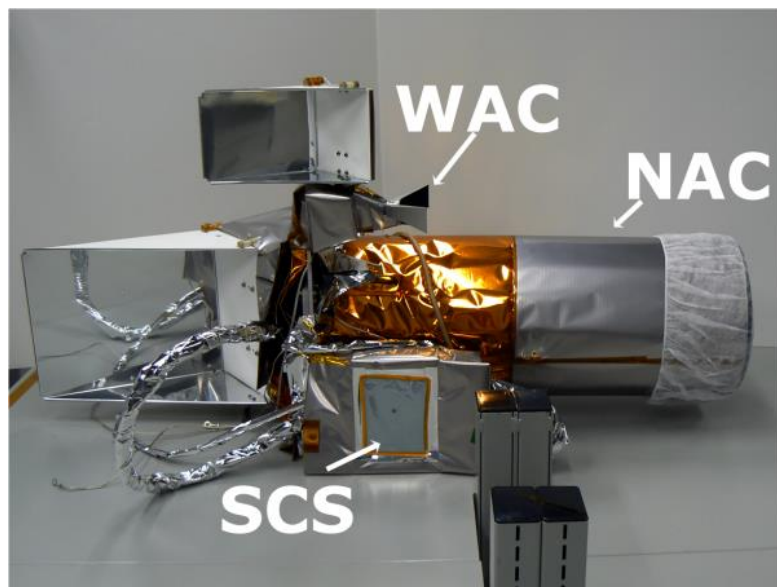


*Figure 4.2: LROC instruments with their position indicated by the white arrow and acronyms. Credit: <http://lroc.sese.asu.edu>.*

component (Wide Angle Camera) with a 100 meter/pixel visible and 400 meter/pixel resolution UV (Ultra-Violet) and a Sequence Compressor System (SCS), which provides a single command and data interface between the LROC and the LRO spacecraft data system.

Principally LROC was designed to measure the small-scale feature for potential lunar landing site and to acquire multi-temporal images of the poles to characterize the polar illumination environment (Chin, Brylow, et al. 2007). To date, the LROC mission produced a high-value dataset which includes: a meter-scale imaging of regions of permanent or near-permanent illumination, a multiple co-registered observations of portions of potential landing sites and elsewhere for derivation of high-resolution topography through stereogrammetric and photometric stereo analyses and a global 100-m/pixel base map with incidence angles (60–80°) useful for morphologic interpretations which have been used in this (Barker, et al. 2016). Each month, the WAC instrument provides a complete coverage of the Moon and these images were mosaicked to create a global map under different lighting conditions (Speyerer, et al. 2011). For this thesis have been used images directly downloaded from LROC official website named WAC\_GLOBAL\_E300N3150\_100M.TIF with a resolution of 100 meter/pixel have been used.

All the data are available on the official site of LROC:

[wms.lroc.asu.edu/lroc/view\\_rdr/WAC\\_GLOBAL](http://wms.lroc.asu.edu/lroc/view_rdr/WAC_GLOBAL).

#### 4.1.2 Lunar Orbiter Laser Altimeter (LOLA)

LOLA objectives can be reassumed in the following (Chin, Brylow, et al. 2007):

- Obtain global geodetic lunar topography.
- Characterize lunar polar region illumination.
- Collect images of permanently shadowed regions.
- Contribute to the assessment of meter-scale features to facilitate landing-site selection.
- Identify surface polar ice if present.

LOLA (*Figure 4.3*) is made its measurements through a single laser pulse propagated from a single source. Then, the laser beam is divided into five beams that measures the precise distance to the lunar surface at 5 spots simultaneously (*Figure 4.4; A-B*). Each spot has a diameter of 5 meter, and the five spots formed a cross pattern of 25 meters (*Figure 4.4*).

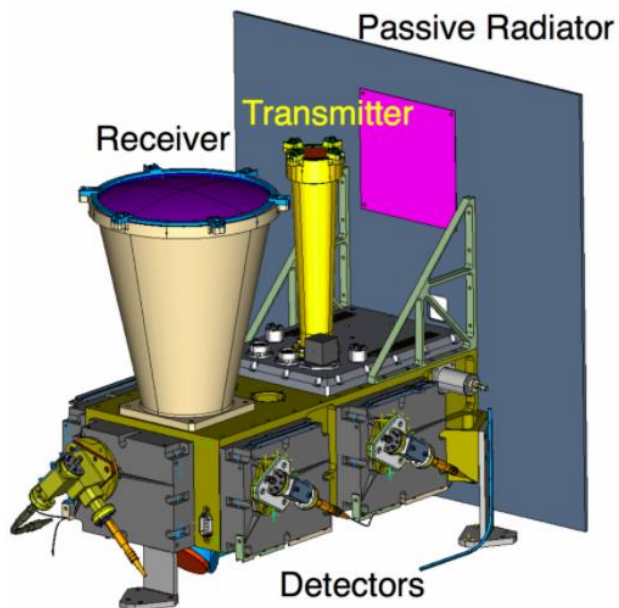


*Figure 4.3: LOLA instruments design. Credit: <https://lola.gsfc.nasa.gov/>*

In addition, each 5-meter spot provides a measure of the surface roughness to ~30 cm within the (flat) spot, derived from the spreading of the laser pulse. LOLA also measured the relative surface reflectance within each 5-m spot, in order to detect highly reflected material on the (Chin, Brylow, et al. 2007).

For this thesis it has been used SLDEM2015, which is a global lunar DEM deriving from the combination of Lunar Orbiter Laser Altimeter data (LOLA) and Selenological and Engineering Explorer (SELENE or Kaguya) data (Melis, et al. 2019), with a resolution of 60 meter/pixel and a vertical accuracy of 3-4 m; downloaded from the official website [https://pds-geosciences.wustl.edu/lro/lro-l-lola-3-rdr-v1/lrolol\\_1xxx/data/slDEM2015/](https://pds-geosciences.wustl.edu/lro/lro-l-lola-3-rdr-v1/lrolol_1xxx/data/slDEM2015/), named each one with the coordinates and the georeferenced quadrant (*Figure 4.5*):

- SLDEM2015\_512\_30N\_60N\_315\_360
- SLDEM2015\_512\_30N\_60N\_270\_315
- SLDEM2015\_512\_00N\_30N\_270\_315
- SLDEM2015\_512\_00N\_30N\_315\_360

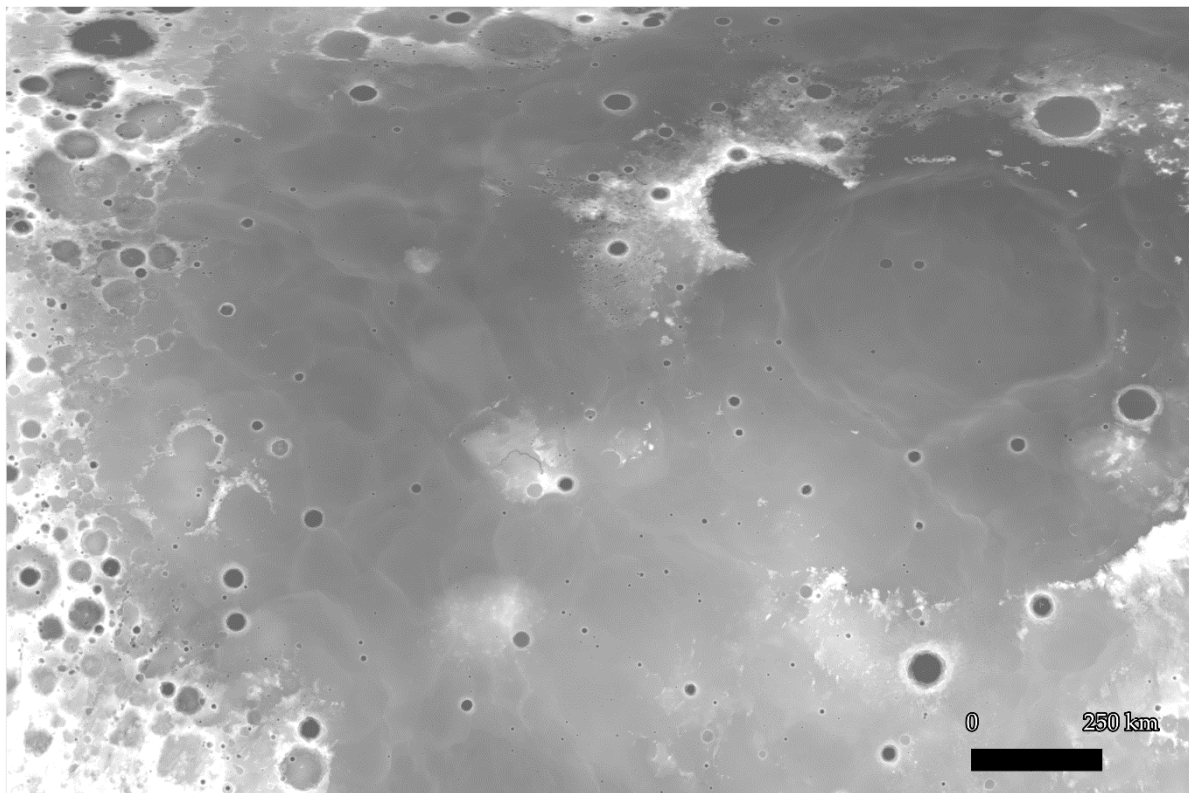


*Figure 4.3: Union of the four SLDEM2015. Credit: LOLA NASA*

#### 4.1.3 Chang'E2 DOM

Chang'E-2 raster images were used in the early phases on the Moon Mapping Project. The available images covered the area called *Sinus Iridium*, in the northern portion of *Mare Imbrium*. The digital orthophoto maps (DOM) of Chang'E-2 have a resolution of 7 meters/pixel and of great help to better analyse the small scale morpho-structures in the area (Figure 4.6). As reported in the “sixth workshop of the Moon Mapping project”, held in Guiyang (China) in 2017, thanks to the high resolution of the images, it was possible to revise the previous classification, mapping additional 72 generic structures in the area. However, the availability of Chang'E-2 DOM images only in such small area was considered too poor to be included in the thesis for two reasons: 1) in light of a more accurate mapping dedicated exclusively to the search for sinuous rilles, in the strict sense of the term, the area of Sinus Iridium does not present a particular abundance of such structures; 2) the DOM images made available covering an area of only  $10^5 \text{ km}^2$ , so that an in-depth analysis of sinuous rilles would have been little appreciable. However, since the DOM images spatial have a spatial resolution exceeding the

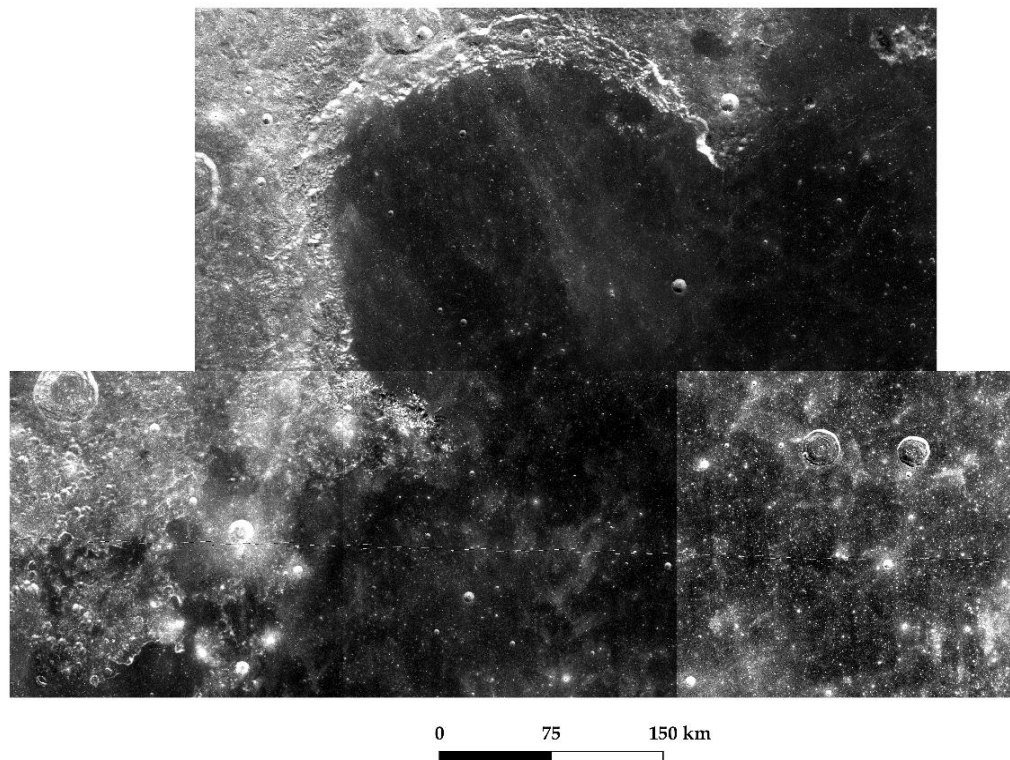


Figure 4.4: Chang'E-2 DOM image of Sinus Iridium area. Credit: CE2TMap2015

LROC's one, their use for future studies of the lunar surface and particularly of sinuous rille is worth to be considered.

## 4.2 Detection and classification criteria

In this paragraph it will be described the mapping methods used for this thesis. A feature on the lunar faces generally changes local topography and radiometric properties of the area, leaving discernible morphometric (Pike 1988) and radiometric (Guzzetti, Mondini, et al. 2012) signatures (i.e., changes in the form, shape, position, or appearance of a topographic surface) that can be detected and interpreted. A work of research, identification, and mapping of sinuous rilles has been conducted mainly based on the subjective interpretation of the morphological features of high-resolution images.

Sinuous rilles, as reported in § 3.1.4, are the remains of channels formed by lava that erupted in effusive, high volume volcanic events (Hurwitz, Head e Wilson 2012). These features are characterized by a flat bottom, steep, long and continue banks and generally associated with a source vent from which they originate. (Komatsu e Hargitai 2014). They can exhibit a certain degree of sinuousness, as for the terrestrial rivers, even if some of them have a straight course. Consequently, despite their peculiar and well recognizable shape on the lunar surface, it is not always easy to identify and distinct them from other similar morpho-structures, such as tectonic structures (see § 3.2). The combination of some morphological signatures allows the recognition of the rilles in the study area. All the sinuous rilles were mapped manually, starting from any point in the contours of the rilles. The polygon follows the outermost edge of the sinuous rilles, where the banks cut the surrounding basaltic layer. In the final parts of the rilles, where the channels of the rilles tended to slowly disappear, the DEM was used, in same case, to define the flow channel. However, for those which do not have an outraged end, it was preferred to close the polygon in a linear way due to the impossibility to continue tracing the flow channel. In two cases, the presence of a sinuous rille within another has been detected. During the mapping work they have been considered as two separate rilles because evidently, they were produced by two different eruptive processes in time scale.

The method of classification used is based on the following criteria:

- The prevalent presence of sinuous rilles on *maria* region and around or within impact craters.
- The presence of a potential source vents on the initial part of the rilles, not always observed.
- The observation of the sunlight illumination angle to detect the features.
- The common behaviour of sinuous rilles to bypass topographic obstacles, such as reliefs, pre-existing craters, and follow the contours of the highland's *terrae*.
- The differences in width from the starting point of the rilles, often characterized by the presence of a source vent, and the final point, which is observed to be shallower and smoother than the initial part of the rilles.
- A certain grade of sinuosity has been observed for well-developed rilles, intended as features having an extension of more than 20-30 km, characterized by a type of meandering channel reminiscent of terrestrial river channels.

The criteria listed above will be explained in detail below. The sinuous rilles are concentrated mostly on *maria* and in particular in the central eastern and southern area of the *Oceanus Procellarum*, in the northern area of the *Mare Insularum* and in the northern area of the *Sinus Iridium* bordering the *terrae* (*Figure 4.7*).

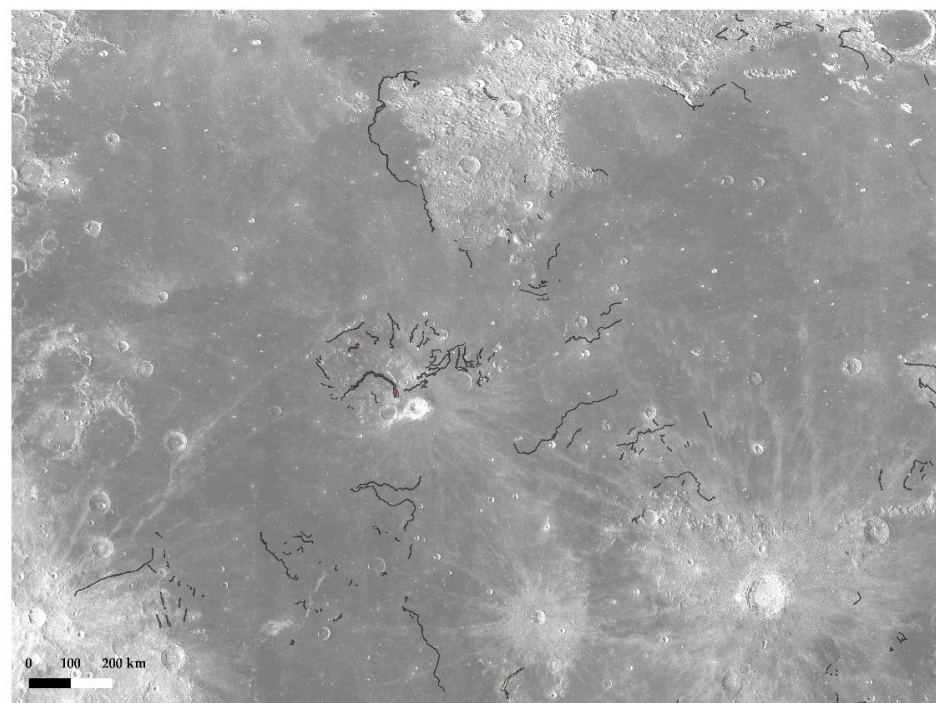


**Figure 4.5:** The mapped sinuous rilles concentrated in the central eastern and southern area of the *Oceanus Procellarum*, in the north of the *Mare Insularum* and in the north of the *Sinus Iridium*, scale bar 200 km.

Sinuous rilles, being created by a flow of lava in the basaltic substrate of the maria, generally present a source vent, characterized by an initial lobed shape wider than the body of the rilles (*Figure 4.8*). This source vent can also originate from a weaker point of the lunar surface, a condition found around and inside some impact craters. For those, sinuous rilles are detected around impact craters (*Figure 4.9*).

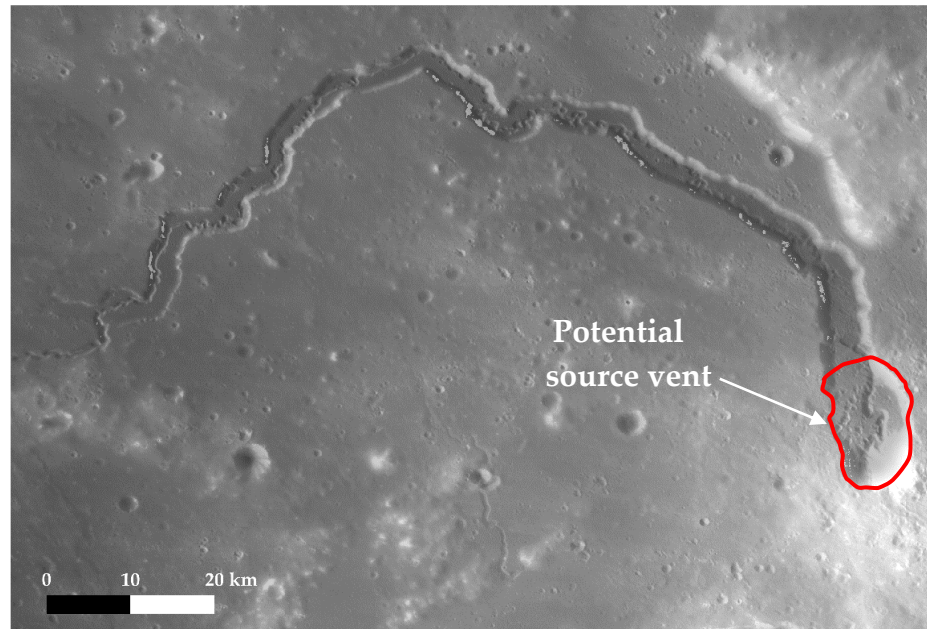


*Figure 4.7:* Vallis Schröteri rilles, it is possible observed the source vent on the right, highlighted in red.

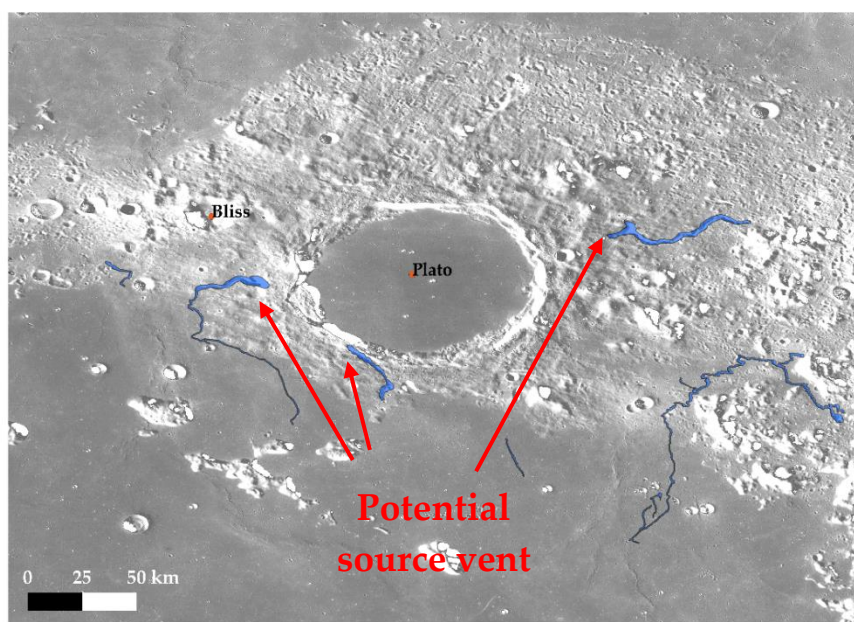


*Figure 4.6:* sinuous rilles mapped around Plato crater in the north-eastern area of Sinus Iridium. The rilles show a potential source vent that starts from the outer rim of the crater.

The identification and observation of the lunar surface and consequently also the features, can change depending on the angle of illumination of the Sun. When the Sun is high (incidence angle  $\sim 68^\circ$  up to  $90^\circ$ ) no useful shadows are observed, while when the low Sun image (incidence angle  $\sim 8^\circ$ ) has marked shadows highlighting the surface texture and features. The angle of illumination is especially important when viewing images. In this case it has been of great help in finding the exact morphology of the rilles, allowing to distinguish the depressions from the reliefs, the steep banks, and the terminal parts of the rilles. The shadows projected, in fact, help in the interpretation by showing the shapes of the rilles as shown in *Figure 4.10*. Thanks to this property of satellite images it is possible not only to distinguish rilles but all other features on the lunar surface.

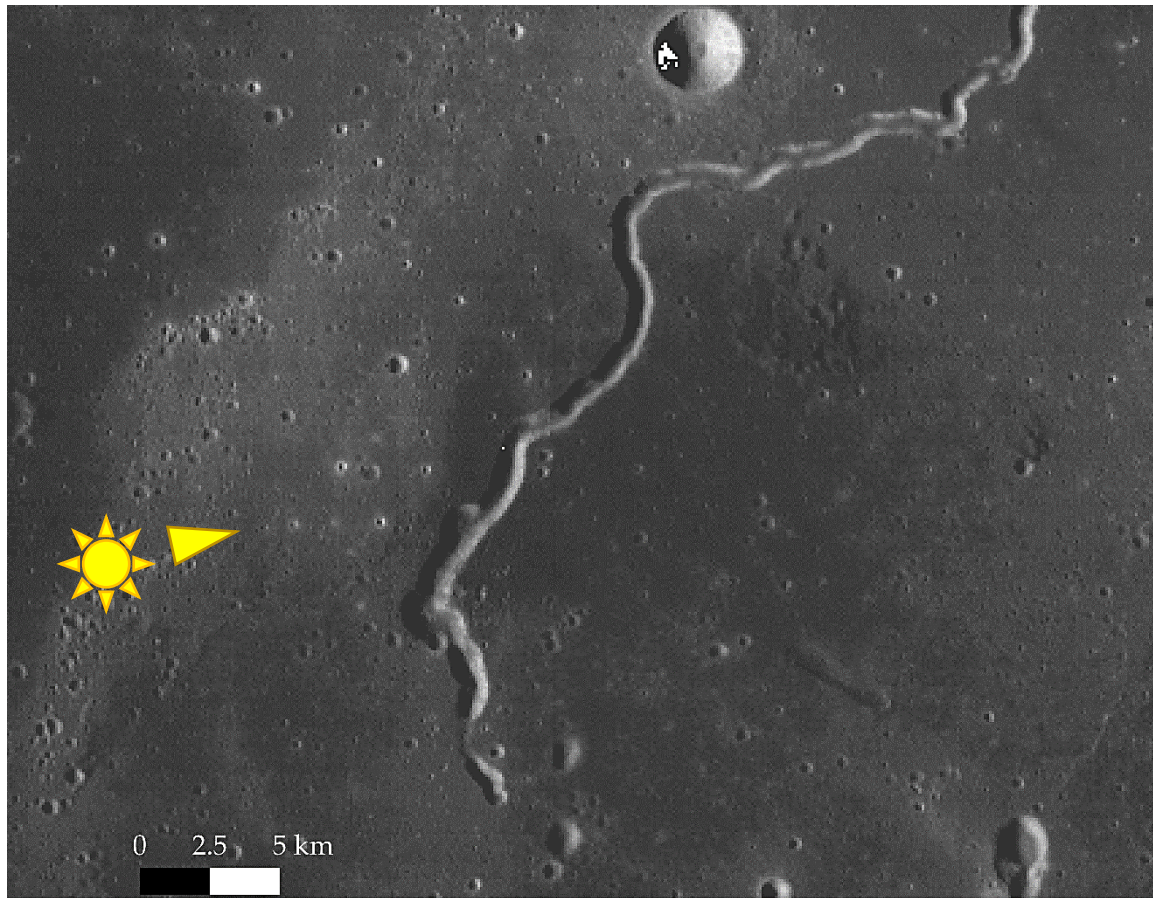


*Figure 4.8: particular of Rima Marius in the south-eastern of Oceanus Procellarum. The grey colour shade highlights the two banks of the sinuous rilles. Sun light illumination is marked with the Sun symbol on the left.*

One of the main characteristics is that sinuous rilles tend not to cut the surrounding topography, preferring flow directions with less energy, bypassing topographical obstacles (*Figure 4.11*). For this reason, in chapter 3 (§ 3.1 and 3.2) a distinction has been made to identify volcanic and tectonic structures; the latter, although they partially recall the characteristics of sinuous rilles, have been excluded from the mapping work.

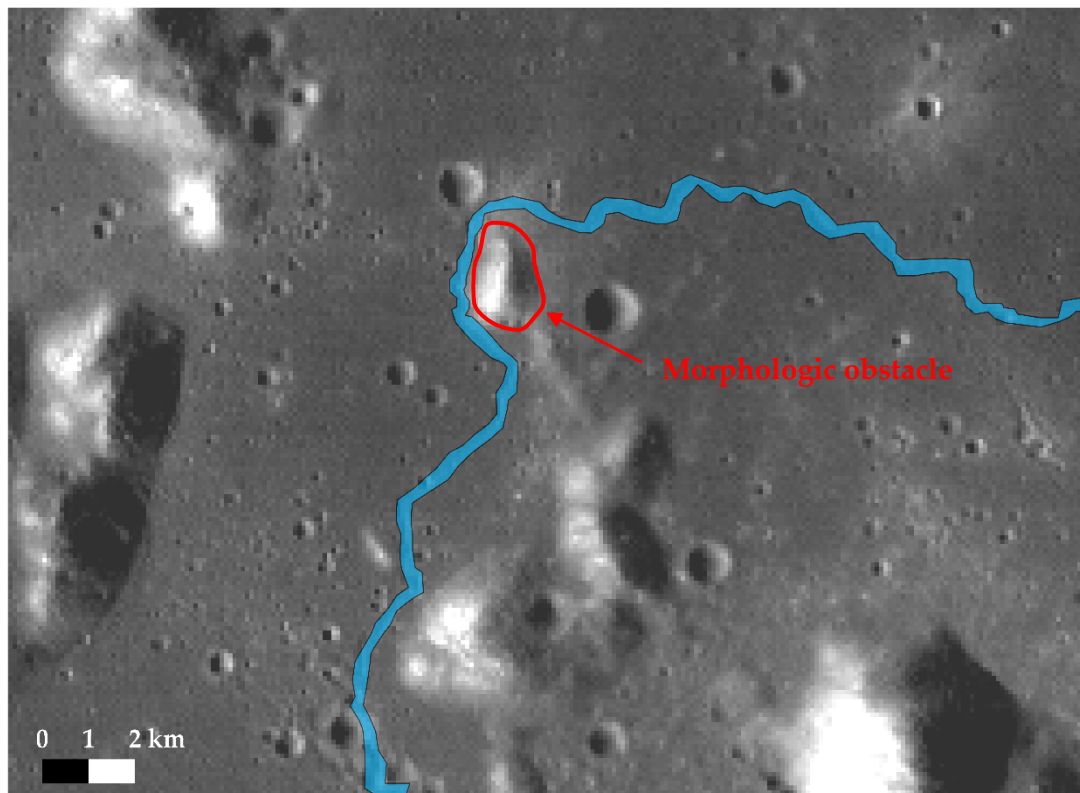


*Figure 4.9: detail of Rima Euler in the eastern area of Oceanus Procellarum. It appears clear the trend of the rille to avoid topographic obstacle, in this case a relief of Mons Vinogradov. The obstacle bypassed by the rilles in light blue is highlighted in red.*

In the majority of sinuous rilles observed, the flow of lava that has originated from the potential source vent, seems to dissolve, or otherwise decrease in intensity as it gradually moves away from the initial source. The flow result, as predictable, more abundant in the initial phases of rilles formations, and then exhausted in the final zones of the rilles (*Figure 4.12 A-B*). When this behaviour is not observed, it has been hypothesized that the melting of the basaltic maria has covered the final part of the rilles.

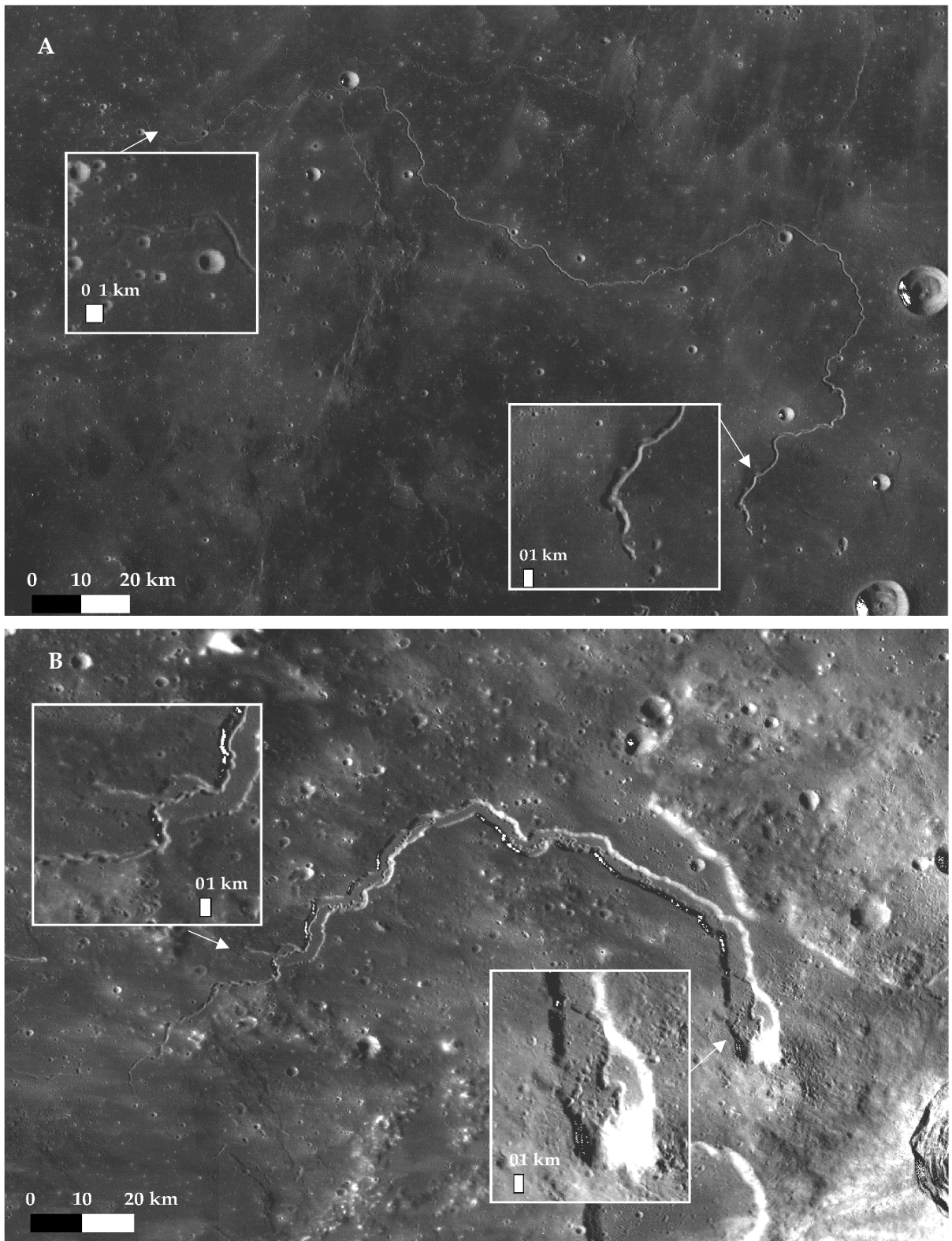


**Figure 4.10:** A) Rima Marius in the southern of Aristarchus plateau. In the white squares it is highlight the difference of the starting point of the rilles (right square), characterized by marker banks and deeper channel than the final part (left square). B) Vallis Schröteri rilles with the starting and final parts highlighted in the white square. Credit: LROC-WAC NASA.

Another character that distinguishes sinuous rilles, even if not all of them, is the degree of sinuosity that they can present, similar to terrestrial meandering rivers (*Figure 4.13*). Although not all the mapped rilles have this characteristic, many of them have an intriguing pattern, also presenting minor branches, centre bars. The sinuosity is a characteristic of the more complex rilles that extend for hundreds of kilometres in length; other rilles, instead, have a straighter or a far lower degree of sinuosity if compared to the complex rilles

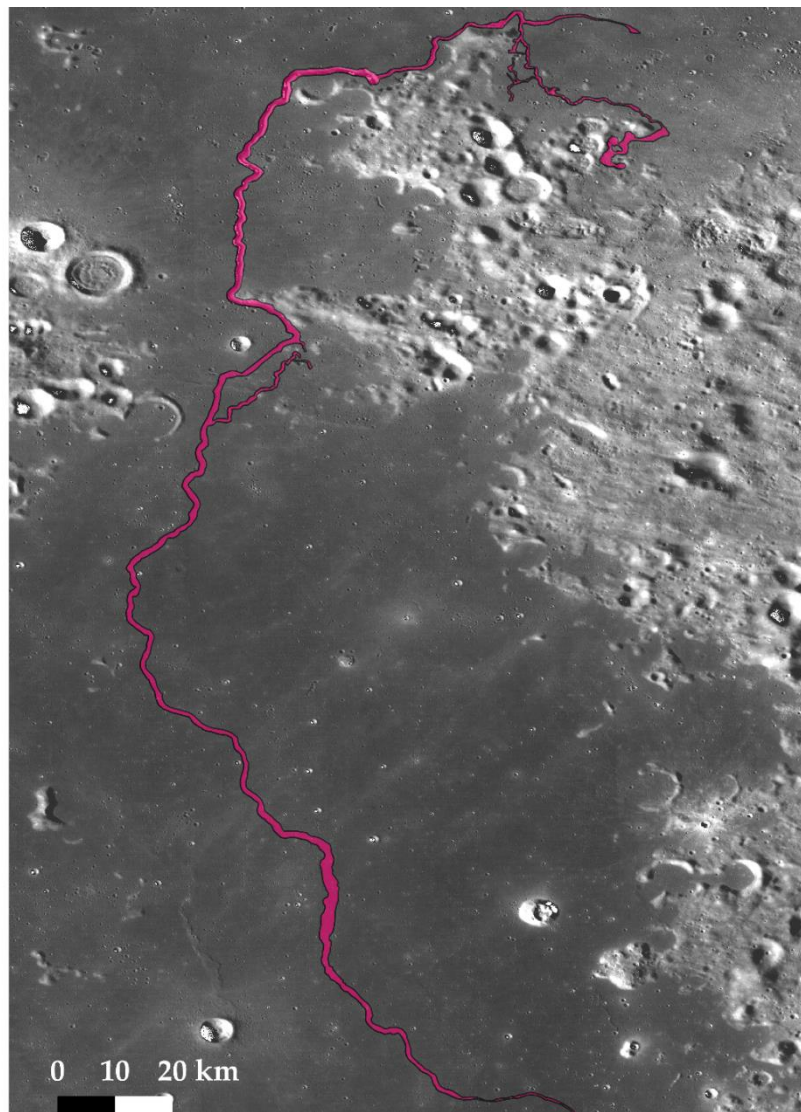


*Figure 4.11:* Rima Sharp in the northern area of Oceanus Procellarum. In the initial and middle side of the rilles is evident the branched pattern, probably due to some topographic obstacle or secondary eruptions. Credit: LROC-WAC NASA

The work of this thesis is based on the classification methods adopted previously in literature by Hurwitz et al. (2013) in which 194 sinuous rilles have been mapped across the entire lunar surface. Here, 210 sinuous rilles were mapped in the single quadrant area between 270°-360° east longitude and 0°-60° north latitude. The availability of high-resolution images allowed detecting and mapping a higher number of sinuous rilles in only 12.5% of the Hurwitz et al. area. The open source QGIS software (version 3.10.8, Coruña) was used to load, overlay, and process images. This software offers a wide range of applications (*plugins*), which have been especially useful in the processing phases of the work. The first part of the work concerned the mapping and collection of the data. The reference system (SR) used is the Moon2000, created and officially adopted by International Astronomical Union (IAU), which corresponds to an ellipsoid with a radius of 1.737.4 km. The same reference system was also assigned to the LOLA DEMs and to the polygonal shapefile created for the mapped sinuous rilles. Once the identification and mapping process has been completed, the available data has been analysed as described in the following chapter 5.

# Chapter 5- Analysis of morphometric parameters

In this thesis, the acquisition of the parameters of sinuous rilles is an important part of the whole work process and represents the last stage of the study. A detailed analysis of morphometric parameters has been conducted in order to characterize the sinuous rilles mapped. Parameters' measures are affected by an error estimate around 10%, hypothesized due to the direct and subjective mapping of the sinuous rilles and the quality of the data. The error range are reported in all the graphs in this chapter. A description of morphometric parameters acquired is described in the following.

## 5.1 Measures of morphometric parameters

The sinuous rilles have been characterized by the following parameters: 1) *Area Groups*; 2. *Width*; 3) *Length*; 4) *Depth*; 5) *Sinuosity index (SI)* and 6) *Slope*.

As mentioned in § 4.2, the 210 mapped sinuous rilles have been classified into 38 groups, each group named according to the feature (crater, volcanic complex and *rimae*) they belong to (*Figure 5.1*).

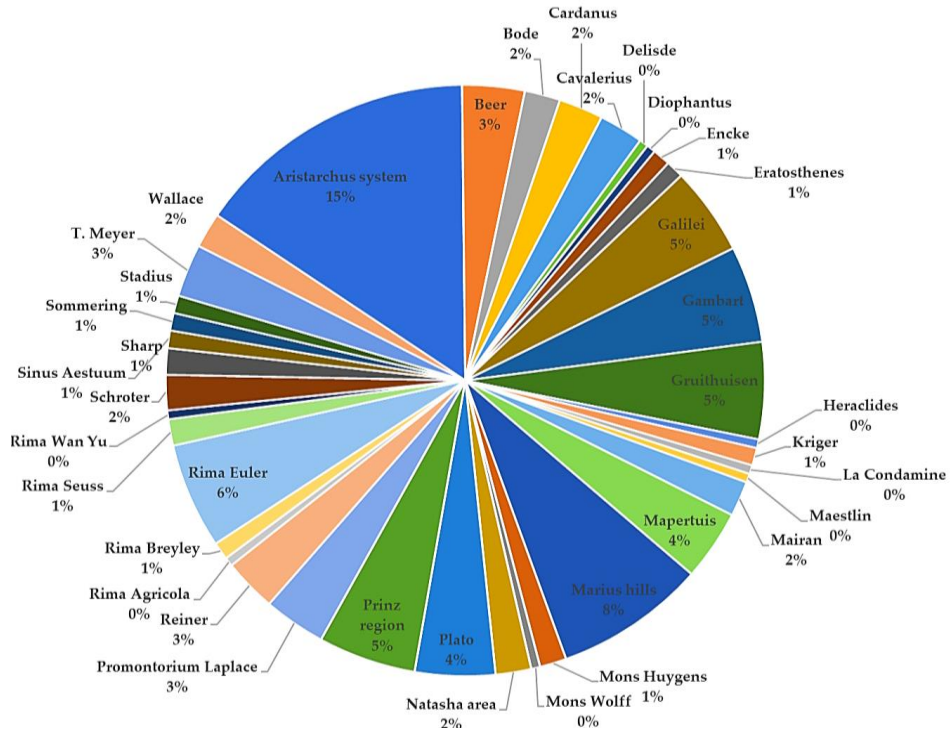


Figure 5.1: Sinuous rilles area groups.

Preferential flow direction, distance between the rilles and radial arrangement in proximity to the general feature have been used to assign the rilles to each group. The following criteria have been adopted as distinction elements: preferential flow direction, distance between the rilles and radial arrangement in proximity to the craters or volcanic system.

The *width* parameter (*Figure 5.2*) is defined as the average width of the polygon superimposed on the sinuous rille. The measurement was taken between the outer edges of the two rilles' sides and was obtained using the QGIS field calculator function according to the following formula (*Equation 5.1*):

$$\text{width (km)} = \frac{\text{area (km}^2\text{)}}{\text{length (km)}} \quad (5.1)$$

The value obtained is an average value referring to the geometry of each element, compared to a measurement of the entire geometry. The data analysis showed an average value of about 350 meters.

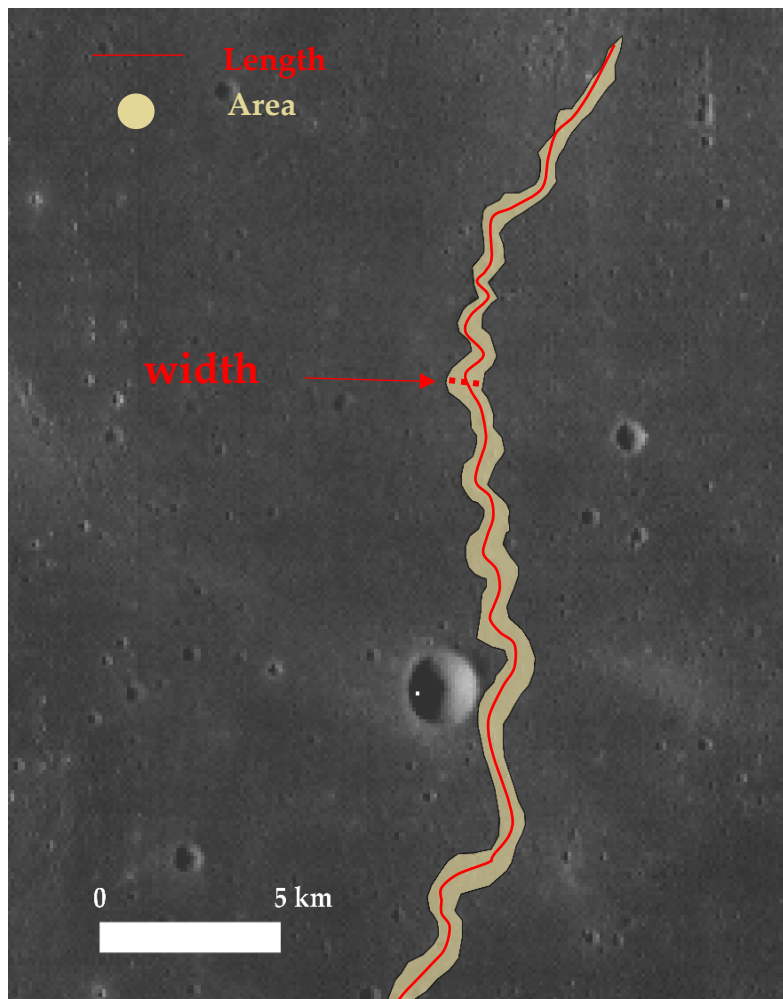


*Figure 5.2:* graphic description of. The red dot lines represent the width parameter.

The *length* parameter of the sinuous rilles is defined as the length of the central channel of the rilles, taking as reference the lateral bank tracks (*Figure 5.3*). Two methods have been used to estimate the length of the sinuous rilles. The first method gives an approximation of the length parameter and uses the field calculator QGIS function (*Equation 5.2*). The formula associates the mean length of the feature to the semi-perimeter of the rille.

$$\text{Length (km)} = \frac{\text{Perimeter (km)}}{2} \quad (5.2)$$

The second method for the length estimation (*Equation 5.3*) was expected to be more accurate than the first method. The two measurements are compared in *Figure 5.4*.

$$\text{Length\_2 (km)} = \frac{\text{Perimeter(km)} - 2 * \text{width(km)}}{2} \quad (5.3)$$

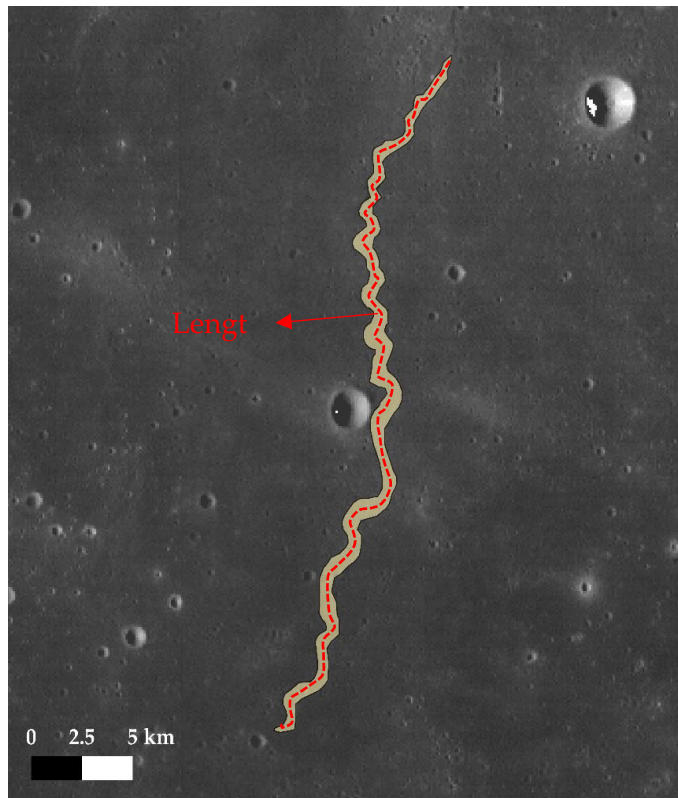


*Figure 5.3:* graphic explanation of length parameter applied to a geometry of a sinuous rilles. Red dotted line represents the central line and the length.

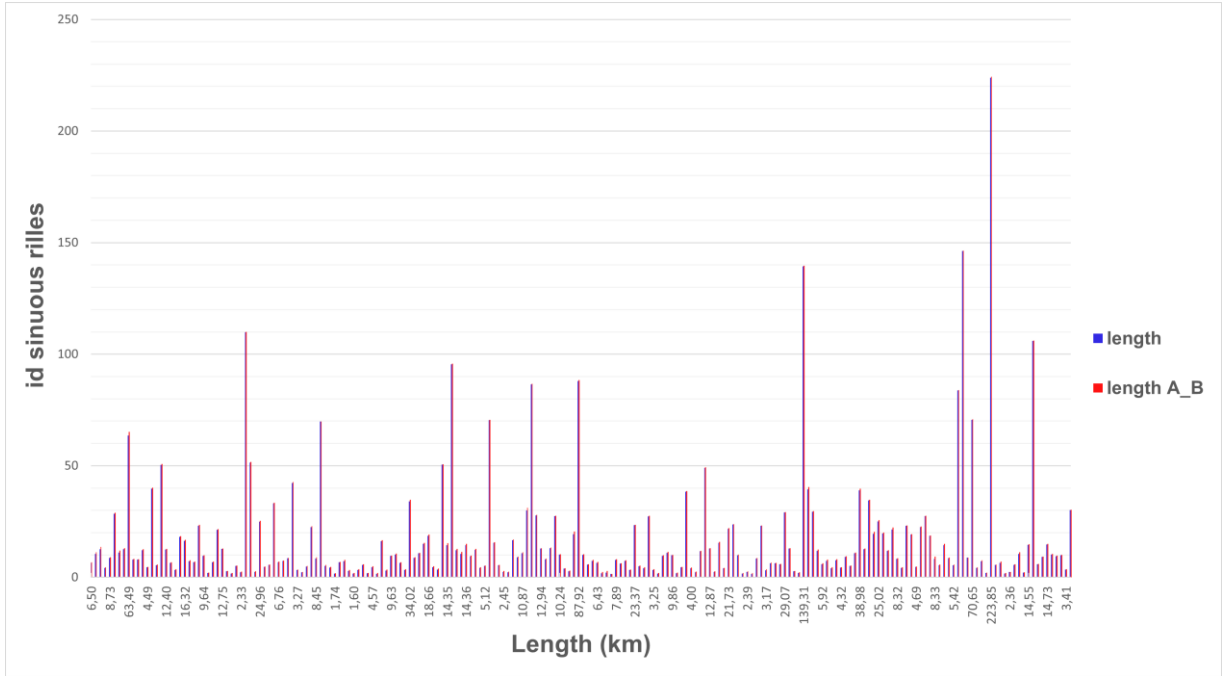


*Figure 5.4: graph of the two-length measured. The red and blue columns each other of at maximum of 15%.*

The relative error between the two measurements is defined as the ratio of the difference between length and lenght\_2 and the length\_2 expressed as a percentage (*Equation 5.4*).

$$\text{error (\%)} = \frac{\Delta S}{S} * 100 \quad (5.4)$$

As can be seen from the graph (*Figure 5.4*), the maximum error obtained between the length values is less than 20%.

In most cases, when the rilles have a more linear and less articulated structure, the relative error is about 5-7%, and increases until a maximum of 20% for the most complex rilles, for which drawing the contour may result to be less accurate. Overall, since the length of a rille is at least 10 times greater than its width, the first method was considered enough accurate and was adopted in the calculation of the rilles length.

The *depth* parameter (*Figure 5.4*) was derived directly from the LOLA DEMs. After completing the mapping process and obtaining a georeferenced *Moon200* shapefile, the DEM was cut out from the geometry images using the crop function for the QGIS mask. Then, using the QGIS zonal statistics command, the minimum and maximum quotes was obtained within each geometry. The *depth* parameter was derived directly from the LOLA DEMs (see § 4.1). After

completing the mapping process and obtaining a georeferenced *Moon2000* shapefile, the DEM was cut out from the geometry images using the crop function for the QGIS mask. Then, using the QGIS zonal statistics command, the minimum and maximum quotes were obtained for each geometric element. The procedure gives back a mean value of the depth including differences in height that may exist within the geometry itself, such as craters or other shapes that may change the real value of the minimum or maximum depth. However, there are only few cases in which the minimum and maximum altitude is modified by other features such as impact craters. The depth was obtained by measuring the altitude of a point outside the rille and calculating the difference with the lowest altitude automatically available from the DEM. The result is the average depth of the rille (in meters).

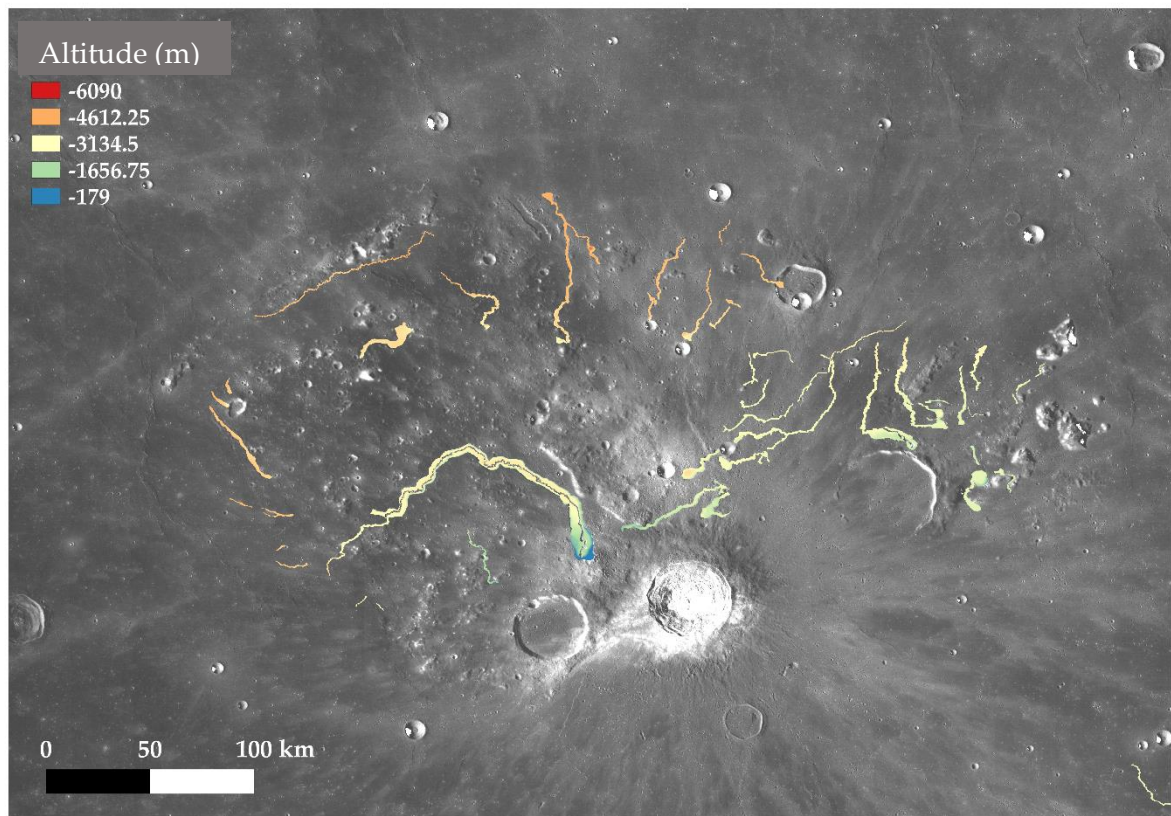


*Figure 5.4: Clipping of the DEM on the geometries of the sinuous rilles. The legend shows the values of the colour scale corresponding to the altitude in meters*

The *sinuosity index (SI)* is used to define the degree of meandering of a riverbed, in order to identify geomorphological river types (Horacio 2015). SI is the ratio between the effective

length of the channel and the shortest distance (straight line) between the beginning and the end of the sinuous rille (*Equation 5.5*), i.e. the starting point (A) and the final point (B) of the channel length (*Figure 5.5*). The actual length was derived using the methods described above, while the shortest path was directly measured and reported in the summary table for each polygon.

$$SI = \frac{\text{channel length}}{\text{length } A\_B} \quad (5.5)$$

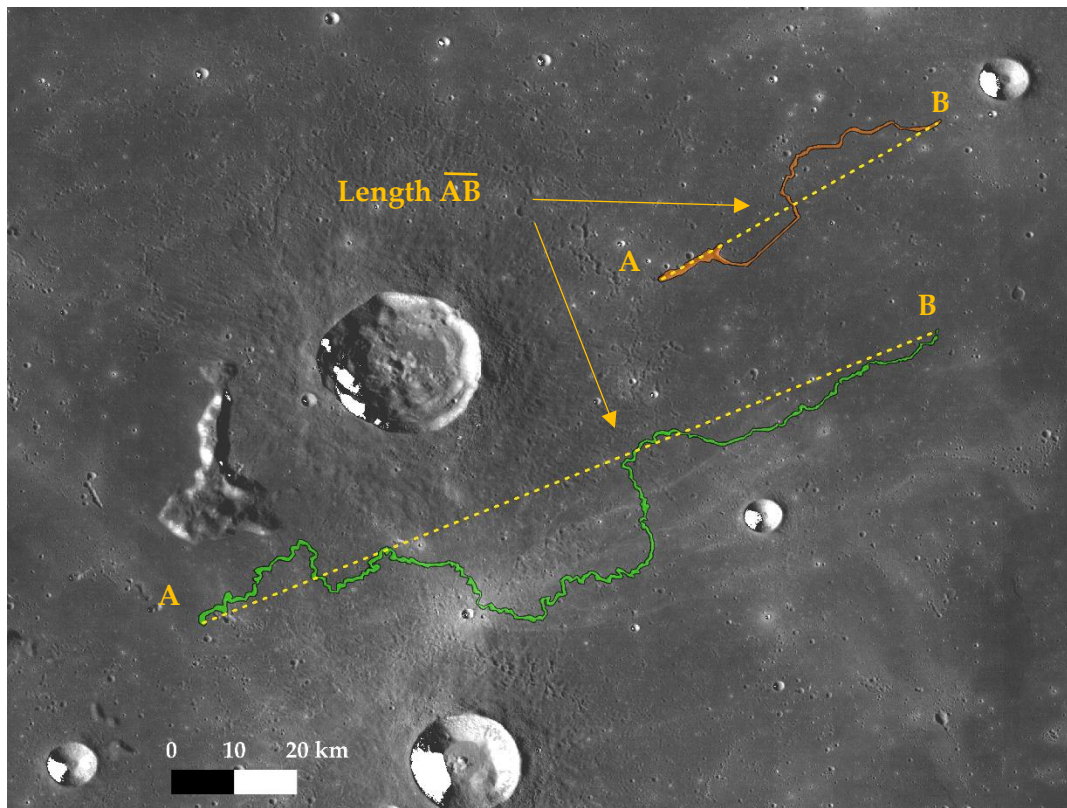


*Figure 5.5:* representation of the length  $\overline{AB}$  from the starting point of the rille (A) and the final point (B). Rilles in green and orange colours belong to the groups of Diophantus and Delisle.

The sinuosity index can be explained as the deviations from a path defined by the direction of maximum downslope (Mueller 2010). For terrestrial rivers SI ranges from a minimum value of 1 (straight coarse) to a maximum value of 5 (meandering). The range of values obtained from the measurement of the sinuosity of the lunar rilles is between 1.01 and 5 (Pike 1988, Hurwitz, Head e Heisinger 2013). Some values indeed exceeded the maximum terrestrial value of 5, but this is essentially due to both measurement errors, since the manual procedure has an

uncertainty of about 10%, and to the length of some rilles. Anomalous values of the sinuosity have been solved with the application of the measurement method used for long rivers on Earth. This method (Horacio 2015) consists in dividing the channel into two or more segments measuring the partial sinuosity index for each section and then calculating the mean value (*Figure 5.6*). This procedure led to an average SI, within the range of the expected values for those rilles with anomalously high SI values.

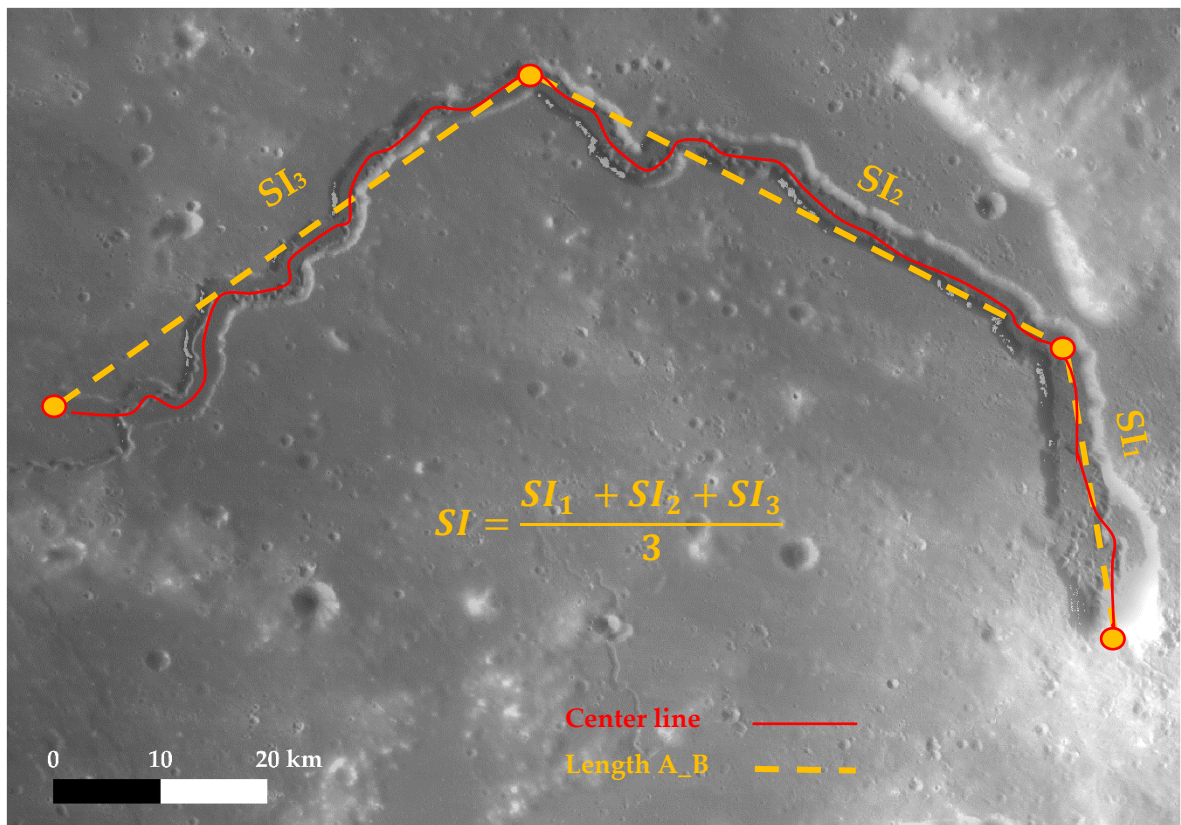


*Figure 5.6: example of the application of SI measure applied to Vallis Schröteri in Aristarchus System.*

The *slope* parameter is the altitude difference in degrees of the sinuous rilles. The slope is important to understand the direction of the flow and during the analysis process, to understand if there is a correlation with the sinuous rilles. Formula (*Equation 5.6*):

$$Slope = \frac{(quote_{min} - quote_{max})}{length} \quad (5.6)$$

The range detected for the mapped sinuous rilles corresponds to a minimum value of  $0.04^\circ$  and a maximum value of  $14^\circ$  to, with a mean value around  $1.59^\circ$ . The relatively low mean

value of slope is evidence of the fact that most of the rilles are in the quasi-flat basaltic plains of the *maria*. Higher values of the slope are typical of those rilles that are instead located either near the impact craters or near the *terrae*.

## 5.2 Statistical distribution of morphometric parameters

The morphometric parameters of the collected sinuous rilles, show how these features exhibit a great variety of shapes and morphologies, which vary in length, width, depth, sinuosity, and slope. The maximum, minimum and mean values are summarized in *Table 5.1*.

	Depth (m)	Length (km)	Width (km)	Slope (°)	Sinuosity Index
<b>Max</b>	370,05	223,85	1,65	14,39	1,02
<b>Min</b>	5,26	1,52	0,09	0,04	5,01
<b>Mean</b>	49,56	17,23	0,35	1,59	1,80

*Table 5.1: Maximum, minimum and mean values of the mapped sinuous rilles, corresponding to the mean morphometric parameters measured.*

The analysis of these parameters helped to answer the questions of the thesis objectives (see § 1.4).

The classification of rilles by area groups (*Figure 5.7*) has shown that most of them are concentrated in six main regions: Aristarchus system with 32 mapped rilles, Marius Hills with 17, Rima Euler with 12, followed by Gambart, Gruithuisen and Prinz region with 11 mapped rilles.

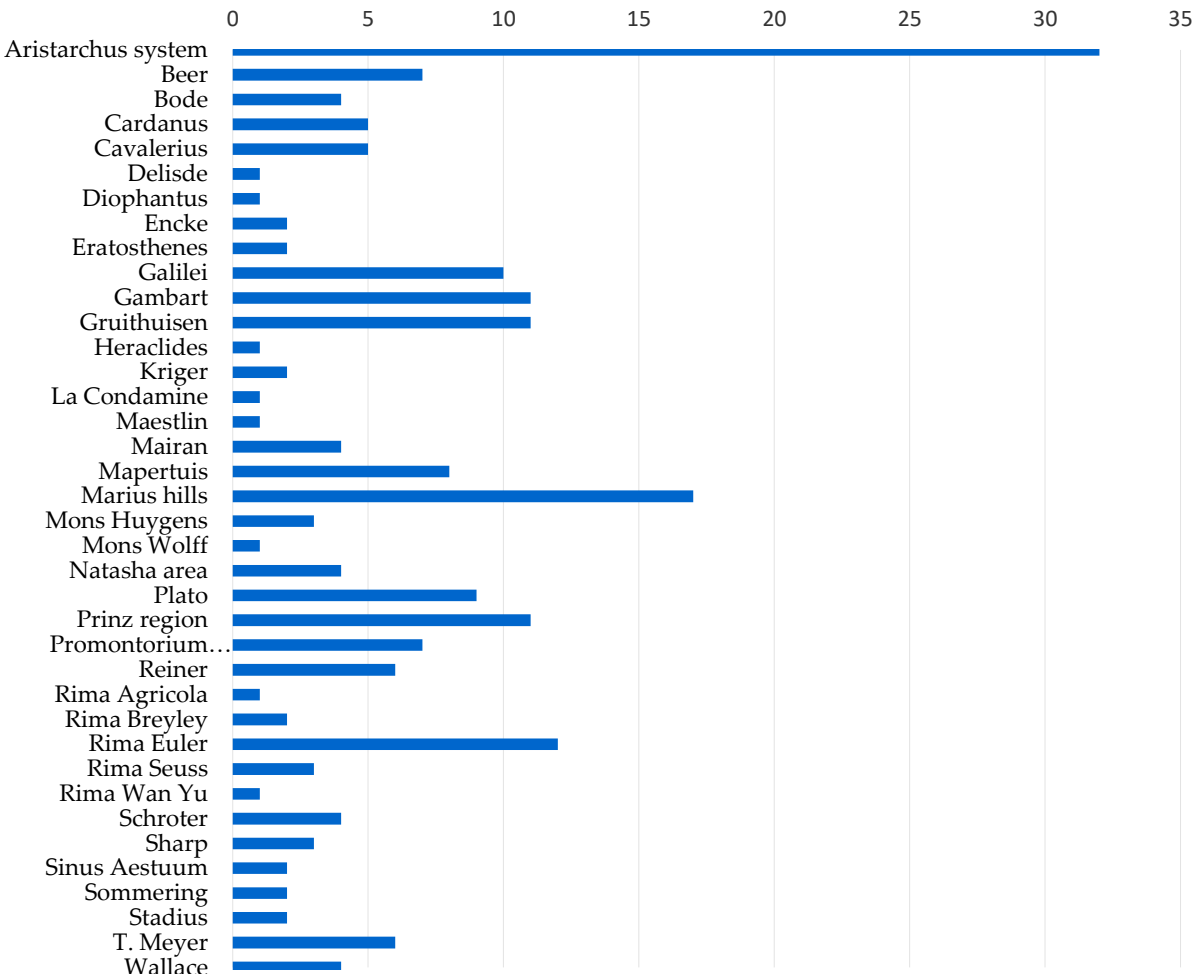
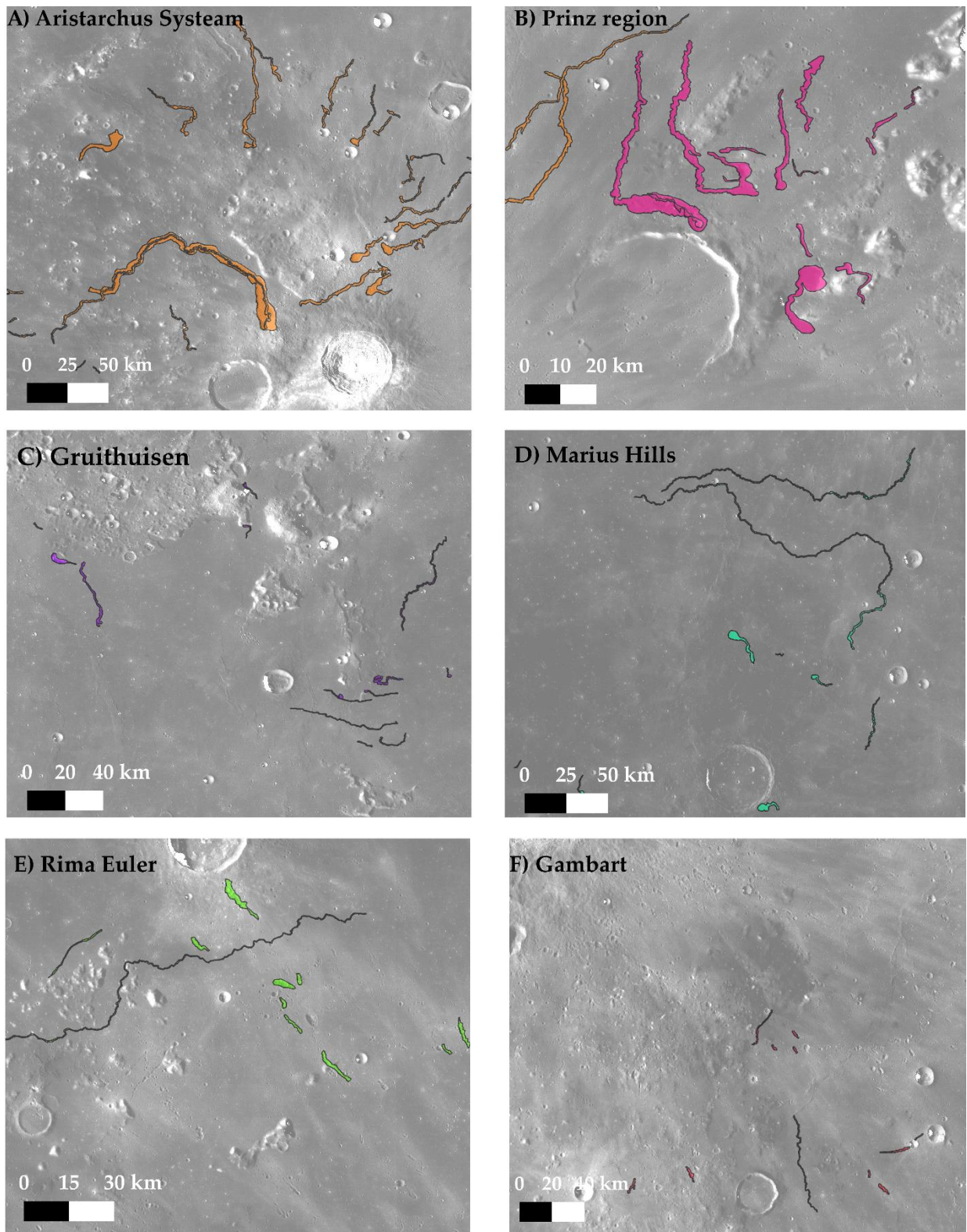


Figure 5.7: frequency of sinuous rilles grouped by area.

The rilles of these groups (Figure 5.8) have an average length ranging from about 7 km in Gambart area up to about 18 km in the Aristarchus system. Areas hosting the majority of rilles are particularly rich in volcanic features, such as Marius Hills and Aristarchus system, described in § 3.1.3. Most of the rilles in these areas, have a recurring shape with at least one rille longer than the others and well developed with sharp and steep banks and accentuated sinuosity. In Aristarchus system and Prinz region, the existence of one rille inside another one has been observed, suggesting, due to the overlapping principle, a multiple and complex eruptive event, which led to the formation of the peculiar morphology.



*Figure 5.8: the six main groups of sinuous rilles classified by area.*

The length parameter was very indicative in the search for a common trend or pattern for the characterization of sinuous rilles. In fact, a large variance is observed regarding the length distribution. The frequency distribution of the length shows (*Figure 5.9*) how the range varies between a minimum value of about 9-10 km up to about 250 km. The frequency density of the rilles lengths has been calculated by grouping the data in intervals of 10 km.

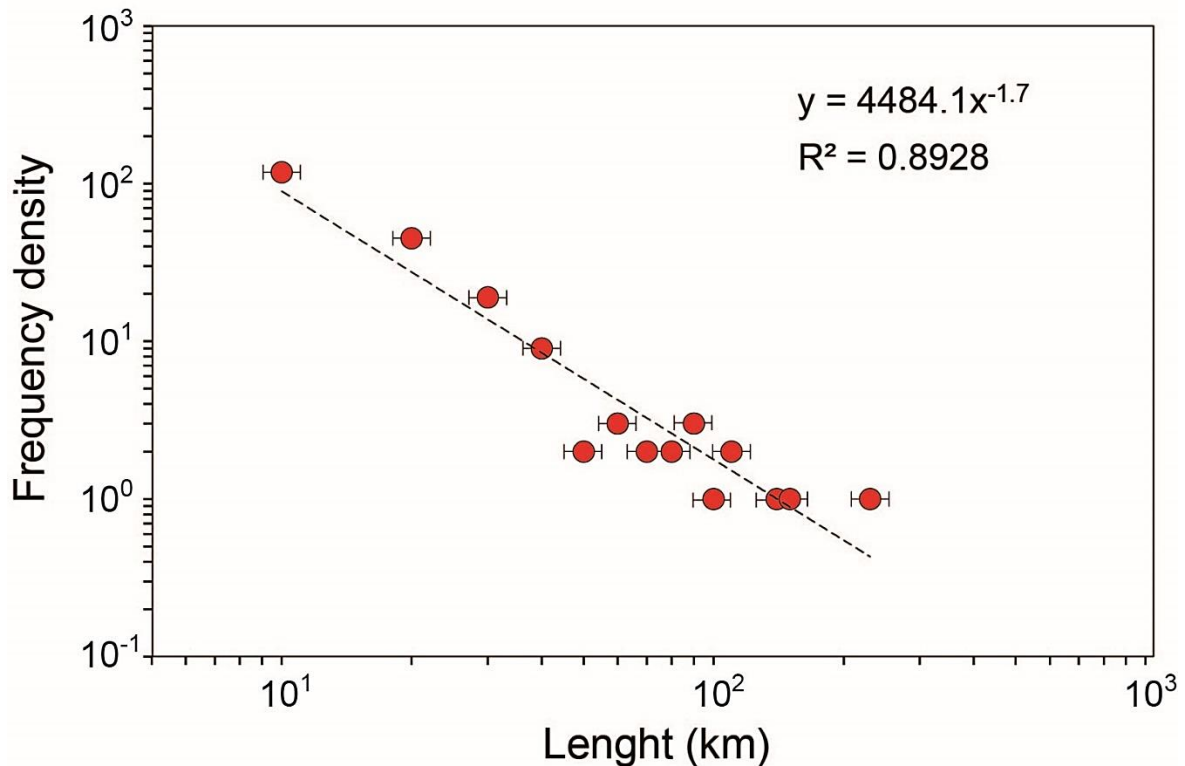


*Figure 5.9: frequency density of sinuous rilles lengths.*

The graph for the frequency distribution of lengths is shown in bi-logarithmic scale due to the range of values. The result shows that the frequency density decreases according to a power law with a linear correlation coefficient of  $R^2= 0.8928$ . Larger dispersion is observed for the frequency density of the longest rilles (Length > 40km). This behaviour may be due to the type of volcanic eruption that led to their formation. Long lasting events of particularly high intensity, characterized by large volumes of lava flows, likely origin sinuous rilles of long and complex sinuous rilles. Since few rilles, as shown in *Figure 5.9*, exhibit the longest lengths, this suggest that high-intensity lava eruption was exceedingly rare or at least not as frequent as those that gave rise to the majority of the rilles.

Another interesting results, concerned the frequency distribution of the slope parameter (*Figure 5.10*). The fit superimposed on the slope distribution shows that as slope increases, the number of rilles decreases. The average value is about  $1.6^\circ$  and this agrees with the prevalent presence of the rilles in the basaltic plains, which are characterized by low slope degree.

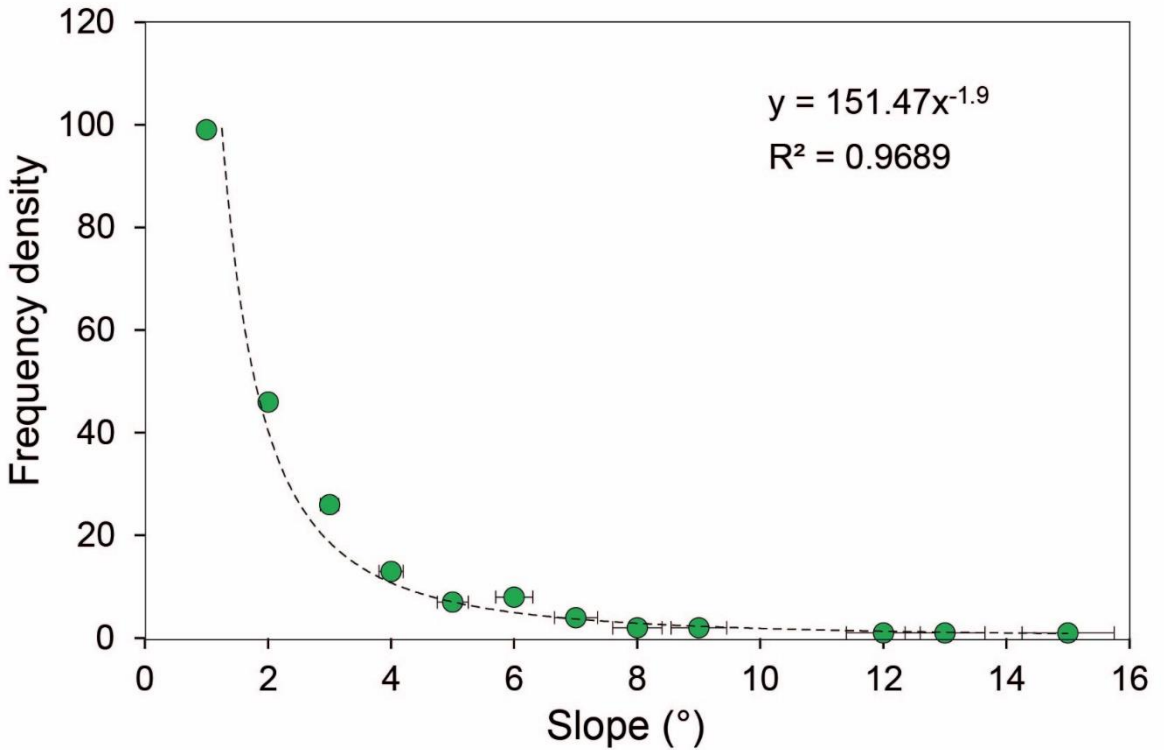


*Figure 5.10:* frequency density of the sinuous rilles slope distribution.

As shown in the graph, only positive slope values were detected, despite the negative values found by Hurwitz et al. (2013) and more recent by Podda et al. (2020). In both the two published works, a negative slope is found as a result the difference in altitude between the initial and the final parts of the rilles. The discrepancy with the findings of this thesis, could be explained with a different identification of the rille's source and direction. Negative slopes could only be interpreted as modification of the lunar surface occurred after the rille formation. These seems to be unlikely because it would have been caused by tectonic events that affecting the rille's area or by recent lava flow. In both cases, discernible signatures like tectonic structures cross-cutting the rilles or rilles partially covered by layers of lava, would have been

observed. The  $R^2$  value of the regression line results to be equal to 0.9689 and therefore it confirmed the behaviour that for gradients higher than about  $4^\circ$  the rilles tend to form rarely.

The frequency distribution of width parameter, shows on the graph in *Figure 5.11*, reveals a predominant variance between 100 and 1700 meters. The mode of the distribution is in the bin 200-400 m. Most of the rilles have a width varying 200 m and 700 m. Such a limited range of values might indicate a typical shape of the rilles and might suggest a common formation mechanism. Since the width of the rilles is not constant along their length, a more accurate sampling would be obtained with multiple measurement along the two banks. Nevertheless, for the purpose of this thesis the value estimated with the QGIS field calculator was considered sufficiently accurate.

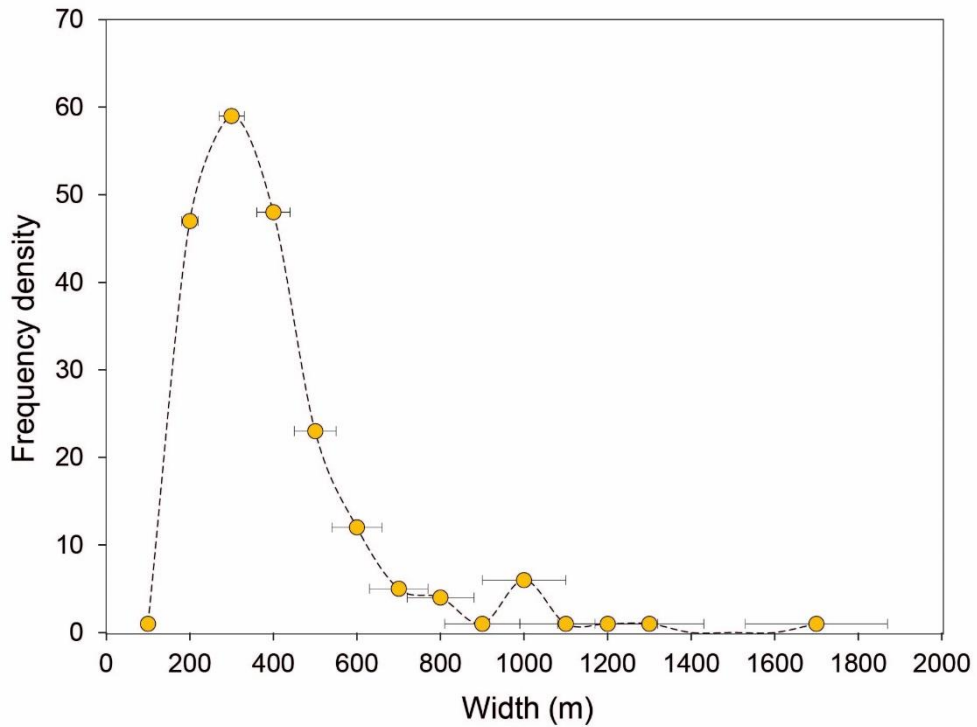


*Figure 5.11: frequency density of width parameters of the sinuous rilles.*

Further investigations were also made as for the width parameter, analysing the frequency distribution of the depth and of the sinuosity index, but they did not lead to noteworthy results.

As reported in Hurwitz et al. (2013) and Podda et al. (2020) a correlation between width and depth has been investigated here, searching for a relationship between these two parameters. However, once plotted the graph (*Figure 5.12*), there is no clear correlation between these two parameters. Most of the values are concentrated in the left part of the graph as outliers have shown in the bottom left of the graph. Two outliers are shown in the upper right part of the graph and may indicate an anomalous shape of the rilles or even misinterpretation of the features.

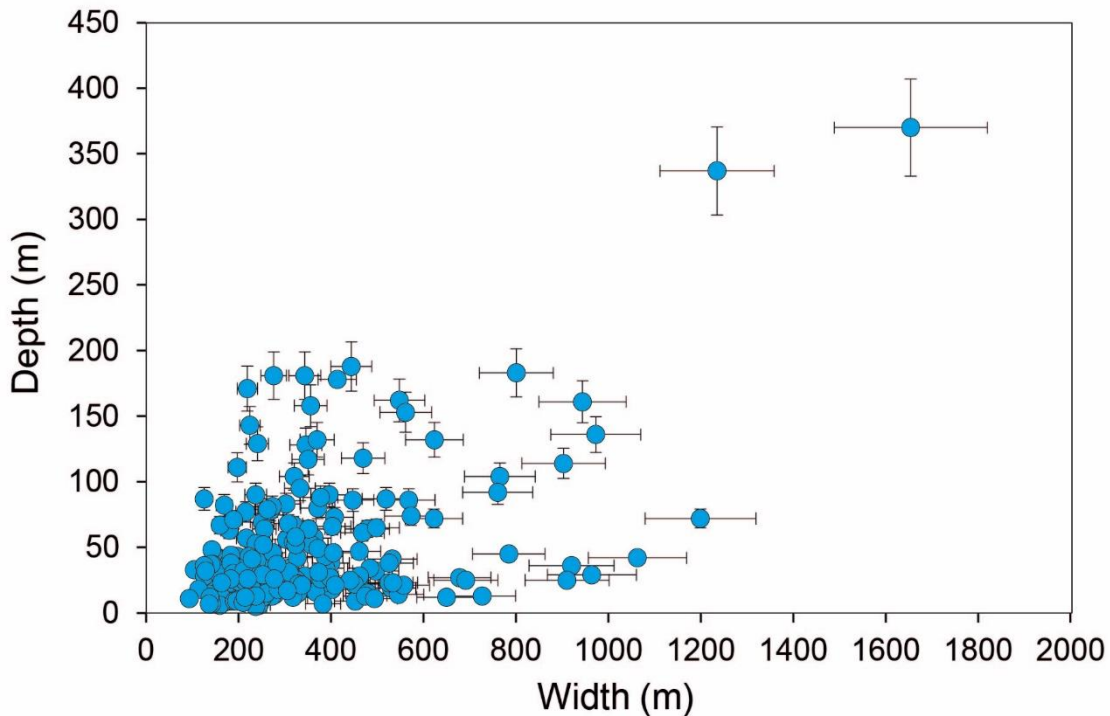


*Figure 5.32: width vs. depth parameters of sinuous rilles.*

The depth seems to be correct, having been directly taken from the LOLA DEMs data, while as far as the width is concerned, the calculation was done working on the shapefile of the sinuous rilles geometries. Since the width values are the most anomalous, the idea of resampling the geometries and taking further measurements of the parameters should be reconsidered.

The comparison with the findings of Hurwitz et al. (2013) (Figure 5.13 A) and Podda et al. (2020) (Figure 5.13 B), reveals a markedly difference in the distribution of the data, and in particular, they found a correlation between the rille's width and depth. A marked correlation

was not observed in this analysis. The linear correlation between the two parameters has values of  $R^2$  of 0.74 (*Figure 5.13 A*) and  $R^2$  of 0.81 (*Figure 5.13 B*), suggesting a strong efficiency by the lava flow to erode with the same efficiency both vertically and horizontally, suggesting a direct proportionality between the two parameters (Hurwitz, Head e Heisinger 2013, Podda, et al. 2020). Nevertheless, it is worth to remind that Hurwitz et al. (2013) collected 194 data across the entire surface and Podda et al. (2020) collected only 51, focusing on the second quadrant of the Moon. In this thesis, however, the number of data collected is larger (210) than the previous works and is concentrated in a single quadrant. It would be possible that the distribution obtained here differs from those of the previous works due to the amount of data used and due to the different sampling resolution. This work, indeed, significantly increases the number of collected features, while increasing the statistical significance of the results.

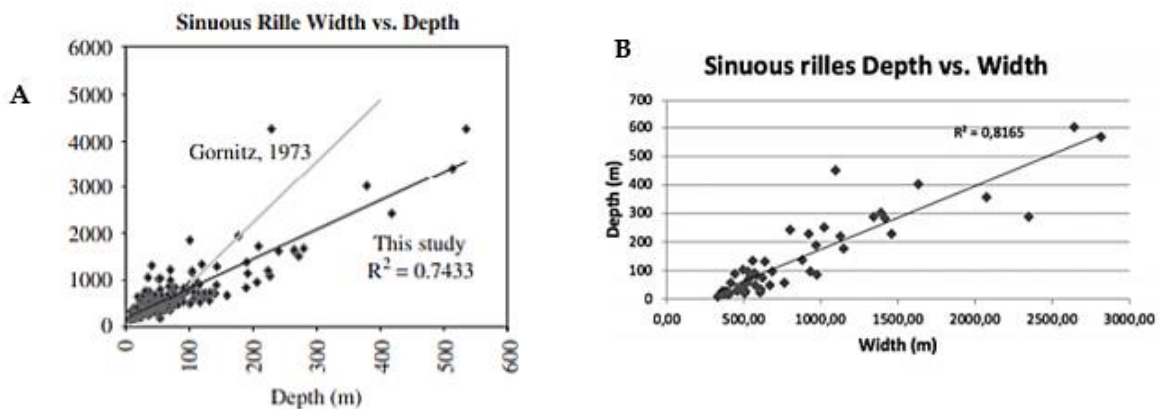


*Figure 5.43: A) graph of width and depth parameters from Hurwitz et al. (2013); B) graph of width and depth parameters from Podda et al. (2020).*

The graph of the sinuosity index as a function of the and slope value has been made (*Figure 5.14*). the graph shows that there is not an evident relationship between these two parameters but increasing the slope a general decrease of the sinuosity index has been observed, as shown with the red line on the graph. This is expected since higher the potential energy of the slope the higher is the kinetic energy of the lava flow and consequently the straighter is the path.

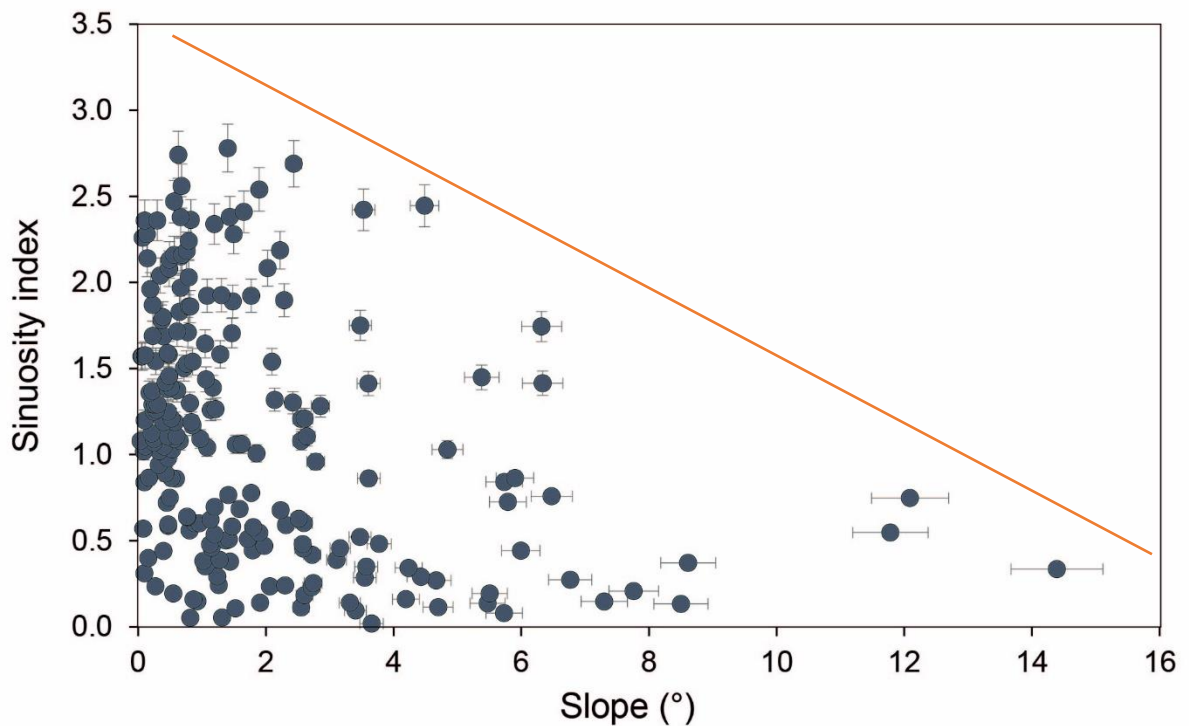


*Figure 5.54: sinuosity index vs. slope parameters of sinuous rilles.*

The sinuosity index tells us how much a channel changes its path with respect to a straight trajectory. As seen from the graph in *Figure 5.9* and *Figure 5.10*, the rilles with lengths greater than 100 km, tend to be a minority compared to other rilles with lower lengths; moreover, most of the rilles have an average slope  $<1\text{--}2^{\circ}$ . This leads us to say that the sinuosity of a rille might be depend on its mechanism of formation. As suggest by Hurwitz et al. (2013), two main mechanisms of sinuous rilles formation are possible: constructive processes and erosive processes, the second one been divided into mechanical and thermal erosion mechanism. Their study conducted, demonstrated that erosion processes have occurred in the initial stage of the rilles' formation for shallower slopes ( $<3.5^{\circ}$ ), making the rille's path almost straight (Hurwitz, Head e Wilson 2012, Hurwitz, Head e Heisinger 2013). Therefore, thermal erosion could be considered the principal formation mechanism for the most of sinuous rilles analysed in this work. The sinuosity, as shown in the graph in *Figure 5.14*, does not seem to be particularly related to the slope. It could be hypothesised that this parameter depends more other factors, such as lithology of the substrate and rheological behaviour of the lava flow (Hurwitz, Head e Heisinger 2013, Podda, et al. 2020).

# Conclusions

The analyses carried out have shown that sinuous rilles are complex structures with a great morphological variety and different interpretations. In the thesis, 210 sinuous rilles were mapped and analyzed according to their area groups and characterized by morphometric parameters such as: length, width, depth, sinuosity index and slope. The work of this thesis can be divided into three phases: the first phase was data collection, identification and manual mapping of the features; the second phase concerned the measure of the morphometric parameters and the last phase concerned the processing of the collected data. The work conducted was able to answer of the thesis' objectives (§ 1.4).

- 1) *How did the volcanic origin influence the distribution of sinuous rilles? Is there any area where the volcanic activity was significantly intense? Can sinuous rilles help to identify the most active area in the past?*

From the classification of sinuous rille in area groups, it emerged that the spatial distribution of the rilles in the analysed quadrant reflects those that have already been recognized as the most active volcanic areas of the lunar surface, in particular Aristarchus system, Marius Hills and Prinz region. The areas called Gambart, Gruithuisen and Rima Euler showed a relevant concentration of rilles too. However, in these areas most of the rilles present the majority of lengths' rilles < 6 km while a couple of them have lengths in the order of hundreds of kilometres. Unlike the three most active volcanic areas (Aristarchus system, Marius Hills and Prinz region) no intense volcanic activity is recognizable in those area, where usually, instead, it is possible to identify other volcanic features (i.e. domes and cones). The presence of long sinuous rilles (length > 100 km) could be associated with a particular intense volcanic eruption events originating the originated the long rilles of those in the area. Mons Rümker represents an exception because no rilles in the proximity of this volcanic complex (§ 3.1.3) have been found. In fact, layers of basaltic lava flow, detected in the northern area of Oceanus Procellarum, covered the basement of the complex, hiding the bottom area of the structure and the possible presence of sinuous rilles (Spudis, McGovern e Kiefer 2013).

- 2) *Sinuous rilles can be characterized by topographic parameters such as length, width, depth, slope, and sinuosity. Can these parameters indicate a common pattern? Are there any characteristics that repeat? Can sinuous rilles be divided according to common characteristics in a given area?*

The most impressive rilles are concentrated in the proximity of large volcanic complexes, thus marking the fact that volcanic eruption events of noticeable intensity and duration have characterized these areas and gave rise to rilles of considerable size. Long length rilles (length > 100 km) are not widespread on the lunar surface. The slope of the sinuous rilles has shown that these volcanic features are mostly concentrated in the *maria* basalt plains, characterized by slopes < 2 °. Furthermore, no negative slopes were recorded, as instead found by Hurwitz et al. (2013) and Podda et al. (2020). In these studies, a negative slope was justified as a tectonic modification following the formation of the rille. However, this hypothesis seems unlikely due to the absence of visible modifications of the rilles. Most of the rilles have a width varying from 200 m to 700 m and this might indicate a typical shape of the rilles and might suggest a common formation mechanism. No clear relationship between width and depth has been found, and an anomalous shape of two rilles reveal a misinterpretation of the features. No evident correlation between sinuosity index and slope has been observed, even if as the sinuosity increases, the maximum value allowed for the sinuosity seems to decrease.

- 3) *Some SRs are extended for hundreds of kilometres, while others have smaller extensions. What is this difference due to?*

From the analysis of the morphometric parameters it emerged that how sinuous rilles have a large length variance. It is evident, as already mention above, that rilles with an extension of hundreds of kilometres seem to be much less frequent on the lunar surface, than rilles with an average extension of around 15-17 km. Undoubtedly, morphologic characteristics of sinuous rilles depend on the type of mechanism that originated them, as well as the intensity and duration of the related volcanic event. Further studies on the lithology of the surface, as well on the characteristics of the lava flows, would help to understand their origin.

- 4) *Some SRs have a very articulate, meandering pattern but not all of them present the same characteristics. What does it depend on?*

The analysis of the slope and its frequency density shows an average slope of  $1^{\circ}$ - $2^{\circ}$ , confirming the fact that most of the rilles are located in the *maria*. From the work of Hurwitz et al. (2012) and Hurwitz et al. (2013), for shallow slopes the predominant formation process of the initial stage of sinuous rille could be ascribed to thermal erosion, which subsequently is replaced by mechanical erosion. It was also observed that the slope increases, the sinuosity of the rille decreases, but no clear evidence of correlation between sinuosity index and slope has been observed. The physical and/or chemical factors that affect the sinuosity of a channel are not yet identified, but it might be assumed that the lithological composition of the substrate and the lava flows characteristics are conditioning factors that can model the shape of the sinuous rilles and influence their morphometric parameters.

In conclusion, I would like to emphasize that this thesis, far from being a complete study on the analysis of the morphometric characteristics of sinuous rilles, provides a methodologic approach and gives interesting outcomes. It would be advisable to deepen the topic, developing more accurate mapping techniques and increasing the collection of morphometric data that characterize the sinuous rilles.

In this thesis, the available remote sensing data of the Moon have been used only partially and likely not in their full potential. A geological characterization of the rilles would certainly be interesting because some morphometric parameters, such as the sinuosity index and the slope, seem to be particularly related to the lithological characteristics of the substrate. For the sinuosity index it would be worth to investigate the mechanisms of formation and meandering to integrate the study done so far. The methods of identification, mapping and analysis used in this thesis can be applied, with the necessary caution, also in other extra-terrestrial environments of the Solar System, given the presence of sinuous rilles in planets such as Venus and Mars (Komatsu, Gulick e Baker 2001, Leverington 2004), offering the possibility to analyse the differences and the similarities with the rilles observed on other planets, like Venus and Mars (Komatsu, Gulick e Baker 2001, Leverington 2004).

# Bibliography

- Andrew-Hanna, Jeffrey C., et al. "Structure and evolution of the lunar Procellarum region as revealed by GRAIL gravity data." *Nature* 13697, vol. 514, 2014: 68-87.
- Barker, M. K., E. Mazarico, G. A. Neumann, M. T. Zuber, J. Haruyama, and E. D. Smith. "A new lunar digital elevation model from the Lunar Orbiter Laser and SELENE terrain Camera." *Icarus* (273), 2016: 346-355.
- Barnes, Jessica, Renee French, Joshua Garber , Wil Poole, Phillipa Smith, and Yunsheng Tian. "Science Concept 2: The structure and composition of the lunar interior provide fundamental information on the evolution of a differentiated planetary body." *LPI Contribution No. 1694, Huston, TX; Lunar and Planetary Institute*, 2012: 47-131.
- Blair, David M., Loic Chappaz, Rohan Scood, and Colleen Milbury. "The structural stability of lava tubes." *Icarus* (282), 2016: 47-55.
- Boyce, Joseph M. , Thomas Giguere, Peter Mark-Mouginis, Timothy Glotch, and Jeffrey G. Taylor. "Geology of Mairan middle dome: Its implication to silicic volcanism on the Moon." *Planetary and Space Science*, Vol. 162, 2018: 62-72.
- Brunetti, M. T., et al. "Analysis of a new geomorphological inventory of landslides in Valles Marineris, Mars." *Earth and Planetary Science Letters*, vol. 405; <https://doi.org/10.1016/j.epsl.2014.08.025>, 2015: 156-168.
- Cano, Erick J., Zachary D. Sharp, and Charles K. Sherer. "Distinct oxygen isotope compositions of the Earth and Moon." *Nature Geoscience*, 2020.
- Chin, Gordon, et al. "Lunar Reconnaissance Orbiter Overview: The instrument suite and mission." *Springer, Spece Sci Rev*, DOI: 10.1007/s11214-007-9153-y, 2007: 1-29.
- Chin, Gordon, et al. "Lunar Reconnaissance Orbiter Overview: The instrument suite and Mission." *Space Sci Rev* 129; , 2007: 391-419.
- Cuk, Matija, and Sarah T. Stewart. "Making the Moon from a fast-spinning Earth: A giant impact followed by resonant despinning." *Science* Vol. 338, 2012: 1048-1052.
- Cullingham, Melanie B., and Christian Klimczak. "Topographic expressions of lunar graben." *The Geological society of America, Lithosphere* vo.11, no.2 , 2019: 294-305.

Cummings, Warren D. "Pre-Apollo Theories About the Origin." In *Evolving theories on the origin of the Moon*, by Warren D. Cummings, 51-73. Columbia, MD, USA: Springer , 2019.

Daly, R. A. "Origin of the Moon and its topography." *Proceedings of the American Philosophical Society*, 90(2), 1946: 104-119.

Deutsch, Ariel N., Gregory A. Neumann, James W. Head, and Lionel Wilson. "GRAIL-identified gravity anomalies in Oceanus Procellarum: Insight into subsurface impact and magmatic structures on the Moon." *Icarus* 331, 2019: 192-208.

Geiss, J., and A. P. Rossi. "On the chronology of lunar origin and evolution. Implication for Earth, Mars and Solar System as a whole." *Astron Astrophys Rev*, 2013: 21-68.

Guzzetti , F., A. C. Mondini, M. Cardinali, F. Fiorucci, M. Santangelo, and K. T. Chang. "Landslide inventory maps: new tools for an old problem." *Earth Science Review* Vol. 112, 2012: 42-66.

Guzzetti, F., A. C. Mondini, M. Cardinali, F. Fiorucci, M. Santangelo, and K. T. Chang. "Landslide inventory maps: new tools for an old problem." *Earth-Science Reviews* 112 (1-2);doi: 10.1016/j.earscirev.2012.02.001, 2012: 42-66.

Hartmann, W. K., R. J. Phillips, and G. J. Taylor. "'Proceedings of the Conference "Origin of the Moon" held in Kona, HI, October 13-16, 1984. Conference supported by NASA. Houston, TX, Lunar and Planetary Institute, 1986, 797 p. Previously announced in STAR as N85-13709; For individual items see A87-20626.' 1986.

Hartmann, William K., and D. R. Davis. "Satellite-sized planetesimals and lunar origin." *Icarus* 24, 1975: 504-515.

Haruyama, Junichi, et al. "Possible lunar lava tube skylight observed by SELENE cameras." *Geophysical research letters*, vol. 36, L21206, 2009: 1-5.

Horacio, Jesus. "RIVER SINUOSITY INDEX: Geomorphological characterisation ." *Technical note* , 2015: 4.

Hurtwitz, D. M., James W. Head, Lionel Wilson, and Harald Heisinger. "Origin od lunar sinuous rilles: Modeling effects of gravity, surface slope, and lava composition on

erosion rates during the formation od Rima Prinz." *Journal od geophysical research*, Vol. 117, E00H14, 2012: 1-15.

Hurwitz, Debra M., James W. Head, and Harald Heisinger. "Lunar sinuous rilles: Distribution, characteristics, and implications for their origin." *Planetary and Science Spaces* 79-80, 2013: 1-38.

Hurwitz, Debra M., James W. Head, and Lionel Hieesinger, Harald Wilson. "Origin of lunar rilles: Modeling effects of gravity, surface slope, and lava composition on erosion rates during the formation of Rima Prinz." *Journal of geophysical research*, E00H14, vol. 117, 2012: 1-15.

Jaumann, R., et al. "Geology, geochemistry, and geophysics of the Moon: Status of current understanding." *Planetary and Space Science* 74, 2012: 15-41.

Kaku, T., et al. "Detection of Intact Lava Tubes at Marius Hills on the Moon by SELENE (Kaguya) Lunar Radar Sounder." *AGU Publications, geophysical research letters*, 44, 2017: 10,155-10,161.

Kang, Zhizhong, Zhongfei Luo, Teng Hu, and Paolo Gamba. "Automatic extraction and identification of lunar impact craters based on optical data and DEMs acquired by the Chang'E Satellites." *IEEE Journal of selected topics in applied earth observations and remote sensing*, Vol. 8, No. 10, 2015: 4751-4760.

Kerr, Ross C. "Thermal erosion by laminar lava flows." *Journal of geophysical research*, vol. 106, no. B11, 2001: 26,453-26,465.

Komatsu, Goro, and Henrik Hargitai. "Sinuous rilles." DOI: 10.1007/978-1-4614-9213-9\_351-1, *reseach gates*, 2014: 1980-1987.

Kramer, H. J. *Observation of the Earth and its enviroment: Survey of mission and sensor, EoS portal directory*      ESA.      2012.      <https://earth.esa.int/web/eoportal/satellite-missions/c-missions/chang-e-2>.

Lin, Yanhao, Elodie J. Tronche, Edgar S. Streensta, and Wim van Westrenen. "Experimental constraints on the solidification of a nominally dry lunar magma ocean." *Earth and Planetary Science Letters* Vol. 471, 2017: 104-116.

- Liu J., Li J. "Solidification of lunar core from melting experiments on the Fe–Ni–S system." *Earth and Planetary Science Letters* vol. 530, 2020.
- Lu, Yu, Yunzhao Wu, Gregory G. Michael, Alexander T. Basilevsky, and Cui Li. "Young wrinkles ridges in Mare Imbrium: Evidence for very recent compressional tectonism." *Icarus* 329, 2019: 24-33.
- Mahanti, P., M. S. Robinson, and T. J. Thompson. "Characterization of lunar crater wall slumping from Chebyshev approximation of lunar crater shapes." *Proc. "Annual Meeting of Lunar Exploration Analysis Group (LEAG)"*, 20-22 Oct. 2015, Columbia, Maryland, U.S., paper No. 2081, 2015.
- Melis, M. T., et al. "Morphometric analysis of lunar sinuous rilles." *IGRASS*. Yokohama, Japan, 2019. 4904-4907.
- Meyer, M. M., A. Reufer, and R. Wieler. "On the origin and composition of Theia: Constraints from new model of the Giant Impact." *Icarus*, Vol. 242, 2014: 316-328.
- Mimoun, David, Mark A. Wieczorek, and Philippe Zarka. "Farside explorer: Unique science from a mission to the farside of the moon." *Experimental Astronomy* Vol. 33, 2012: 529-585.
- Morbidelli, A., J-M. Petit, B. Gladman, and J. Chambers. "A plausible cause of the late heavy bombardment." *Meteoritics & Planetary Science* 36, 2001: 371-380.
- Mueller, Jerry E. "AN INTRODUCTION TO THE HYDRAULIC AND TOPOGRAPHIC SINUOSITY INDEXES1." *Annals of the association of American Geographer*, vol. 58 (2), doi.org/10.1111/j.1467-8306.1968.tb00650.x, 2010.
- Ouyang , Zi Yuan, et al. "Primary scientific results of Chang'E-1 lunar mission." *Science China, Earth sciences*, November 2010, Vol. 53, No: 11, 2010: 1565-1581.
- Oxford Dictionaries. "regolith - Definition of regolith in English by Oxford Dictionaries". Oxford Dictionaries, 2008.
- P. Gamba, et al. "Automatic extraction and identification of lunar impact craters based on optical data and DEMs acquired by Chang'E satellites." *IEE Journal of selected topic in applied earth observations and remote sensing*; Vol. 8, No. 10, 2015: 4751-4760.

- Pike, R. J. "The geometric signature: quantifying landslide-terrain types from digital elevation models." *Mathematical Geology* 20 (5), 1988: 491-511.
- Podda, S., et al. "New Morphometric Data of Lunar Sinuous Rilles." *IEEE Journal of selected topics in applied earth observations and remote sensing*, vol. 12, 2020: 3304-3316.
- Richardson, Derek C., and Trudi Hoogenboom Hagen. "Crater Chain (Impact, Primary)." *Encyclopedia of Planetary Landforms*, DOI 10.1007/978-1-4614-9213-9\_73-2, Springer Science+Business Media New York 2014, 2014: 1-4.
- Riris, H., et al. "The Lunar Orbiter Laser Altimeter (LOLA) on NASA's Lunar Reconnaissance Orbiter (LRO) mission." *Conference Lasers and Electro-Optics, 2008 and 2008 Conference on Quantum Electronics and Laser Science. CLEO/QELS 2008*, 2008.
- Roberts, Carolyn E., and Tracy K.P. Gregg. "Rima Marius, the Moon: Formation of lunar sinuous rilles by constructional and erosional processes." *Icarus* 317, 2019: 682-688.
- Robinson, M. S., et al. "Lunar Reconnaissance Orbiter Camera (LROC) Instrument overview." *Space Science Reviews* 150, <https://doi.org/10.1007/s11214-010-9634-2>, 2020: 81-124.
- Scaioni, M., et al. "The 'Moon Mapping' project to promote cooperation between students of Italy and China." *The international Archives of the Phorogrammetry, Remote Sensing and Spatial Information Sciences, Volume XLI-B6; XXIII ISPRS Congress, 12-19 July 2016, Prague, Czech Republic*, 2016: 71-78.
- Sharkov, E. V. "The Earth and the Moon developed at the close scenario?" *Horizons in Earth Science Research*, vol. 5, chapter 4, 2011: 177-219.
- Sharkov, E. V., and O. A. Bagatikov. "Early Stages of the Tectonic and Magmatic Development of the Earth and Moon: Similarities and Differences." *Petrology*, Vol. 9, No. 2, 2000: 97-118.
- Speyerer, E. J., et al. "Lunar Reconnaissance orbiter camera global morphological map of the Moon." *42nd Lunar and Planetary Science Conference*, 2011.
- Spudis, Paul D., Patrick J. McGovern, and Walter S. Kiefer. "Large shield volcanoes on the Moon ." *JOURNAL OF GEOPHYSICAL RESEARCH: PLANETS*, VOL. 118, 2013: 1063-1081.

- Sun, Ze Zhou, et al. "The technical deisgn and achievements of Chang'E-3 probe." *SCIENTIA SINICA Technologica, Volume 44 , Issue 4*, 2014: 331-343.
- Urey, H. C. "The planets: Their origin and development." *Yale University Press*, 1952.
- Wilhems, D. E. *The geology history of the Moon*. U.S. Geological survey, 1987.
- Ye, Pei Jan, Ze Zhou Sun, and Fei Li. "An overview of the mission and technical characteristics of Change'4 Lunar Probe." *Science China Technological Sciences volume 60*, 2017: 658-667.
- Yordanov, V., M. Scaioni, M. T. Brunetti, M. T. Melis, A. Zinzi, and P. Giommi. "Mapping landslides in lunar impact craters using Chebyshev polynomials and DEM's." *Arch. Photogramm. Remote Sens. Spatial Inf. Sci., Vol. XLI-VI Prague, Czech Republic*, 2016: 8 pages.
- Zhang, Feng, et al. "Newly Discovered Ring-Moat Dome Structures." *Agu-publication. Geophysical research letters*, 2017: 9216-9224.
- Zinzi, A., M. T. Capria, E. Palomba, P. Giommi, and L. A. Antonelli. "MATISSE: A novel tool to access, visualize and analyse data from planetary exploration missions. Zinzi et al., *Astronomy and Computing*, 2016, <http://dx.doi.org/10.1016/j.ascom.2016.02.006>." *Springer International Publishing Switzerland*, 2016: 16-28.
- Zuo, Wei, Chunlai Li , and Zhoubin Zhang. "Scientific data and their release of Chang'E-1 and Chang'E-2." *The science and Application Center for Moon and Deepspace Exploration, National Astronomical Observatories, Chinese Academy of Sciences, Beijing 100012, China*, 2013: 024-044.